MEASUREMENT AND ANALYSIS OF RESIDUAL STRESSES IN ZIRCONIA DENTAL COMPOSITES USING MICRO X-RAY DIFFRACTION

By

HRISHIKESH BALE

Master of Science in Mechanical Engineering

Oklahoma State University

Stillwater, Oklahoma

2005

Submitted to the Faculty of the
Graduate College of the
Oklahoma State University
in partial fulfillment of
the requirements for
the Degree of

DOCTOR OF PHILOSOPHY
May, 2010

MEASUREMENT AND ANALYSIS OF RESIDUAL

STRESSES IN ZIRCONIA DENTAL COMPOSITES USING

LAUE MICRO-DIFFRACTION

Dissertation Approved:

Dr. Jay C. Hanan
Dissertation Adviser

Dr. Raman P. Singh

Dr. Kaan Kalkan

Dr. David Rubenstein

Dr. James Smay

Dr. A. Gordon Emslie
Dean of the Graduate College

ACKNOWLEDGEMENTS

"Gurur Brahma Gurur Vishnu, Gurur Devo Maheshwarah
Gurur Saakshaat Para-Brahma, Tasmai Shri Guruve Namah"

Is a phrase from the ancient 8th century Hindu scriptures, that describes the importance of finding a Guru – A teacher who has wisdom and authority in a specialized area and can impart supreme knowledge. A teacher who conjures unquestionable obedience – making his disciple have full trust in his teacher. This is what Dr. Jay Hanan means to me and I would like to take this opportunity to show my heartfelt gratitude to my advisor. His continuous encouragement, guidance and support have enabled me to develop a thorough knowledge in the field of X-ray diffraction and tomography. His constructive suggestions, clear directions and resolute confidence in me, from the initial to the final stage have helped me to successfully complete my Ph.D.. No amount of adjectives I use can overstate the importance of Dr. Jay Hanan's contribution in molding my Ph.D. and my personality on a whole. With this said, I would like to express my sincere thanks to him.

My Master's and my Ph.D. would not have been possible without my parents. I am eternally grateful to my Dad and Mom for always giving me the immense opportunities. They have raised me with love, taught me and supported me in all my decisions. I thank them for their patience, dedication and everlasting motivation to uplift my spirits. I dedicate this thesis to them.

My wife Ridhima is the source of my strength. No words can express the amount of encouragement and support my wife has provided throughout. I will always be thankful for her patience and the constant cheering up at times when I was low which drove me back to positive starts. Without fail, I would like to thank her for the zillion cups of tea and coffee she has made during the long nights.

I would also like to seize this opportunity to name and extend my thanks to the many people who made this journey special and this thesis possible. My special thanks to the committee members – Dr. James Smay, Dr. Raman Singh, Dr. Kaan Kalkan and Dr. David Rubenstein. I am very grateful to Dr. Smay, Dr. Singh and Dr. Hongbing Lu for letting me use their labs.

I would like to mention a special thanks to my collaborators - Dr. Nobumichi Tamura (ALS) and Paulo Coelho (NYU School of Dentistry). A significant amount of work from my Master's and Ph.D. work would not have been possible if not for Dr. Tamura's state-of-the-art XMAS software. He has patiently and enthusiastically guided me throughout the years in achieving the success Dr. Paulo Coelho has been a constant support in providing the dental samples and providing insights from the dental research area. The frequent telephonic conferences with him have always proven to add newer dimensions to my work.

I have had the privilege to use the facilities at the Advanced Photon Source, IL and the Advanced Light Source, CA to put my research work into effect. I thank Dr. Francesco and Yong Chu, Beamline Scientist at 2BM at Argonne for their constant support with the experimental work at APS. I would like to sincerely thank Martin Kunz, Beamline Scientist at ALS for providing me with constant support during my long hours at ALS. I also thank Dr.

Yuncheng Zhong for sharing insights on the IGOR software and help on the experimental setup at APS.

John Gage from the DML lab here at OSU needs a special mention for providing the access and resources required in fabrication of the high precision load frame.

I thank my colleagues (Dr.) Nitin Daphalapurkar, Boshen Fu and Nick Phelps for their support at multiple occasions. Special thanks to Dr. Gajendra Pandey for his constant inspiration and enthusiastic help on endless questions. Thanks to (Dr.) Abhishek Singh for his timely advice and essential discussions on core concepts.

Big thanks to Amol Birje and Amol Ganpatye who have always believed in me and bestowed undying support during the most difficult times. Undoubtedly Balaji, Giri, Mukund, Swarup, Dhivakar, and Saravan have a huge contribution towards this success. They have been with me in my most enduring time and raised my spirits throughout. I thank my fellow lab mates Advait Bhat, Sudheer Bandla, Praful Bari, Ashwin, Ranjan and Masoud Allahkarami for all their help and wonderful company. I would also like to express my thanks to my extended family for making my PhD worthwhile.

I am thankful for the constant funding and support from "OCAST" which has enabled me to carry my research on dental ceramics this far. The work at the Advanced Photon Source and Advanced Light Source was supported by the US Department of Energy, Office of Basic Energy Sciences under Contract no. W-31-109-ENG-38 and Contract No. DE-AC02-05CH11231 respectively.

CONTENTS

1. LIST OF FIGURES

LIST OF TABLES

CHAPTER I

1 INTRODUCTION

Typical core restorative materials in modern dentistry include alumina, zirconia, or noble metal alloys that are veneered with porcelain. There has been a transition from the use of metal alloy cores to all ceramic crowns with no metallic components. Porcelain veneered alumina and zirconia cores have unique esthetic properties and closely resemble natural teeth due to the refraction of light from the internal cores. Among ceramics, zirconia has high fracture toughness and crack resistant characteristics.

Figure 1 Fractured porcelain veneer layer off the top of a 4 unit Zirconia FPD [1]

The phase transformation from tetragonal to monoclinic produces local volume expansion favoring crack closure, resulting in additional strength. [2-3] However there are reports of failures of ceramic dental crowns during service. [4-6]

Failures mostly involve the chipping of the veneer layer with the crack propagating parallel to the interface within the veneer layer. Roughly 5-10 % of the failures undergo complete catastrophic failure wherein the crack propagates all the way through the core.[7] This type of failure is mostly observed in crowns with alumina cores. Maximum service loads experienced by the restoration in a patient's mouth do not exceed 150 N [8] which are typically distributed over a wear area of 1 – 4 mm^2, [9] leading to stresses in the range of 30 – 150 MPa, which are much below the ultimate failure stress value of most commonly utilized ceramic core materials (as seen in Figure 1). In spite of such low loads, significant numbers of failures occur in the first year of restoration. Such failures can be caused by prolonged cyclic loading with stresses amplified or reduced by residual stresses present in the restoration. Cyclic fatigue promotes crack propagation, which usually initiates at areas with stress concentration. Observations of the failures in crowns with zirconia cores indicate the existence of detrimental tensile residual stresses may be present in the porcelain region, close to the interface. During crown fabrication in dental laboratories, residual stresses develop due to factors including grain anisotropy, both shape and compliance anisotropy of the crystal [10-11], coefficient of thermal expansion mismatch, and the overall complex tooth geometry. The magnitude of the residual stresses in dental restorations is unknown. [1, 12] Along with stress induced phase changes, grain-to-grain stresses are significant. Small grain sizes along with the high linear X-ray absorption coefficient of zirconia are some of the major challenges faced when considering X-ray micro-diffraction for residual stress measurement. Furthermore the complex geometries involved makes the residual stress measurement challenging.

A method to measure these residual stresses non-destructively would provide valuable feedback for the fabrication of new crowns. The knowledge of the magnitude and distribution of the stresses will aid in identifying designs with minimized tensile residual stress concentrations in the porcelain and correlation of their performance to the magnitude of the stress. The presence of compressive residual stresses is often beneficial since they inhibit crack growth. Tensile residual stresses favor crack initiation and growth. [8] In order to determine the residual stress distribution in dental restorations, a polychromatic X-ray (Laue) micro-diffraction technique was adopted. Laue micro-diffraction can provide deviatoric residual stresses in a crystalline material. [13] Since X-rays can penetrate the veneer, the residual stresses in the underlying zirconia core layer can be determined using X-ray diffraction from the zirconia layer. Typically, dental crowns have a complex curved geometry. To simplify the geometrical constraint, a disk shaped zirconia model composite was fabricated with thermal history and material properties typically utilized for dental restorations. The deviatoric strains developed within the zirconia layer were determined by X-ray Laue micro-diffraction at Beamline 12.3.2 of the Advanced Light Source.

A method of developing a finite element model of real components involving complex geometries has been developed through the use of X-ray micro-tomography. The technique enables a comparison of experimental results with simulations for the sample under observation. In the current study, the technique has been employed in understanding the residual stress behavior in a dental crown and in a model dental composite sample generated using the robo-casting technique. [14-16]

CHAPTER II

2 LITERATURE REVIEW

2.1 Dental materials

2.1.1 Ancient materials

The use of external materials for dental restoration dates back to as early as 500 BC, which involved the use materials such as gilded wood, gold and ivory to stop cavities [17-18]. It has been found that most ancient civilizations comprising of the Chinese, Hindu, Egyptians, Japanese and the early European civilizations had practiced dental medicine, involving the use of gold, silver, ivory and wood for the purpose of dental restorations [19].

2.1.2 Amalgams

In the late 19^{th} century, G. V. Black presented his investigations on the use of Ag and Sn in amalgam alloys which could be used as restorative materials [20]. To increase the strength further, and decrease the flow, some amount of copper was added. These amalgam alloys contained less than 5% copper, known as low copper amalgam alloy, and were in use for

over a period of 60 years with no significant variation. These amalgams were extensively used in restoration of posterior teeth and often encountered corrosion and chipping at the edges. A small percentage of mercury is present in this alloy along with a phase of Hg-Sn. It was observed by many studies [21-22] that this particular phase underwent corrosive breakdown, especially severe at crevices and other cavities and eventually led to failure of the restoration. In 1962, William Youdelis achieved a major breakthrough in the area of amalgams when he experimented with Ag-Cu eutectic added to the traditional amalgam. Initially this was not accepted by the dental associations due to high copper percentages. However, even without Youdelis's knowledge, his addition of the eutectic alloy had induced additional compressive strength to the dental amalgam. The composition lead to a higher strength alloy due to change in the phase. The dispersion hardened alloy eliminated the Ag-Sn phase. The higher copper percentage thus induced enhanced corrosion resistance and reduced the occurrence of damage. [23]

2.1.3 Ceramics as dental materials

The introduction of ceramics as a dental restoration material took place in 1903, when Land [24] experimented with feldspathic porcelain crowns. Further in 1965 there were developments in improving the mechanical and physical properties of porcelain by addition of alumina. [25] The first paper on using zirconia as a biomaterial was written in the 1969 by Helmer and Driskell [26]. Most of the material developments related to structure and property improvement and applications related to dental restorations took place in the early 1990's. [27] Dental ceramics are categorized on the basis of its application either as a base material or veneering material. Categories of ceramics in use as dental materials are listed.

2.1.4 Glass ceramics

Glass ceramics consist of lithium-disilicates (SiO_2-Li_2O), leucites (SiO_2-Al_2O_3-K_2O) and feldspathics (SiO_2- Al_2O_3-Na_2O-K_2O). The most widely utilized lithium-disilicates and leucite glass ceramics are IPS empress, IPS empress-2 and IPS e.max press manufactured by Ivoclar Vivadent, Schaan, Liechtenstein. [4-6, 28-30] IPS Empress and Empress 2 are lithium disilicate glass ceramics, the former being a leucite reinforced ceramic. These ceramics are fabricated by heat-pressing the ingot into investment molds. The molded product is further veneered with fluorapatite-based porcelain veneers. Numerous variations of IPS empress are available that are designed to have variations of shades and translucency. They also vary slightly in their strengths, and hence are selectively used based on the posterior or anterior position of restoration. [31] The leucite based glass ceramics with modifications in particle size [32] and firing modes are suitable for use with advanced CAD/CAM systems to achieve the desired geometries through advanced machining techniques.

Vita Mark I/II (VITA Zahnfabrik, Bad Sackingen, Germany) is a more commonly used feldspathic porcelain consisting of alumina (20-23%) and silica (60-64%). This glass is monochromatic, meaning only a particular shade is possible, hence is a challenging material for esthetical considerations. This problem has been solved by the development of machinable ceramic blocks [33] with several layers of different shades [34], which optically replicates the natural tooth. The structural block consists of an opaque internal shade with an intermediate semi-opaque region covered by an outer translucent layer. This forms a raw ingot for a CAD/CAM system which can machine the inlay to clinical specifications.

2.1.5 Alumina-based ceramics

Alumina based ceramics are utilized in single tooth restoration and also in 3 part fixed partial dentures (FPD's). Alumina based ceramics, mainly used as the high strength framework or core material, gives the final finished crown its strength. These ceramics have a percentage of alumina ranging from anywhere between 50% to 99.9%. [9, 35] The high percentage, high purity alumina ceramics have very high flexural strengths and are used where there was a high functional demand (posterior crowns and FPD's). [35] The first all-ceramic system available for dental restorations was In-Ceram Alumina (VITA Zahn-fabrik), introduced in 1989. The alumina ceramics are fabricated starting with a sintering procedure on a dental replica die in a high temperature oven, followed by slip-casting to infuse lanthanum glass into the porous skeletal network. [36] This step significantly reduces porosity and flaws which can lead to crack initiation and propagation. This was further veneered with feldspathic porcelain. To counter the problem of opacity posed by pure alumina ceramics, magnesia ($MgAl_2O_4$) was added to the alumina green before sintering. These ceramics commonly known as alumina spinel have adequate translucency and a comparatively lower flexural strength, hence are more suitable for the anterior restorations. [37] Among the all-ceramic alumina–based restorations, Procera (Nobel Biocare AB, Goteborg, Sweden) has the highest strength. [38] The high strength was a result of the 99.9% high purity aluminum oxide that is used in the coping along with the low-fusing porcelain veneer. Fabrication of Procera based restoration starts with the mechanical compaction of the high-purity alumina on an oversized die followed by sintering at 1550^{o}C. The post-sintering product has reduced porosity and the desired final dimensions from shrinkage during sintering. The restoration is complete upon the application of the feldspathic veneering porcelain having matching thermal expansion coefficients. [38]

2.1.6 Zirconia-based ceramics

Yttiria stabilized polycrystalline zirconia (YZP) is one of the preferred ceramic materials, due to its relatively higher fracture toughness and flexural strength among ceramics. Zirconium oxide is a transformation toughening material, which is polymorphic in nature and occurs in three different crystallographic forms. It is cubic at its melting point at 2680^{o}C. As the temperature is reduced to 2370^{o}C and below, the cubic structure transforms to tetragonal.[2]

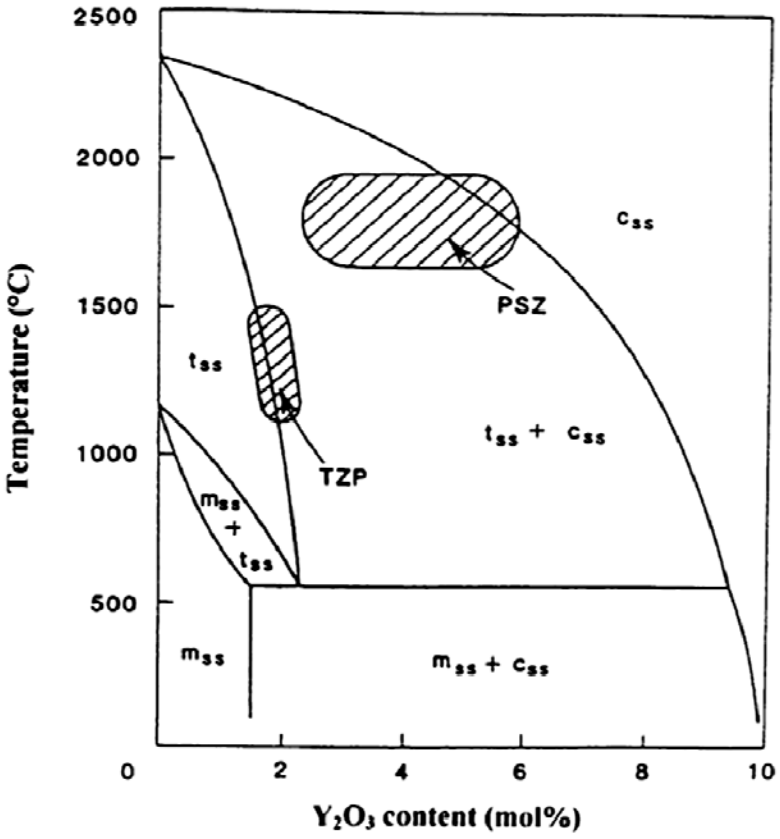

Figure 2 The various phase relations at different processing temperatures and yttria compositions for zirconia. Shaded regions indicate the processing ranges [2]

Further, a tetragonal-to-monoclinic transformation occurs below 1170^{o}C.[39-40] This transformation involves 3-5% volume expansion, which is accompanied with high internal

stresses. The volume expansion is restricted by the addition of 3% yttrium-oxide, which stabilizes the tetragonal phase of zirconia.

Any crack propagating through bulk stabilized zirconia creates a concentrated stress zone at its tip, which results in the transformation of zirconia from tetragonal-to-monoclinic at the crack front. The resulting volume change due to transformation creates a net compressive stress at the crack tip which counter-acts the tensile stresses, thus arresting the crack. The mechanism of the phase transformation ahead of the crack, leading to the toughening mechanism [3] is illustrated in Figure 3.

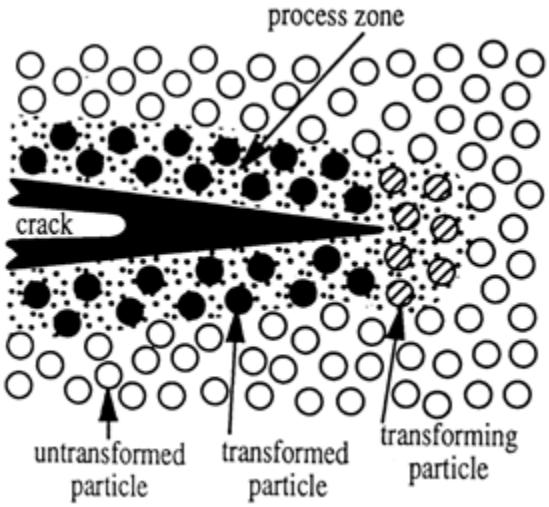

Figure 3 Illustration of the mechanism of transformation toughening in zirconia. The tensile stresses encountered by the crack tip causes a phase transformation from tetragonal to monoclinic. The propagating crack tip dissipates most of the energy in transforming the tetragonal phase. [3]

The yttria- partially stabilized zirconia (Y-TZP) possesses high flexural strength, high fracture toughness and is dimensionally and chemically stable, [41-42] which makes it potentially suitable for dental restorations. Y-TZP is primarily used as a core material due to its excellent mechanical properties. The cores are fabricated using computer aided design

and manufacturing systems (CAD/CAM). [43] Mechanically compacted green homogenous blocks of zirconia are milled according to specifications of the framework, with 20-25% shrinkage tolerance. This is to account for the shrinkage during the sintering process. A final framework or coping with desired dimensional specifications is obtained after sintering. It is also possible to obtain the final product by directly milling fully sintered blocks of Y-TZP. However the mechanical strength is compromised due to flaws introduced in the milling process. Tool wear is also considerable as compared to machining of the compacted green or partially sintered blocks. [44] The finished framework is veneered with feldspathic porcelain to obtain the final restoration.

CHAPTER III

3 MICRO-LAUE DIFFRACTION

The beamline 12.3.2 at the Advanced Light Source, Berkeley CA, produces brilliant micro-focused polychromatic X-ray beams with a spectral range of 6-22 keV and a sub-micron sized cross section, which are suitable for high resolution Laue micro-diffraction. Conventional X-ray diffraction involves beam sizes on the order of a millimeter. Hence only the grain averaged bulk properties can be studied.

Table 1 comparison of x-ray facilities available for conducting residual stress measurement

Facility	Beamline /Model	Source	X-ray Wavelength	Beam size
Advanced Light Source, Berkeley, CA	12.3.2	Synchrotron Ring	Polychromatic 6-22 keV	500 nm x 500 nm
Argonne National Laboratory, Chicago, IL	APS ID-2-BM	Synchrotron Ring	Monochromatic 17.85 keV	0.7 μm x 0.8 μm
Bruker AXS D8 Laboratory Diffractometer	D8	Copper X-ray tube	Monochromatic	0.3 mm spot

With the development of the third generation synchrotron sources and advances in the positioning and computational capabilities, it is possible to achieve the sub-micron probe sizes, thus facilitating the measurement of properties at the grain level. Figure 4 shows a schematic of the layout of beamline 12.3.2 at the ALS. The beamline's source is an X-ray beam, obtained from a bend magnet. The large cross section beam is then focused onto XY-slits using platinum coated torroidal mirrors.

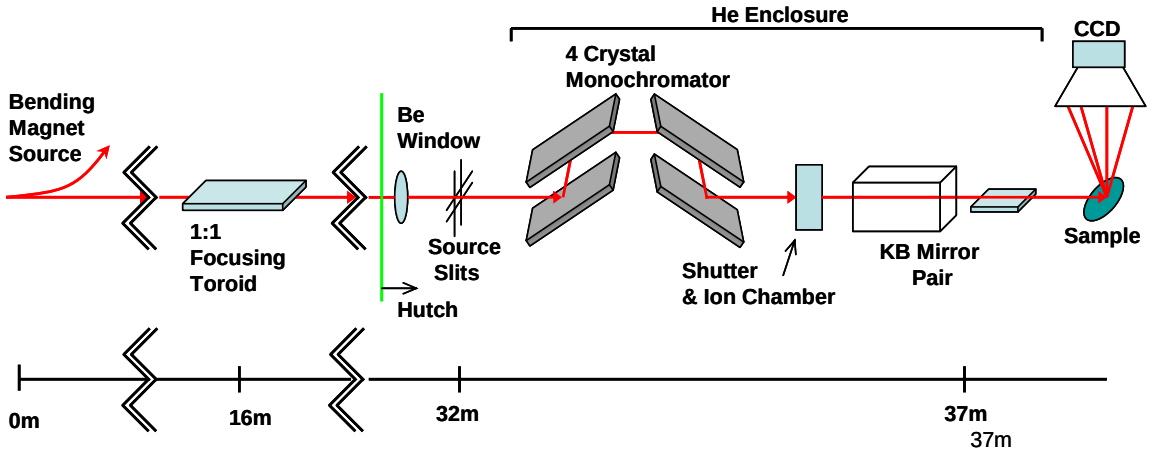

Figure 4 Schematic layout of Beamline 12.3.2 at the Advanced Light Source [45]

The next stage consists of a 4 crystal monochromator, which is designed to allow either a monochromatic or a polychromatic beam. The beam then travels to the shutter which controls the entry of the beam into the hutch. The most critical focusing stage is the Kirkpatick-Baez (KB) mirrors which focus the millimeter sized beam to a sub-micron beam. The KB mirrors consist of elliptically bent platinum coated silicon substrates. The focal point and the size of the beam are controlled by varying the bend in the mirrors using piezo actuators. The focusing optics are capable of achieving a cross section of 0.5 µm x 0.5 µm.

The current experiment was planned to determine the inter-granular residual stress within zirconia. Laue diffraction was utilized to observe the stress distribution in individual grains. Emerging diffracted X-rays from the sample, produce spots on the CCD oriented in 90° reflection geometry as shown in Figure 6.

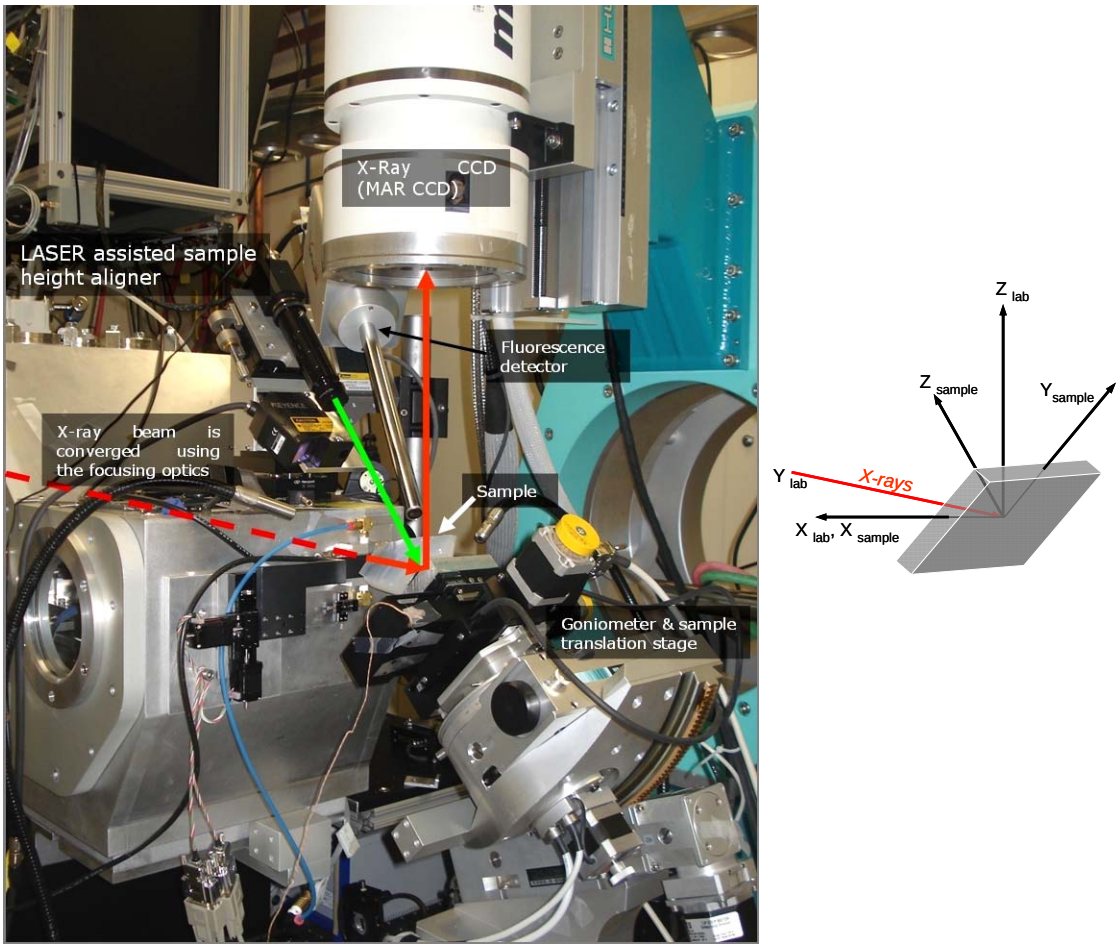

Figure 5 Experimental setup at Beamline 12.3.2, Advanced Light Source. Red dashed arrow indicates the X-ray beam incident on the sample and diffracted onto the CCD. The setup is in a 90° reflection geometry. A Laser alignment setup is used to position the sample at the focal point of the beam. A specific sample area can be registered using the fluorescence detector.

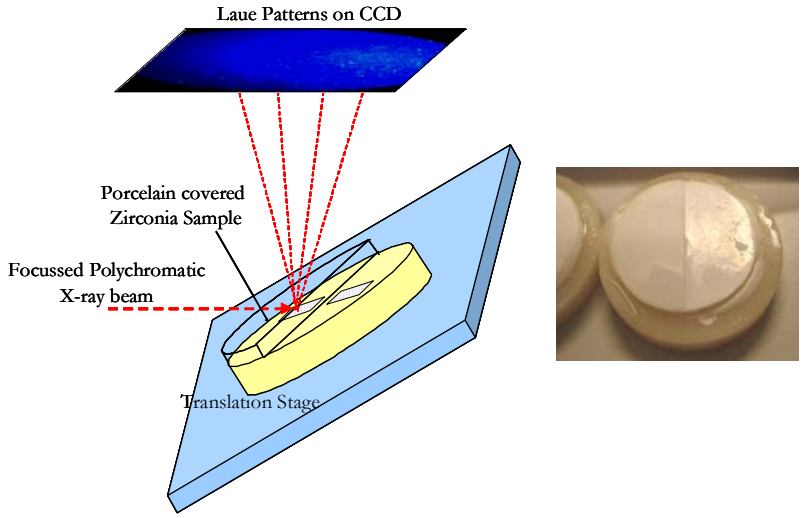

Figure 6 Schematic of the sample orientation in 90° reflection geometry. The sample consists of two semicircular zones where raster scans were obtained to study the residual stresses.

Spots registered for every position of the beam on the sample are collected onto an X-ray CCD and analyzed using XMAS [46] (X-ray micro-diffraction analysis software), a customized indexing software. The procedure and the sample geometry is explained in the following sections.

3.1 Sample Preparation

The main goal of the experiment is measurement of the in-situ residual stresses in a dental restoration such as a crown. However, the complex geometry of crowns is challenging, especially in the case of a diffraction setup where a successful experiment depends on several factors such as the X-ray transmission through the veneer, the sample volume being considered and the sample orientation. Sample orientation decides the components of stress that can be observed. To simplify the geometry of the sample while maintaining the clinical relevance, a model composite sample was also designed.

3.1.1 Crown Geometry

Figure 7 is a 3D rendered sectional view of a zirconia core dental crown showing the zirconia core which forms the base layer. The core is veneered with porcelain to a specific contour which closely resembles the natural tooth geometry.

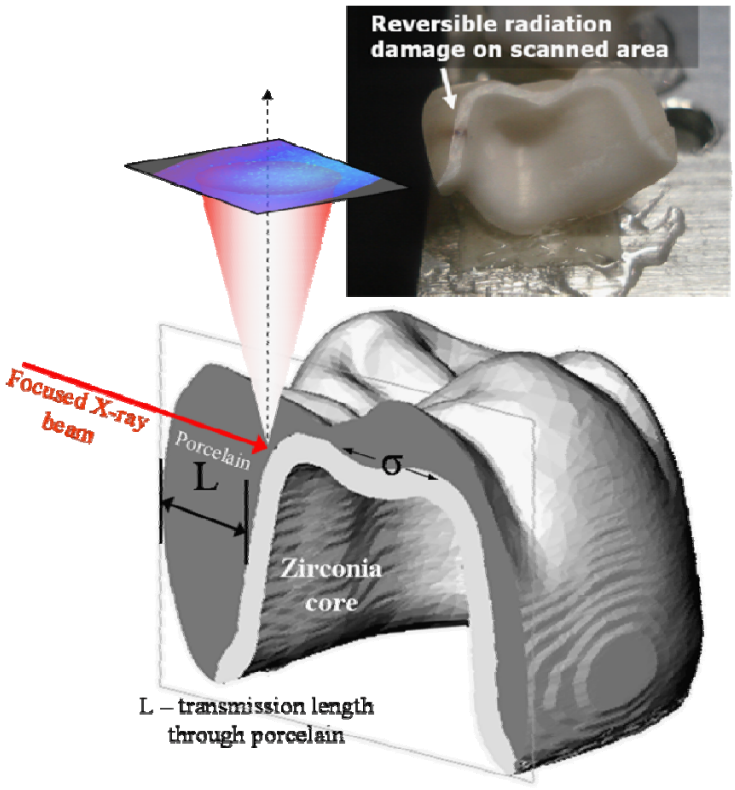

Figure 7 Cross Sectional view of a porcelain veneered dental crown. The base layer is made of zirconia and has a porcelain veneer on top.

Orientation of the crown sample with respect to the X-ray beam is critical and a possible orientation that enables measurement of residual stresses is shown in Figure 8. Since the porcelain veneer is 90% amorphous, the feasible zone which reveals the stress state through diffraction is the underlying zirconia core which is crystalline comprised of the tetragonal phase. The position of the surface of zirconia has to coincide with the focal point of the beam. The beam further away from the focal point diverges leading to a bigger spot than desired. Furthermore, the sample alignment with the beam focal point Figure 7 shows a pre-

selected area suitable for a scan based on the thickness of porcelain on top of the zirconia core.

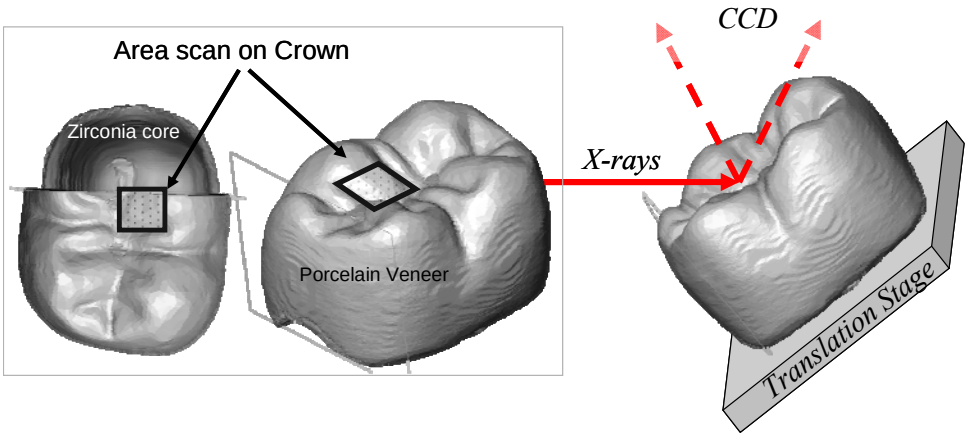

Figure 8 (Left) Sectional and isometric view of the crown showing the area where a possible micro-diffraction scan can be performed. (Right) Orientation of the crown in a diffraction setup (Illustrated CCD-sample distance is not to scale)

When considering an X-ray diffraction measurement for a geometry such as the one seen in Figure 7, it is important to determine the maximum X-ray transmission. For longer travel paths of the X-ray beam through the sample, there is higher absorption, resulting in lesser reflections on the CCD. A model ceramic with small transmission lengths is desirable.

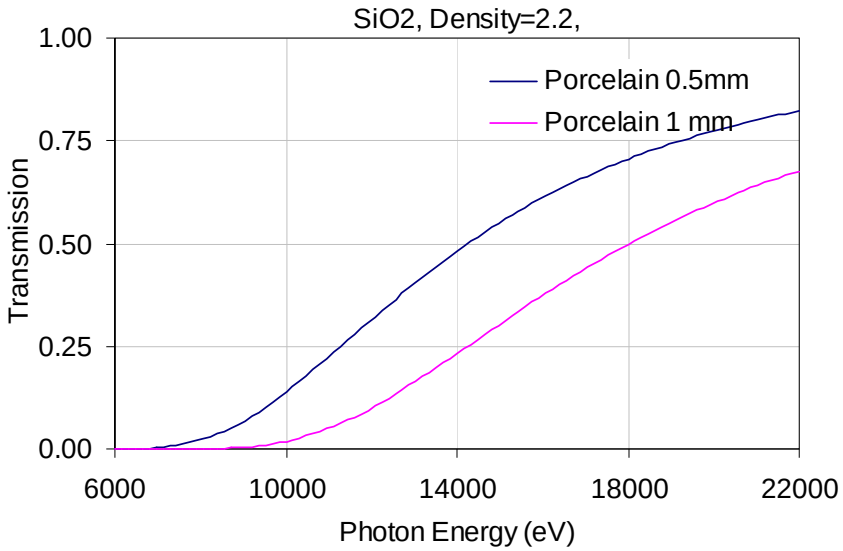

Figure 9 X-ray transmission for the white beam for two different thicknesses of porcelain.[47]

3.1.2 Model Ceramic composite

The samples consisted of a disk 1 mm thick made of sintered polycrystalline yttria stabilized zirconia. The disk was half coated with a porcelain layer 0.5 mm thick which was ground and polished. The porcelain layer and the zirconia disk were fabricated with typical dental laboratory thermal treatment procedures for fabrication of all ceramic zirconia-porcelain systems. The disks were maintained under water for at least 2 weeks before X-ray measurements. No further processing was required for Laue-XRD measurements. A finite element simulation of the model composite was also performed to compare the magnitude of the expected interface residual stresses in the crown and the model ceramic disk.

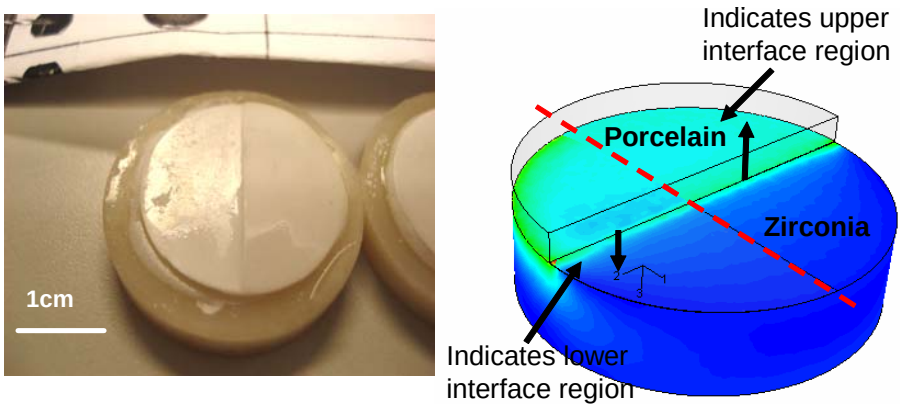

Figure 10 Geometry of the model ceramic disk sample. The schematic shows a finite element simulation of the interface residual stresses in the model composite

3.1.2.1 Microstructure

For SEM analysis, the zirconia disks were polished using fine diamond slurry (0.1 micron diamond size). After the initial polishing process the samples were thermally etched at a temperature of 1100^{o}C for 20 minutes. Thermal etching reveals the grain boundaries, which are not well defined otherwise. SEM images showed that the grains were of submicron size (0.1 - 0.3 μm).

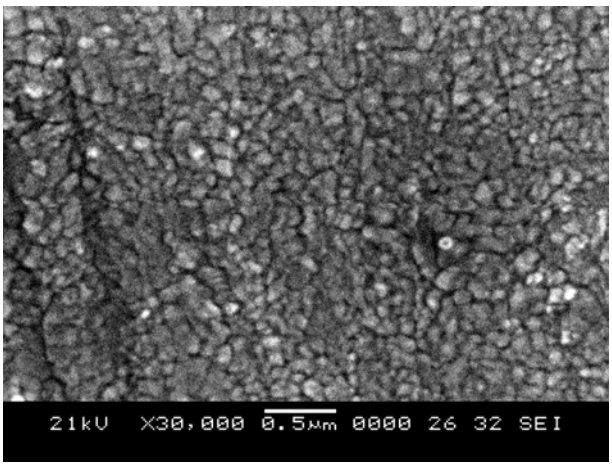

Figure 11 SEM image of the neat Zirconia disk surface at 30,000× magnification. The grain sizes are in the submicron range (0.1 – 0.3 μm).

3.2 In-situ fatigue, Sample Positioning and Alignment

An important case of the study is the observation of stress fields and deformation mechanisms in zirconia under the influence of cyclic fatigue. Crowns are subject to prolonged cyclic fatigue in a patient and numerous occurrences of sudden catastrophic failures have been reported.[6] A customized load frame designed for *in-situ* fatigue was utilized to subject the sample to cyclic fatigue. Cyclic loading has to be carried out under an aqueous environment, to simulate chewing and in order to account for the crack opening phenomenon that occurs when a liquid is trapped in an already initiated crack. The kinematic bases shown in Figure 12 are fitted on both the translation stage and the load frame, thus facilitating efficient sample switching with the location of the area of interest registered repeatedly. The experimental setup is designed such that the beam along with the optics is fixed. To map a diffraction scan, the sample is moved in steps to complete a 2D grid using the high precision translation stage as shown in Figure 13.

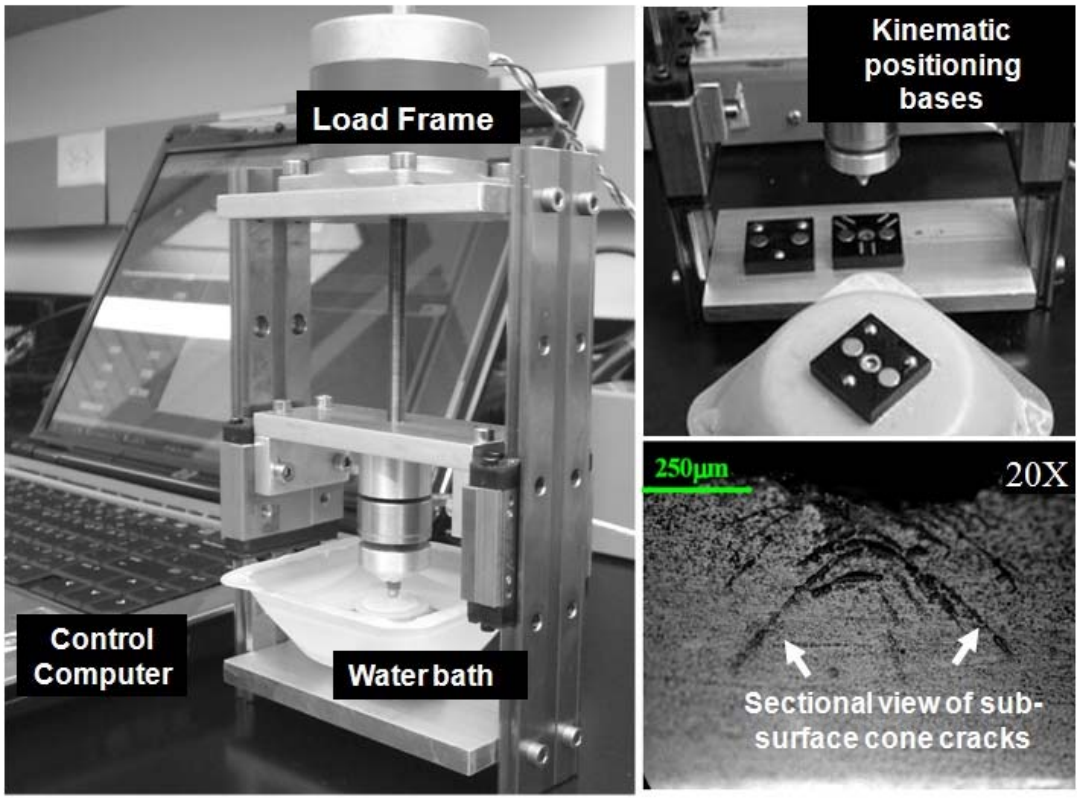

Figure 12 (Left) In-situ cyclic fatigue load frame. Top Right - Kinematic bases for easy re-positioning of sample on load frame and stage. Bottom Right - Cone cracks emerging underneath the indenter after cyclic loading

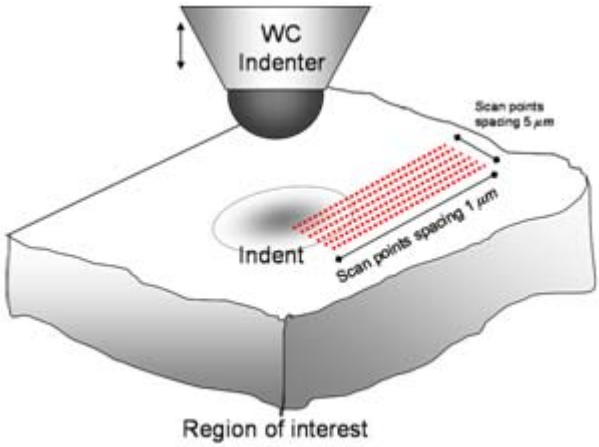

Figure 13 Schematic of scan points under the cyclic fatigue indenter. Image not to scale

3.3 Positioning

An important starting parameter in the experimental setup is the distance in between the sample and the CCD camera. The simulation module of the X-ray Micro-diffraction Analysis Software (XMAS), along with the lattice parameters of the zirconia, provides a simulation of the reflections. Since the sample to camera distance plays an important role in obtaining accurate results, accurate positioning of the sample surface at a desired distance from the camera is important. The positioning is carried out using a laser beam aligned to intersect the center of diffraction. The sample registration is adjusted by following the fluorescence of zirconia under X-rays using a micro-fluorescence detector. The porcelain fluoresces, producing a visible blue light. This observation was advantageous in monitoring the region being scanned in diffraction. Another important aspect of the sample positioning was the registration in the XY plane of the sample. Due to weight and geometry limitations of the translation stage, fatigue cycling of the sample was carried on the load frame outside the X-ray hutch. To maintain consistency in fatigue cycling and mapping the exact same area after every step, a specialized kinematic base attachment was provided to the load frame, which can re-position the sample on the load frame and the translation stage within an angular tolerance of a micro-radian and an in plane repositioning accuracy of one micrometer.

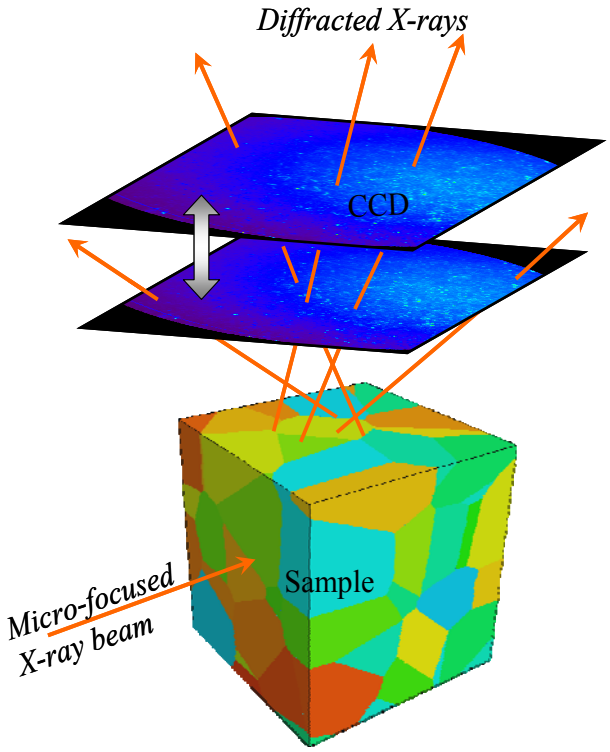

Figure 14 Schematic of dependence of the camera-to-sample distance on the number of reflections captured on the CCD.

The simulated result provides important information related to the number of reflections at a specific camera distance. It is desirable to obtain a large number of reflections, typically more than 12, since it refines the fit increasing the strain accuracy. Decreasing the camera distance by 55 mm, results in triple the number of reflections captured on the camera, as seen in Figure 14. However, this results in a reduced resolution per spot, since there are less pixels/diffraction spot. An optimum distance is chosen based on a set of diffraction patterns acquired at different camera distances.

3.4 Diffraction Theory

The simulation of the direction of the reflections incident on the CCD is based on the geometry of the crystal lattice, the structure factor and Bragg's Law as shown below.

Bragg's Law is given by

$$\lambda = 2d\sin\theta \quad \text{(Eqn. 1)}$$

where λ is the incident wavelength in Angstroms, d is the lattice plane spacing, and θ is called the Bragg angle or the diffraction angle. The value of d is based on the set of planes that are diffracting the beam, which depends on the crystal structure. One polychromatic beam diffracts many reflections.

For a tetragonal crystal structure the inter-planar spacing is given by,

$$(Tetragonal) \qquad d_{hkl} = \frac{a}{\sqrt{h^2 + k^2 + l^2(a^2/c^2)}} \quad \text{(Eqn. 2)}$$

where a, c are the lattice parameters for the tetragonal crystal and h,k,l are the miller indices.

The directions of the diffraction spots is given by

$$\sin^2\theta = \frac{\lambda^2}{4}\left(\frac{h^2+k^2}{a^2} + \frac{l^2}{c^2}\right) \quad \text{(Eqn. 3)}$$

Equation 3 calculates the directions of the diffracted intensities. The arrangement of atoms, commonly called the structure factor, also affects the scattering of the beam from a unit cell. The structure factor for a particular material is given by

$$F_{hkl} = \sum_{1}^{N} f_n e^{2\pi i(hu_n + kv_n + lw_n)} \quad \text{(Eqn. 4)}$$

where, the summation extends over all *N* atoms of the unit cell, and the u, v and w are the fractional coordinates. Another factor which is used in the simulation of the reflections is the multiplicity factor which accounts for the relative proportion of the planes that contribute to a particular reflection. In other words, the multiplicity factor considers the number of different crystal planes that have the same inter-planar spacing.

3.5 Sample-CCD distance

3.5.1 Laue pattern simulation

The simulated Laue pattern for a tetragonal and monoclinic crystal lattice of zirconia is shown in Figure 15 & Figure 16 respectively. The tetragonal phase of zirconia shows brighter but lesser number of peaks as compared to the patterns for monoclinic phase at a particular camera distance. This difference in the peaks observed is due to the difference in symmetries of the two phases, the tetragonal phase being highly symmetric compared to the monoclinic phase. The observation of increased number of reflections at a smaller camera distance is in accordance with Figure 14.

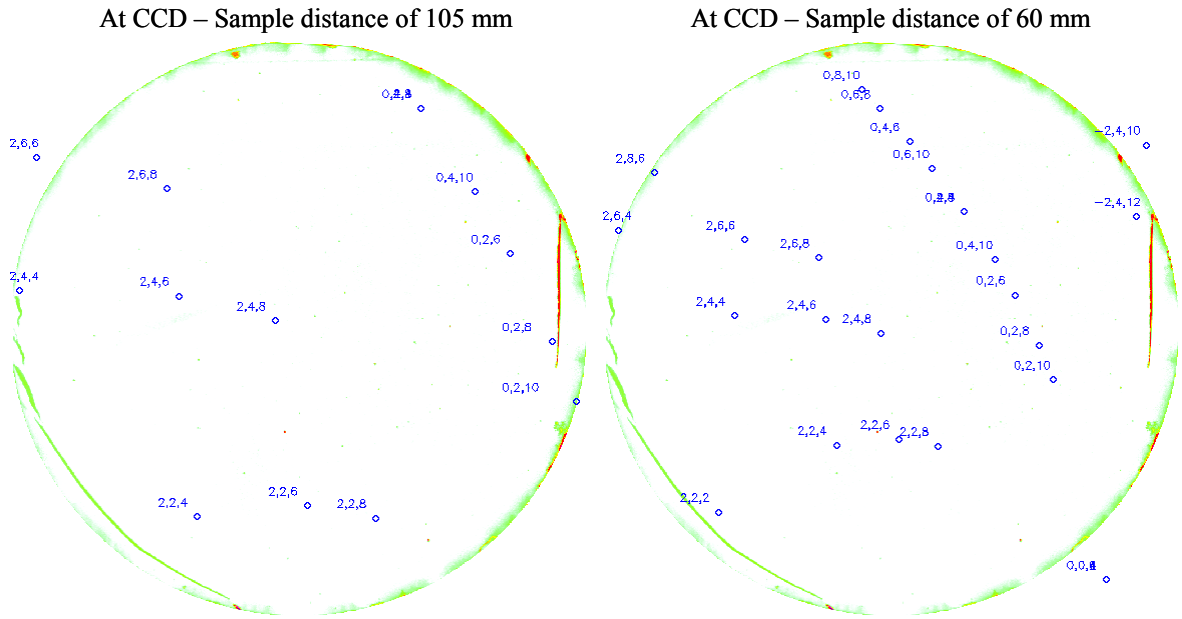

Figure 15 Simulated Laue pattern of tetragonal Zirconia at 2 different distances of the camera. (10 reflections at D_1(105mm) and 22 at D_2(60mm)).

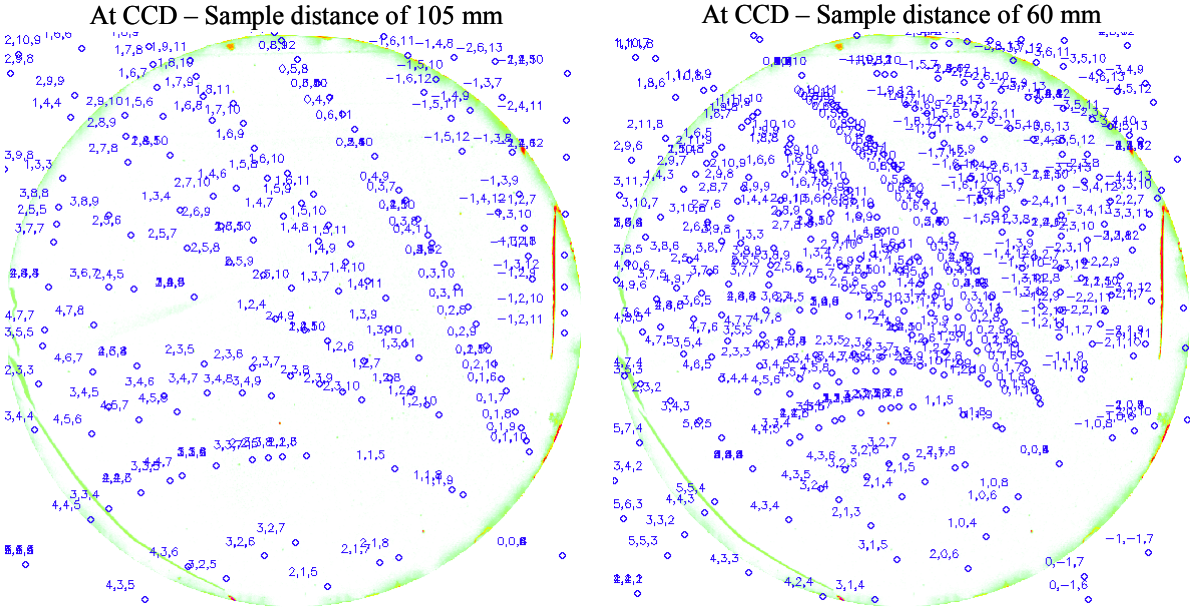

Figure 16 Simulated Laue pattern of monoclinic Zirconia at 2 different distances of the CCD. (112 reflections at D_1(105mm) and 220 at D_2(60mm)).

3.6 Data Analysis

3.6.1 Procedure

Laue patterns collected for every spot on the sample were analyzed using the XMAS software. The sample surface was scanned with a 500 nm cross section beam over a rectangular grid of size 0.5 mm by 0.024 mm. Figure 17 lists the step-wise process of indexing an acquired Laue pattern. The Laue pattern at every data point of the raster scan was input to the XMAS software. The raw image was in TIFF format and consisted of the CCD artifacts which were eliminated by a reference image subtraction followed by the background subtraction. The reference image was an image file from the data set where no diffraction spots were observed. The background subtraction step also involved normalizing the intensities of the peaks. Input parameters to XMAS included the reference crystal lattice parameters, the energy range, and sample to detector distance, detector tilt, and sample orientation parameters.

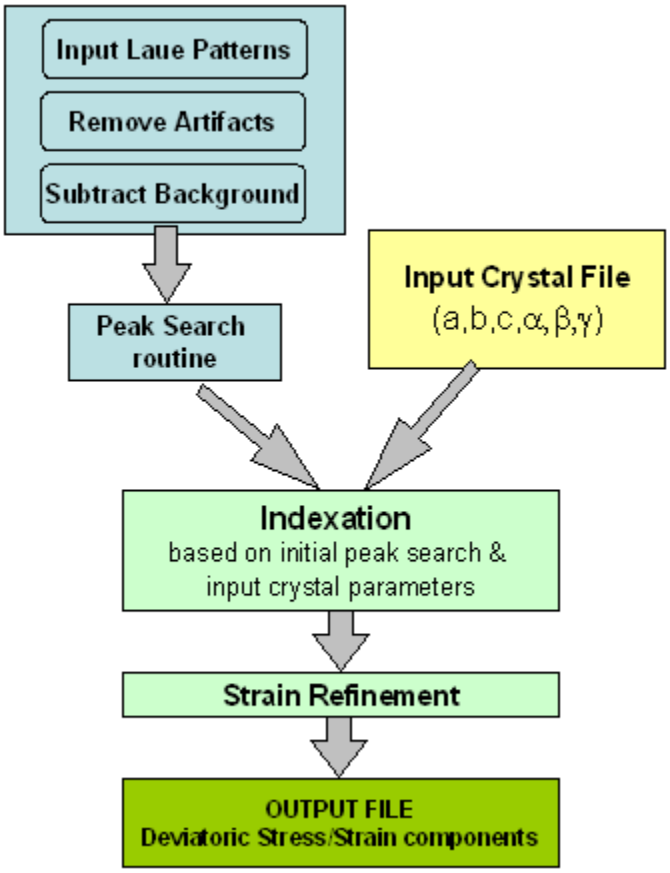

Figure 17 Flow Chart of the data analysis procedure

3.6.2 Image Processing

Raw images obtained from the diffraction scan tend to contain artifacts such as scratches or defects on the CCD camera. These appear as higher intensity spots, which can be accounted as peaks by the search routine. Also there exists background intensity due to air, amorphous media, and diffraction from grains lying deep beneath the surface. Background removal is a critical step in the image processing, wherein the background intensities superimposed on the diffraction spots are eliminated, thereby enhancing the profile of a diffraction spot. Figure 18 illustrates the background and its line profile observed in case of the zirconia sample.

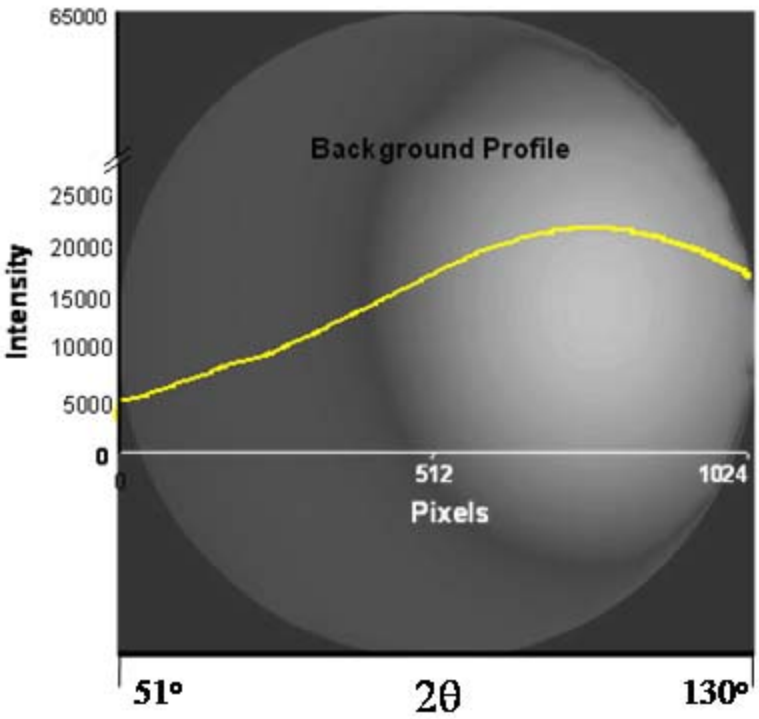

Figure 18 Illustration of the background on the CCD along with a line profile along the diameter of the CCD.

Figure 19 illustrates the process of artifact removal and background subtraction. Red numbers indicate the indexed grains in zirconia after an initial peak search based on the Lorentzian peak profile.

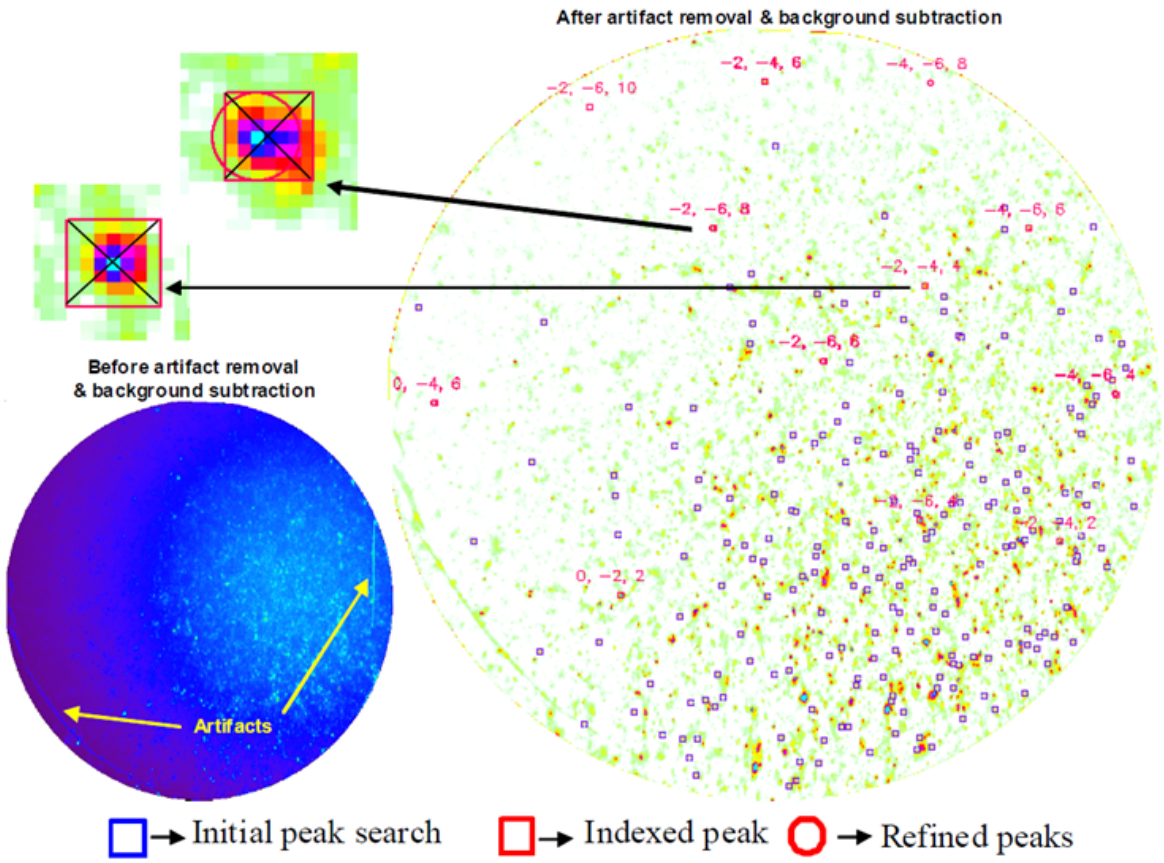

Figure 19 Indexed pattern of the tetragonal phase of zirconia. 10 peaks were utilized in determining the strain. The close up view of the indexed peak shows the peak search and fit. The symbol "□" indicates the brightest peaks found during the initial automated peak search. Based on the input reference crystal parameters, further peak search and fitting is carried out autonomously. Found peaks are marked by the symbol "□".

3.7 Parameters

3.7.1 Crystal file

XMAS determines a set of reflections belonging to a particular grain based on the input crystal file consisting of the lattice parameters a, b, c and the lattice angles α, β, and γThe stiffness constants for a particular crystal has to be defined as well. Most crystals are anisotropic in stiffness in different directions. Table 2 shows values for the different phases

of zirconia considered. The method initially determines crystal strains from the reflections obtained from the diffraction experiment and utilizes the compliance tensor to determine the components of stress according to the generalized Hooke's law, $\sigma_{ij} = C_{ijkl}\,\varepsilon_{kl}$.

Table 2 Comparison of Elastic Constants for Cubic, Tetragonal and Monoclinic phases of Zirconia (Table has been adapted from [10]. Values of directional components of the stiffness constant from different studies have been compared for the three different phases of ZrO_2.)

		***c* phase**		***t* phase**		***m* phase**	
		Study 1	Study 2	Study 1	Study 2	Study 1	Study 2
S_{11}	(x 10^{-12} Pa^{-1})	2.76	3.4	3.46	4.12	3.45	3.41
S_{22}						3.35	5.03
S_{33}				4.06	4.45	5.37	6.78
S_{44}		16.7	16.8	17.0	17.9	11.4	10.4
S_{55}						15.3	14.7
S_{66}				15.4	5.68	8.73	8.28
S_{12}		-0.56	-1.0	-0.96	0.34	-1.28	-1.60
S_{13}				-0.59	-1.15	-0.116	0.608
S_{15}						1.73	1.65
S_{23}						-1.78	-3.71
S_{25}						-2.68	-3.19
S_{35}						2.42	3.10
S_{46}						3.42	1.88
C_{11}	(GPa)	401	390	327	263	358	361
C_{22}						426	408
C_{33}				264	262	240	258
C_{44}		56	60	59	55.9	99.1	99.9
C_{55}						78.7	81.2
C_{66}				64	44	130	126
C_{12}		96	162	100	15	144	142
C_{13}				62	72	67	55
C_{15}						-25.9	-21.3
C_{23}						127	196
C_{25}						38.3	31.2
C_{35}						-23.3	-18.2
C_{46}						38.8	-22.7

3.7.2 Calibration Parameters

The calibration parameters are important values that need to be input to XMAS. Without the correct parameters, the analysis fails. Details of most parameters can be found in the XMAS

manual [48]. There are certain experiment specific parameters which control the output of the analysis and are discussed below.

3.7.3 Distance

The distance parameter specifies the distance from the center of the CCD camera to the point of diffraction from the sample. Accurate measurement of this value is critical since strain calculations are based on the angles imposed by the reflections onto the CCD which are functions of the distance. In the current experiment a distance of 106.52 mm was utilized. The initial value for distance can be picked based on Laue pattern simulations as explained in the previous section. For unknown distance parameters, such as in case of the diffraction volume being sub-surface, the distance calibration method of triangulation [13] is utilized. Other parameters that are related to the camera to sample distance are the values related to the yaw and tilt of the camera, which should be close to zero in a well aligned setup. These parameters contribute to the angular calculations in finding strain.

3.7.4 Angular Tolerance

The tolerance value is specified in degrees and allows the program to search for peaks within a certain error range. A larger tolerance value leads the program to search for more pixels in a given peak's vicinity leading to slower computation. In zirconia, which has a fine grain size (0.1μm – 0.3μm), there are a large number of reflections on the CCD. Hence, a larger angular tolerance increases the chance of including more than 2 peaks in the area of search. Such a region of multiple overlapping peaks from different grains can lead to error in strains.

3.7.5 Peak Search Box Size

The peak search box size sets the size of the search box for every peak. The pixel values lying in the box are fit using the Lorentzian fit criterion. Box size plays a critical role in the

analysis. Since peak search is the initial step in indexing the grains, it is important to consider every spot corresponding to a grain. A larger box size potentially encloses neighboring peaks. Such neighboring peaks are then erroneously treated to be a single peak by the software. Figure 20 shows a region of interest with 2 neighboring peaks. The two distinct peaks can be fit when the box size is changed from 6 to 3. The number of pixels utilized in the centroid calculation is the square of twice the box size. Hence the box size value also contributes to the computational time.

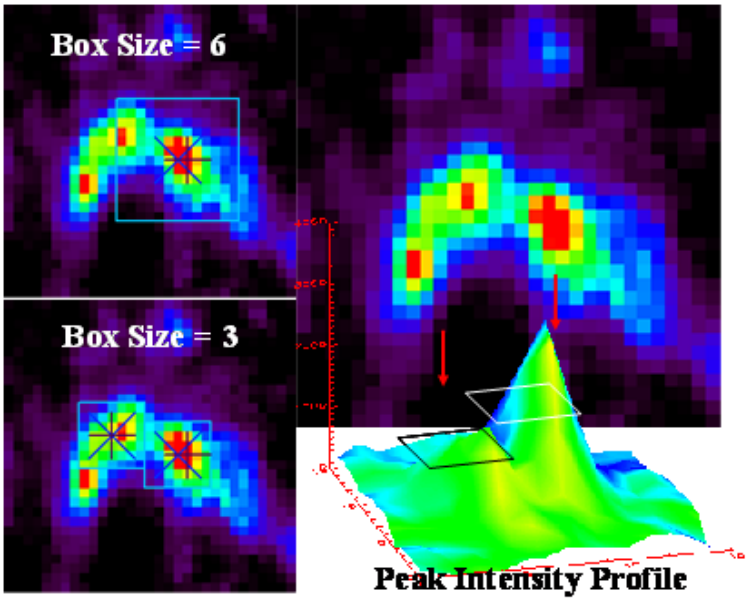

Figure 20 Effect of search box size on the number of peaks searched. A reduction in box size allowed searching two overlapping peaks. Lorentzian intensity profile of the region considered exhibits 2 peaks with slight overlap.

3.7.6 Threshold

The threshold value, mainly dependant on the sample, creates a subset of N peaks from the entire set of peaks searched. This list is passed on to the indexation algorithm for further calculations. A convenient way of applying threshold is by the use of the threshold factor which is a multiplicative factor to the average intensity of the CCD image. A threshold

factor of 6 for the neat zirconia data, led to an output of 250 ± 20 peaks searched. A higher threshold factor was used for the data related to the zirconia sample covered with porcelain. This was due to the fact that only the bright peaks from the tetragonal phase of zirconia show up over the amorphous silica background. The weaker reflections seen in neat zirconia were attenuated.

3.7.7 Maximum Pixel Deviation

The maximum pixel deviation parameter is expressed in pixels and indicates the maximum deviation between the centroid location of a peak search box and the pixel position resulting from the peak fit. A typical value for materials with large grains is 5, but due to a small grain size and large number of resulting reflections, a value of 0.75 was used. With lesser reflections per grain indexed, the strain accuracy decreases. The conservative tolerance value of 0.75 for the pixel deviation suppresses large strains which can arise from erroneously indexed peaks.

3.7.8 Indexation

The indexation step consists of assigning miller indices to the peaks searched in the search routine. The peaks seen on the CCD emerge from the grains aligned with a favorable orientation. The angular range of peaks varies from a two-theta angle of 10° to 167° for the polychromatic X-ray beam of 6-22 keV. Incident X-ray beams interact with the sample and were elastically scattered. Using this consideration we have, $q_{\exp} = k_{out} - k_{in}$ which gives the direction of the scattering vectors.

The list of N bright peaks generated by the search routine is used and a new list of the angles between the experimental scattering vectors is generated. A comparison is made between the generated list and between the theoretical scattering vectors computed from the input crystal

lattice. Within the bounds of the input angular tolerance, the indexation code searches triplets of angular matches between the experimental and theoretical angle list. Further, a calculation of a list of possible reflections incident on the CCD is done. The best match amongst the list is the triplet that matches the largest number of experimental reflections.

The crystal lattice parameters for the tetragonal zirconia phase were determined using powder diffraction of zirconia powder (using a Bruker D8 Diffractometer). Based on initial parameters and a reference crystal file, XMAS analyzes the positions of diffraction spots and indexes them to individual grains. Following indexation, based on the deviation of the reflections from the expected position and the reference *d*-spacing, the strains are refined for each indexed grain in every image. The strain obtained from polychromatic diffraction (Laue diffraction) consists of the deviatoric components only (red box in Eqn.).

$$\varepsilon_{ij} = \varepsilon = \boxed{\begin{pmatrix} \varepsilon_{11} - \Delta/3 & \varepsilon_{12} & \varepsilon_{13} \\ \varepsilon_{12} & \varepsilon_{22} - \Delta/3 & \varepsilon_{23} \\ \varepsilon_{13} & \varepsilon_{23} & \varepsilon_{33} - \Delta/3 \end{pmatrix}} + \begin{pmatrix} \Delta/3 & 0 & 0 \\ 0 & \Delta/3 & 0 \\ 0 & 0 & \Delta/3 \end{pmatrix}$$

$$\text{With } \Delta = \varepsilon_{11} + \varepsilon_{22} + \varepsilon_{33}$$

Where, Δ is the hydrostatic strain.

A separate measurement using a monochromatic X-ray beam or a micro-Raman measurement is required to determine the hydrostatic component. The output file of a particular analysis is stored as a sequential list file consisting of the strain components, respective stress components, the resolved shear stress/strain values for every data point on the sample. Upon analyzing the sequential list, it was found that 95% of the data points from the area scan were indexed as different grains. In the remaining 5% of scan points, 2-3 repetitive grains were observed. Indexation of a majority of the scan points as different

grains was due to the small grain size and also since the scan points were spaced 1 μm apart, which reduced the chances of scanning the same grain.

For any given data point, a minimum of 6 spots were chosen as a limit for indexation. The strain index parameter increases with the strain accuracy. Where, strain accuracy is indicated by observing physically relevant strains. Figure 19 illustrates an indexed pattern of the tetragonal zirconia phase. Based on the initial peaks and the found peaks, the entire pattern is indexed.

3.7.9 Sequential List File

An automatic analysis module allows the batch analysis of an entire set of images collected from a scan on the sample. The results for each image is stored into an indexation file which further consists of information pertinent to each grain indexed at that particular spot. At the end of the automatic analysis, the software tabulates the results from the entire indexation file database into a sequential list file. Data sorting, distribution analysis was conducted on subsets of the sequential list file.

Macroscopic and microscopic stress distribution

The sequentially stored list of information related to individual images which in turn belong to a specific spatial location on the sample can be analyzed for microscopic or macroscopic stress information. Sub-grain (Type III) & grain-to-grain (Type II) stress information can be obtained when the grain size is larger than the beam. A microscopic grain-to-grain stress analysis has been conducted on an aluminum-sapphire metal matrix composite previously using a similar setup on beamline 7.3.3 as shown in Figure 21. [13, 49] Identification of a set of scan points belonging to a particular grain, was done using orientation angle matching.

A particular scan point was assigned a specific grain number based on the the orientation angle within a certain range, and based on an initial histogram sort.

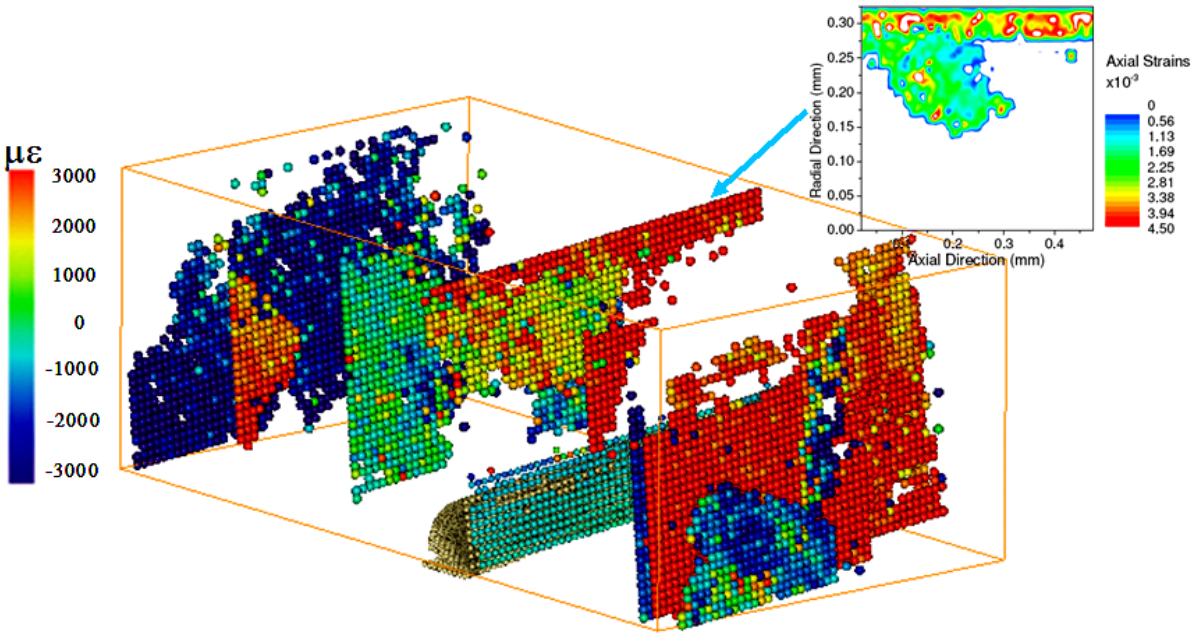

Figure 21 Micro-beam strain analysis on aluminum sapphire composite demonstrates the capability of the technique in measuring in-situ strains within individual grains. Each data point on the graphic indicates a diffraction scan point on the sample. The 3D plot indicates various grain morphologies along the X-ray beam and a portion of the sapphire fiber which is a part of the fiber-matrix composite.

It is desirable to have such a result related to the grain-to-grain behavior, however in the current scenario; the grain sizes lie in the range of 0.1-0.5 micrometer, which are in the size range of the focused beam cross section. The orientations obtained over a certain area do not form a definitive histogram for the small grain size under observation. Hence mapping individual grains was not possible. The technique however gives us a good understanding of the microscopic strain over 3-10 grains averaged and macroscopic strain state when averaged over an entire scan area of many grains. It is important to have a well defined sample and laboratory coordinate system to interpret the results of the strain tensor from the experiment.

Since we look at the entire result from a laboratory coordinate perspective or a global perspective, the beam which is always in a fixed position is kept as a reference. The sequential list also provides us with individual crystallographic orientation, strain and stress information. This is especially useful when analyzing bigger grain sizes as in Figure 21. The reference coordinate system is illustrated in Figure 22.

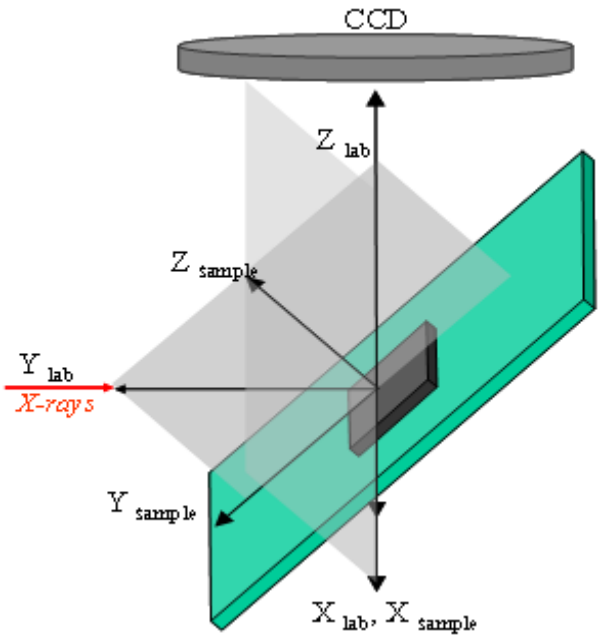

Figure 22 Laboratory and sample co-ordinate system at beamline 12.3.2.

3.8 Results

Analysis and extraction of interpretable results from the sequential list file was done using a data analysis and statistical software (Origin Pro 7.1). An initial sort based on the grain index was done to eliminate any ambiguous grains indexed. Ambiguous grains generally have less than 5 peaks indexed or have indexations which have erroneous peaks which tend to have very low peak intensities. A multiple conditional sort is implemented on a dataset related to every direction of the strain component which includes strains in the principal directions and the shear planes. A range of ± 8000 με was utilized for the sort. Datasets

acquired for monolithic zirconia, porcelain veneered zirconia and subsequent datasets related to the former two subjected to sets of fatigue cycles were refined in a similar manner as explained above.

The refined dataset for every individual sample case is analyzed for an area averaged macroscopic stress/strain. This is achieved by utilizing a histogram of the probability distribution of strains from individual scan points.

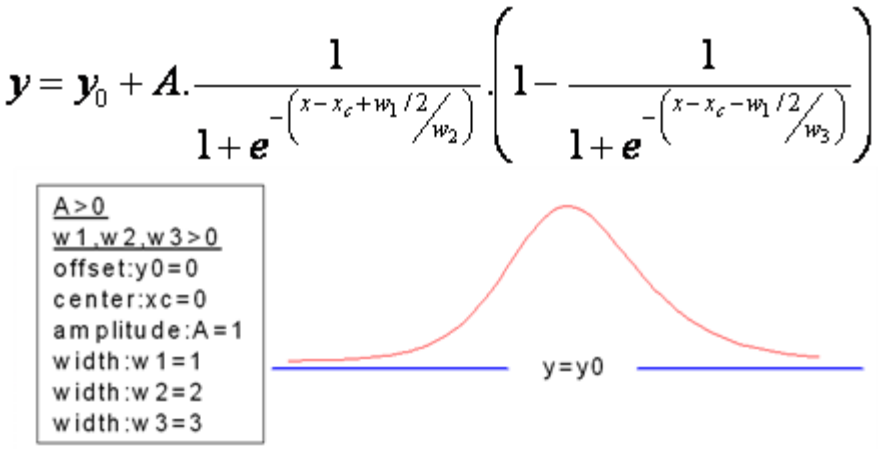

Figure 23 Asymmetric Sigma fit used to fit the stress and strain distributions

The range of ± 8000 με was binned into 100 με bins. It was found that all the data had a probability density distribution which was asymmetrically skewed around zero strain. The distributions were fit using an asymmetric sigma function as expressed in Figure 23. All the density distributions were normalized by a factor of the number of occurrences, which enables for a comparison of the residual stress/strain states of different samples.

3.8.1 Comparison of residual stress in monolithic zirconia and porcelain veneered zirconia model composite

Figure 24 & Figure 25, show the distribution of strains and stresses respectively and their respective fits using the asymmetric sigma 2 fit function. The results of stress and strain for

the two cases namely, monolithic and porcelain veneered zirconia are summarized in Table 3.

Table 3 Summary of residual stress and strain values averaged over many grains. Comparison indicates an introduction of stress when monolithic zirconia is veneered and sintered. The change indicates a relative stress/strain as a result of mismatch in coefficient of thermal expansion.

Stress (MPa)	XX	XY	XZ	YY	YZ	ZZ
Monolith	-79 ± 6	112 ± 5	-64 ± 5	-64 ± 5	38 ± 8	-65 ± 7
Veneered	267 ± 14	183 ± 7	2.3 ± 24	-96 ± 43	-365 ± 30	-143 ± 7
Δ stress	346	71	66	-32	-403	-78

Strain ($\varepsilon \times 10^{-6}$)	XX	XY	XZ	YY	YZ	ZZ
Monolith	-38 ± 60	584 ± 30	-405 ± 112	-157 ± 30	-133 ± 794	-82 ± 51
Veneered	1293 ± 90	1010 ± 150	359 ± 500	-873 ± 200	-2287 ± 330	-685 ± 64
Δ strain	1331	426	764	-716	-2154	-603

The error bars on the strain in the shear directions XZ and YZ are high and are due to the large standard deviation of the distribution in these directions. XZ and YZ planes are shear planes and lie in the plane of the incoming beam and the normal vector. All the values of stress/strains tabulated in the tables above include the deviatoric component only. A separate monochromatic energy scan is required to furnish the information related to the hydrostatic component.

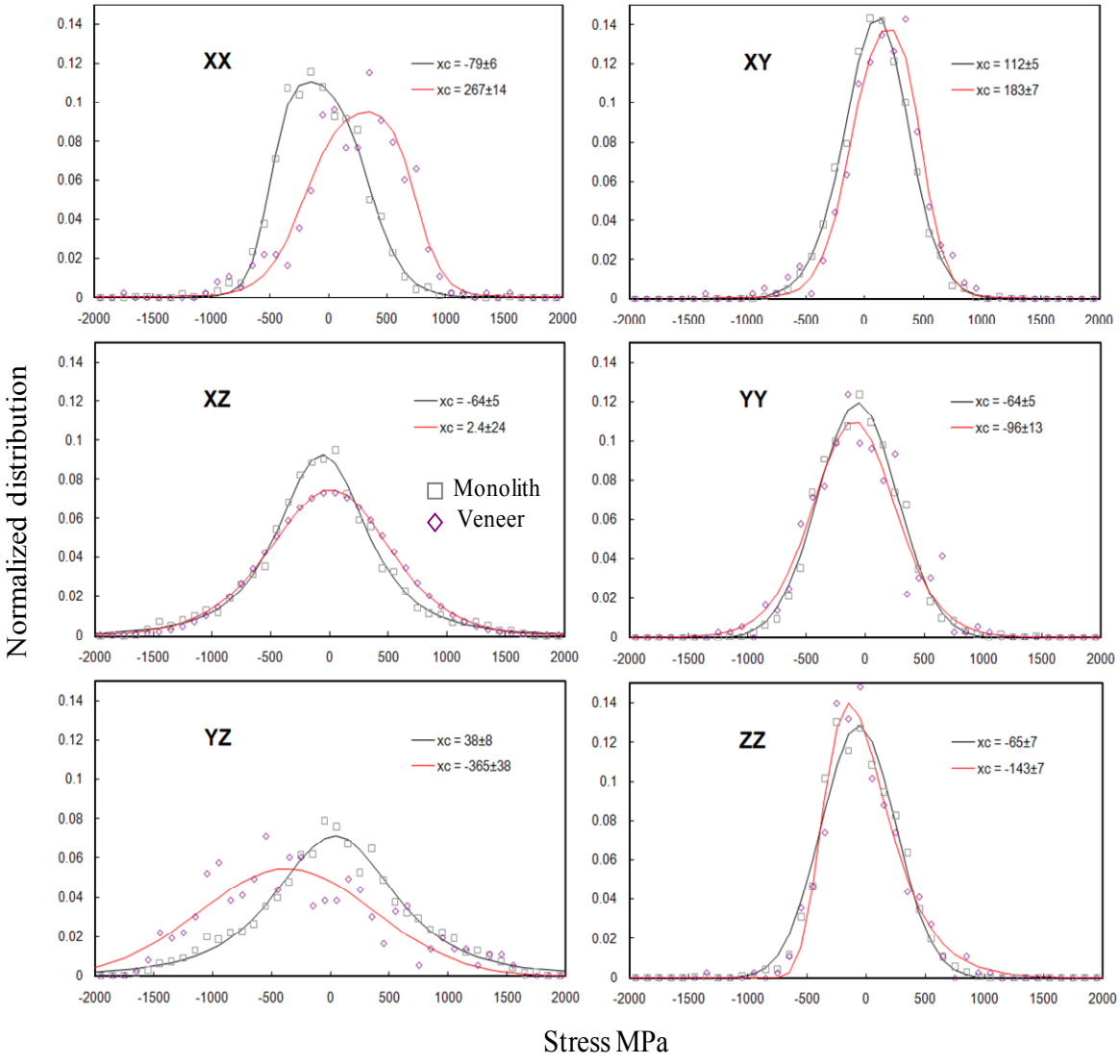

Figure 24 Type II Residual Stresses in Zirconia and Interface Residual Stress in Porcelain veneered Zirconia. xc indicates the center of the distribution obtained through the sigma2 fit function for different datasets.

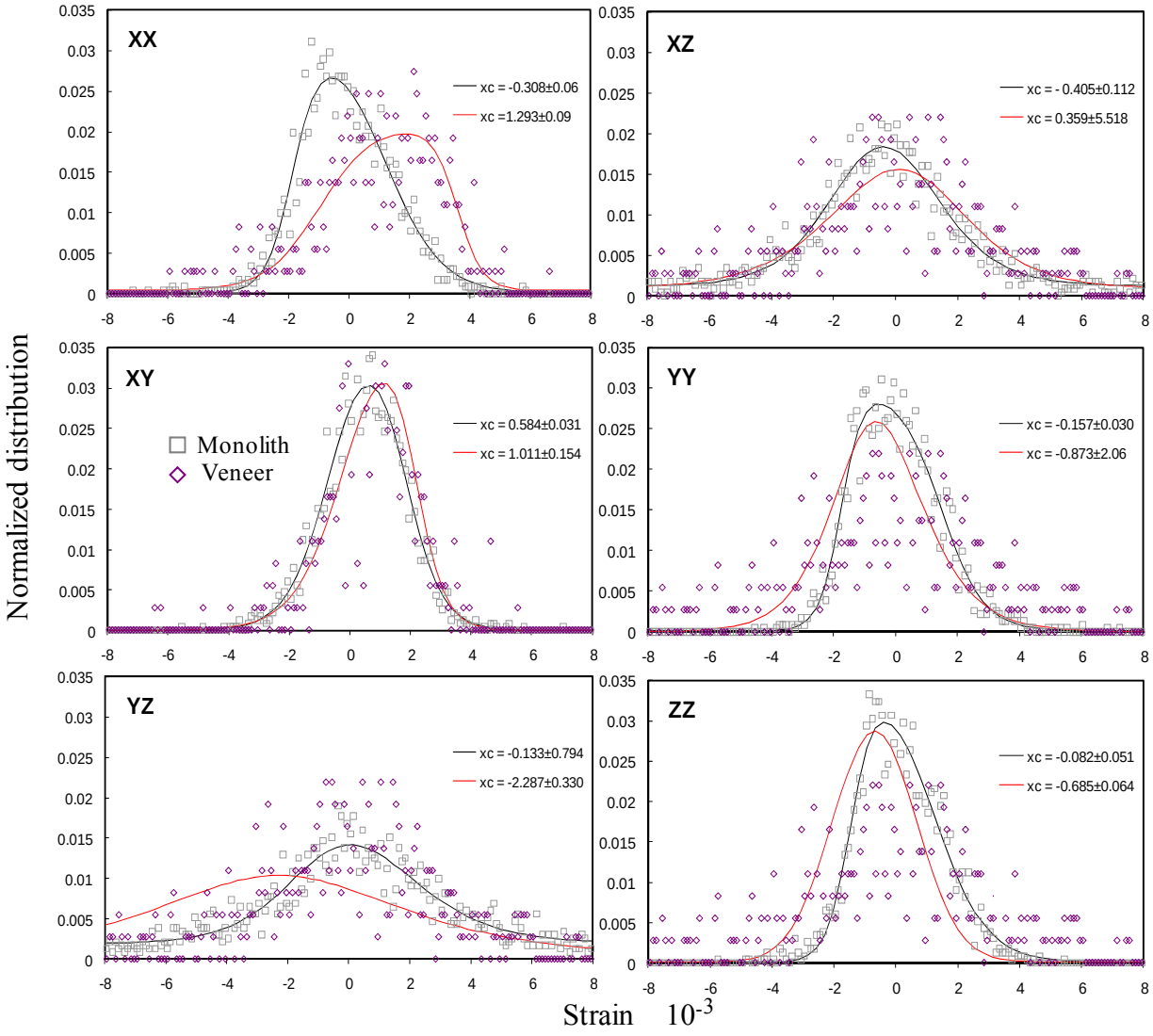

Figure 25 Type II Residual Strain distribution in Zirconia and Interface Residual Stress in Porcelain veneered Zirconia. xc indicates the center of the distribution obtained through the sigma2 fit function for different datasets.

Based on the values of the deviatoric stress component it is possible to derive the Von Mises stress value using Equation 5. The Von Mises stress is a convenient measure to express the overall residual stress state in a particular sample and observe the change in stress state as certain physical parameters change, for instance addition of the veneer layer. Von Mises

stress gives a general idea of the stress state which is difficult to otherwise interpret with individual directional components of stress. Table 4 tabulates the Von Mises strain for a monolith zirconia and a veneered zirconia sample. A relative type I stress change of 577 MPa was observed after sintering a porcelain veneer layer on the zirconia surface.

$$\sigma_v = \sqrt{3J_2}$$

$$\sigma_v = \sqrt{\frac{(\sigma_{11}-\sigma_{22})^2 + (\sigma_{22}-\sigma_{33})^2 + (\sigma_{33}-\sigma_{11})^2 + 6(\sigma_{12}^2 + \sigma_{23}^2 + \sigma_{31}^2)}{2}} \qquad \text{(Eqn. 5)}$$

Table 4 Area averaged (Type I) Von Mises stress of a monolithic and porcelain veneered zirconia model composite.

Stress (MPa)	**XX**	**XY**	**XZ**	**YY**	**YZ**	**ZZ**	**Von Mises Stress (MPa)**
Monolith	-79	112	-64	-64	38	-65	233
Veneered	267	183	2	-96	-365	-143	807
							$\Delta\sigma_{\text{Von Mises}}$ = **577 MPa**

Based on the deviatoric stress components found in the monolithic zirconia, the principal minimum and maximum stresses and corresponding direction vectors were determined. A maximum principal stress of 43 MPa and a minimum principal stress of -218 MPa exists on the monolith zirconia surface.

The maximum and minimum principal stresses on the zirconia underneath the porcelain layer were determined to be 399 MPa and -506 MPa respectively. The direction of the principal minimum and maximum stresses in the case of the monolith and veneered core are shown in

Figure 26. The principal stress values and their corresponding direction vectors are tabulated in Table 5.

Table 5 Resultant principal minimum and principal maximum stress in the monolith zirconia and veneered zirconia along with their corresponding direction vectors. The eigen values and eigen vectors were derived from the deviatoric stress tensor which neglects the contribution of hydrostatic stress.

		Direction Vectors		
		x	**y**	**z**
Monolith	Stress (MPa)			
Principal Max	43	-0.713	-0.677	0.183
Principal Min	-218	0.677	-0.597	0.430
Veneer				
Principal Max	399	-0.753	-0.548	0.365
Principal Min	-506	0.167	-0.695	-0.699

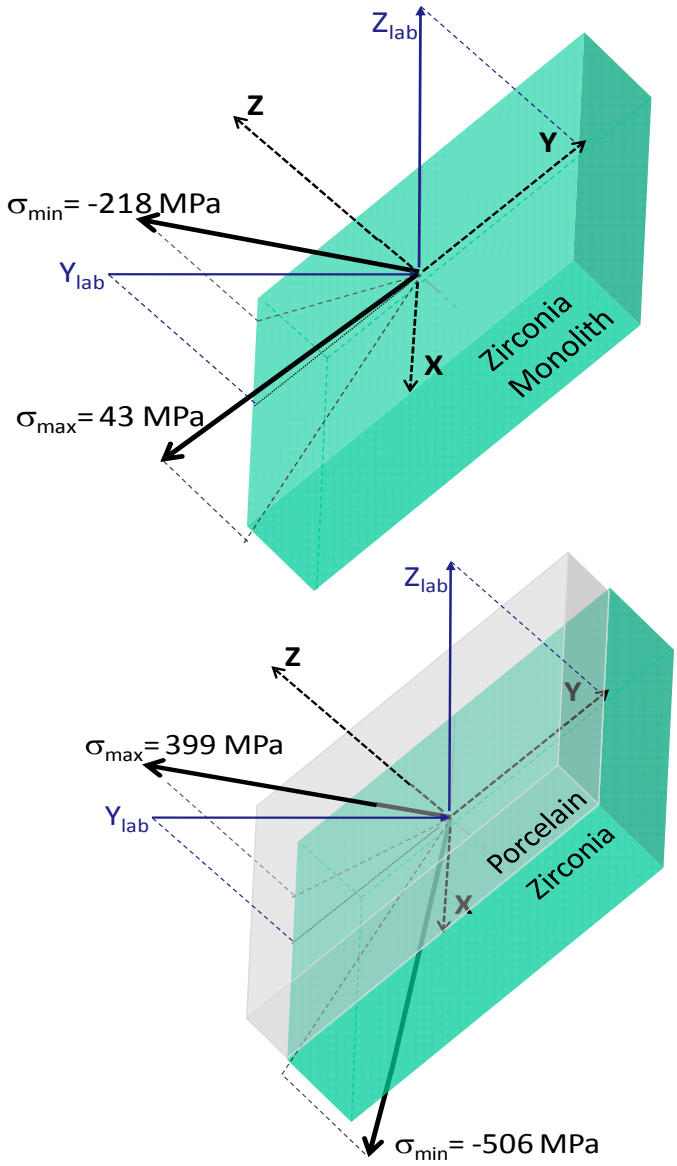

Figure 26 Resultant principal maximum and principal minimum stresses in the monolith zirconia (top) and veneered zirconia (bottom). The direction of the vectors is indicated with respect to the sample oriented at 45° on the stage.

3.9 Effect of cyclic impact loading on monolithic zirconia

Monolithic zirconia samples were subjected to 2 sets of fatigue cycles – 40,000 & 180,000 cycles, after the initial residual stress states were measured. The number of load cycles was decided based on literature values. [7-8] The monolithic disk samples were mounted on polymer bases which simulate the dentin layer. [8] The disk samples were mounted on a high precision kinematic base and fatigued in the custom built load frame at a frequency of 2 cycles/second with a load of 150 N using a 1.9 mm tungsten carbide ball indenter. The kinematic base ensures accurate alignment of samples on the translation stage after a particular cyclic loading step. Sample registration with an accuracy of 1 micron is achievable using TiO_2 marker dots. The area under the indenter and in the vicinity of the indenter was mapped for both the 40k and 180k cyclic fatigue steps. Results of the analysis of the different cyclic fatigue steps on the neat zirconia are shown in Figure 27.

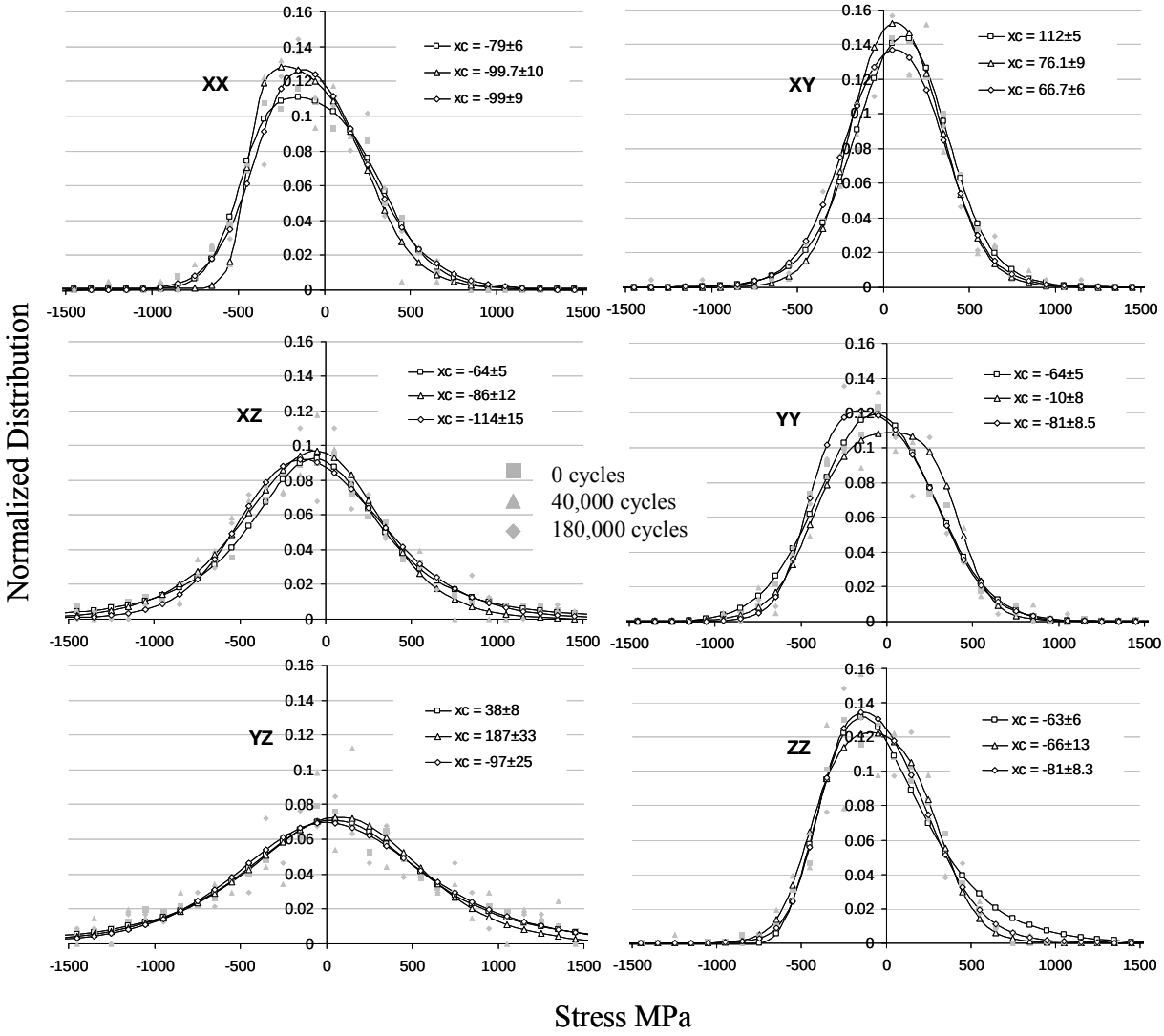

Figure 27 Influence of fatigue cycling on residual stress state in neat zirconia. The type I stress is obtained from grains averaged from a rectangular area under the indenter extending 100 micrometer away from the indenter. Solid lines with the open symbols indicate the asymmetric sigma fit to the data (solid symbols).

No significant change in the Type I residual stress was observed with increasing fatigue cycles, in any particular direction. However an in-depth observation of the grain-to-grain local stresses (Type II) at the indentation site is vital to studying damage evolution due to impact fatigue.

3.9.1 Effect of impact fatigue on porcelain-veneered zirconia composite

The experimental procedure employed to fatigue the neat zirconia disks described in section 6.3 was utilized to determine the effect of cyclic fatigue on the change in residual stress state. The layered porcelain veneer composite is of particular interest since it represents the typical specifications of a clinically relevant sample with a simplified geometry. Due to beam time constraints only 40,000 load cycles could be implemented on the porcelain veneered zirconia sample. A significant change in Type I residual stress was observed in this case. A net residual stress change of -652 MPa ($\sigma_{\text{Von Mises}}$) was observed as a result of the fatigue cycles. There is a relative stress change from 807 MPa on an intact porcelain veneered sample, to 154 MPa after application of 40,000 cycles. This result indicates that cyclic fatigue at a relatively small load does change the state of residual stress in the sample. The components of Type I stress from the fatigued porcelain veneered zirconia sample are summarized in Table 6.

Table 6 Residual stress and strain values averaged over many grains (Type I). The result of applied fatigue load cycles on the veneered composite is summarized. The layered veneer composite was subjected to 40,000 load cycles at 150N.

Stress (MPa)	XX	XY	XZ	YY	YZ	ZZ	Von Mises Stress (MPa)
Veneer (0 cycles)	267	183	2	-96	-365	-143	807
Veneer(40k cycles)	47	31	-68	24	-47	31	154
Δ stress	-219	-152	-70	120	318	174	-652

Table 7 Principal minimum and maximum residual stress derived from the deviatoric components of stress for veneer sample before and after fatigue.

Stress (MPa)	Principal Minimum	Principal Maximum
Veneer (0 cycles)	-218	43
Veneer (40k cycles)	-506	399

3.10 Discussion

The analysis of raw Laue diffraction images leads to a sequential list of the refined strains. The distribution of the six deviatoric components of stress and strain, from the scanned area consisting of 6000 data points from a monolithic neat zirconia disk is presented in Figure 28.

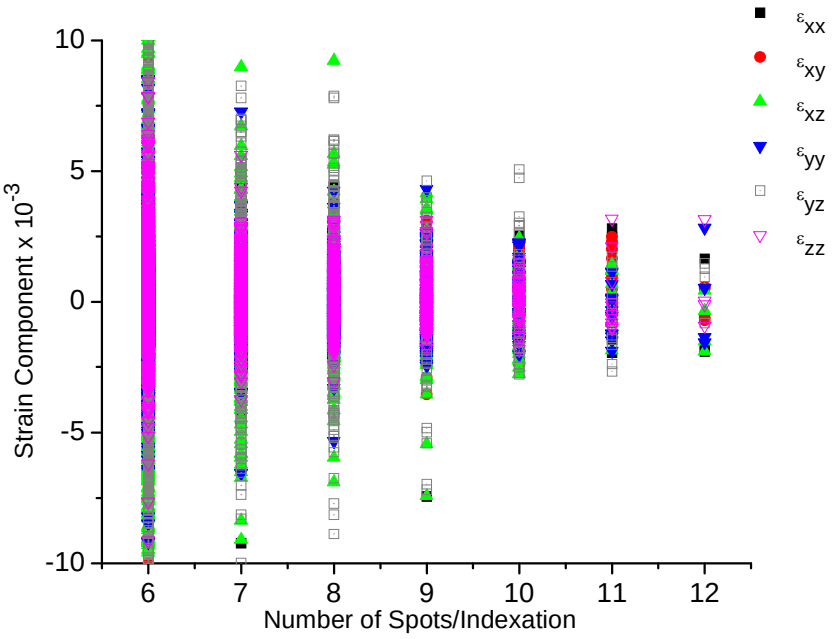

Figure 28 Illustration of strain magnitude and number of spots used per indexation. The accuracy of strains is low for less number of indexed peaks

The output of the analysis consists of the strain components which are transformed to stress components using the stiffness tensor [10] for tetragonal zirconia. Results indicate that there exists on average, a relatively small compressive stress at the surface between 47 and 75 MPa

depending on direction. However, more than a few grains, between 10-25% depending on the direction, reached stresses up to 1 GPa. Large compressive and tensile strains up to 5000×10^{-6} were observed. [12] The beam cross section, nominally 500 nm × 500 nm, provided 1- 3 indexed grains. Typically only one grain per exposure had sufficient intensity for strain refinement. Such strains have been previously observed in graded alumina zirconia components, and zirconia disks. [50-53]

Observed in the Laue pattern are a large number of spots, which were due to the small grain size. The results were obtained by analyzing only the tetragonal phase for indexation due to the relatively brighter peaks and high symmetry. Indexation of the monoclinic phase is more computationally intensive. Figure 28 shows the influence of the grain index number on the strain accuracy. It was observed that a low error in strain was obtained when 12 or more spots were used in a particular indexation. The error increases as lesser spots are utilized per indexed grain since there is less constraint. This aspect of the experiment can be significantly altered by optimizing the sample-to-CCD distance.

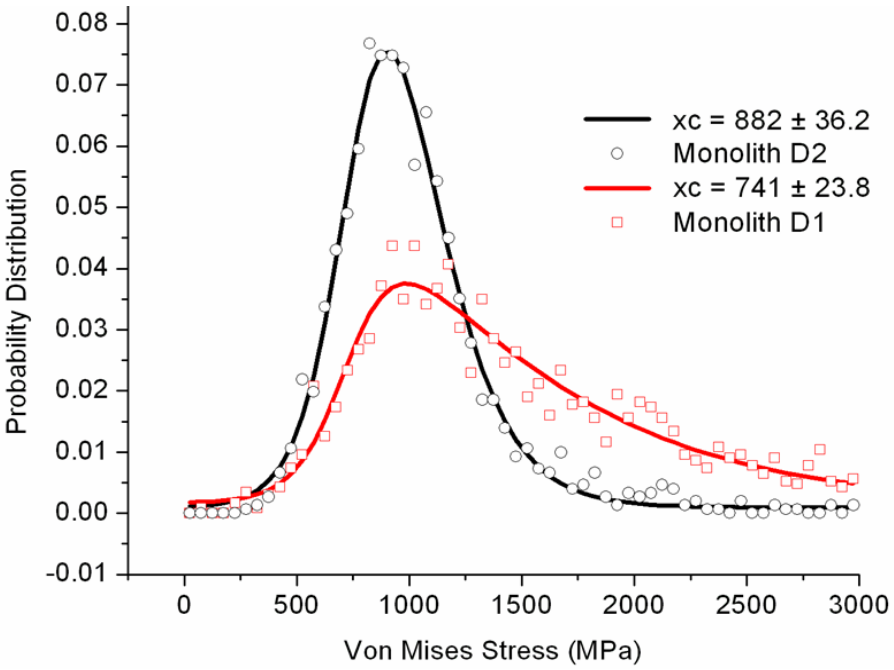

Figure 29 Probability distribution function of the Von Mises stress for distance D1 and D2 on the monolith surface of zirconia.

A smaller camera distance creates more spots on the CCD and hence more constraint in determining the strain. However this is accompanied by a lesser peak accuracy. The optimum camera distance is one which is has the best resolution per spot and has an optimum number of spots. The resolution per spot reduces as the camera distance is decreased since the number of spots captured increases and the number of pixels per spot reduces. Probability distribution plots of the Von Mises stress for the dataset corresponding to two different sample-to-camera distance D_1 (long distance) and D_2 (short distance) were generated as shown in Figure 29. A significant observation of this experiment is the occurrence of a large fraction of the grains at a considerably high stress. The dataset corresponding to long distance, D_1, has a peak center at 741 MPa and has a trailing tail in the direction of high stress values which is due to the low strain accuracy as a result of fewer peaks. On the other hand, a comparatively uniform distribution centered around 882 MPa of

stress is seen in the dataset corresponding to the near distance, D_2. Considering the dataset corresponding to D_2 it was observed that at least 42% of the overall indexed grains lie in the range of 800 - 1000 MPa.

Table 8 Deviatoric stress (Type I) values in MPa derived from the distribution of stress components in individual directions (Type II) for zirconia monolith. Von Mises stress has been calculated for the two datasets based on the Type I stress components.

Dataset	xx	xy	xz	yy	yz	zz	Von Mises Stress
Monolith D_2	-104	-4	6	-165	51	-71	121
Monolith D_1	-79	112	-64	-64	38	-65	233

Table 8 shows tabulated values of the stress components in individual directions along with the corresponding Von Mises stress value for the monolith zirconia. The Von Mises stress value should approximately represent the macroscopic stress state of the sample. It can be observed that the macroscopic Von Mises stress derived from several grains was significantly smaller than the one observed in the local grain domain.

Polychromatic diffraction patterns were obtained along a 0.75 mm long line scan on the surface of monolithic zirconia. The deviatoric strain tensor for each scan point was determined through indexing. Figure 30 (top) shows a plot of the principal deviatoric stress component in the XX direction along the line scan. Figure 30 (bottom) is an inset of the line scan indicating typical large local stress at a grain in the line scan. The trend demonstrated in the line scan is typical of all the line scans that comprise the area scans. Average variations of stresses were typically smaller than ±500 MPa with a small amount of localized high

stress values close to ±1 GPa at a few locations along the line scan (roughly 25 % of indexed grains).

A typical deviatoric strain and stress tensor derived from the analysis of one Laue diffraction image from a 1 μm spatial resolution line scan on monolith zirconia is shown below. The deviatoric stress (σ^n) and strain tensors (ε^n) for two different grains with close to 1 GPa stress (indicated in red circles in Figure 30) are shown below. '*n*' indicates the grain in Figure 30.

$$\sigma^{(1)} = \begin{pmatrix} 823 & -821 & 1405 \\ -821 & 174 & 779 \\ 1405 & 779 & -428 \end{pmatrix}$$

$$\varepsilon^{(1)} = \begin{pmatrix} 4775 & -3759 & 6945 \\ -3759 & -997 & 3846 \\ 6945 & 3846 & -3752 \end{pmatrix} \times 10^{-6}$$

$$\sigma^{(2)} = \begin{pmatrix} -915 & -174 & 402 \\ -174 & 44 & 770 \\ 402 & 770 & 388 \end{pmatrix}$$

$$\varepsilon^{(2)} = \begin{pmatrix} -3145 & -872 & 1810 \\ -872 & 862 & 3362 \\ 1810 & 3362 & 2306 \end{pmatrix} \times 10^{-6}$$

The large stress values indicate the presence of a fraction of grains with highly localized stresses. Considering the aspects of damage tolerant properties of ceramics, the ultimate performance of a given ceramic depends on how minimal the defects in a given system are. The number of occurrences of high stress concentration sites in a ceramic can govern the property of fracture resistance. Hence knowledge of the distribution of the localized stresses is paramount. Measurement of the localized, type II, high magnitude stresses is extremely challenging. However, the small probe size and high sensitivity of the polychromatic Laue-diffraction technique to lattice distortions makes it a highly valuable and unprecedented type II residual stress measurement method.

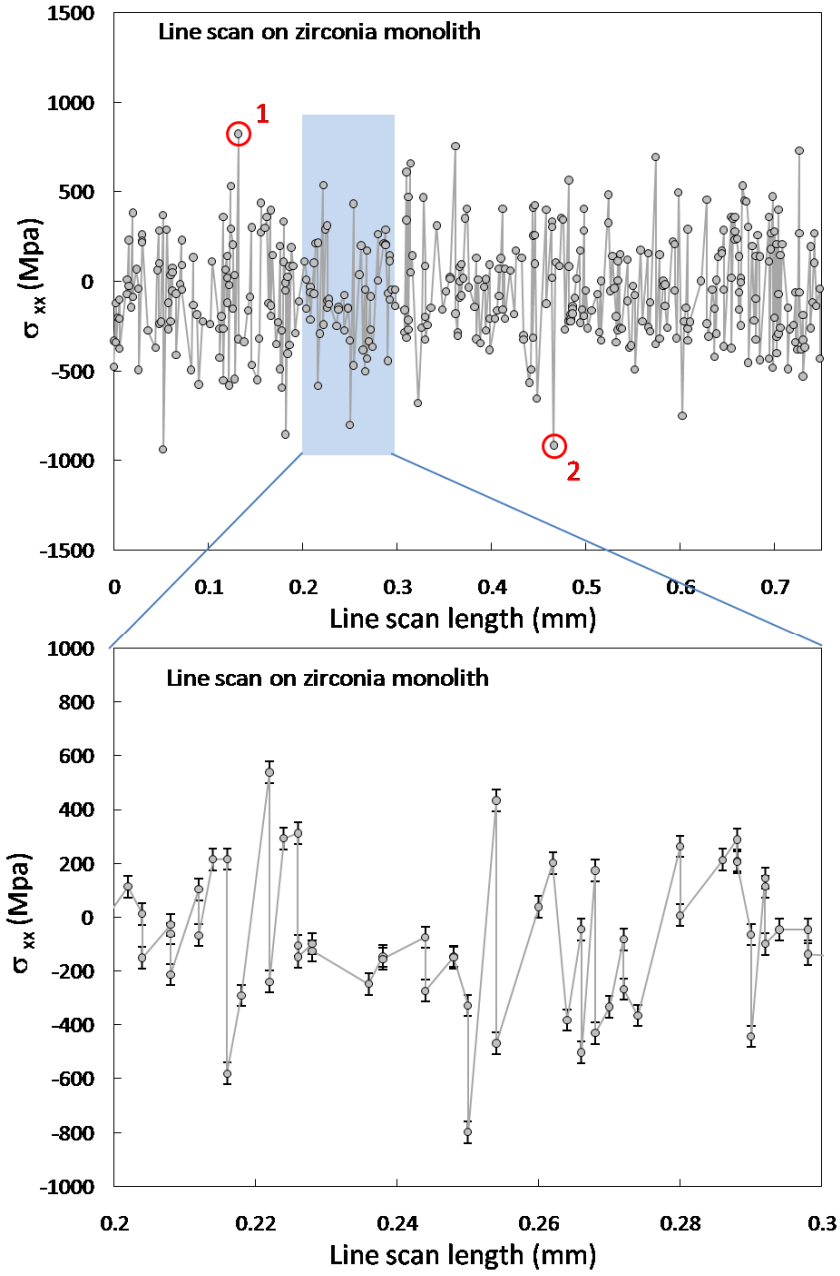

Figure 30 Deviatoric stress component in the XX direction is shown along a high resolution line scan on monolith zirconia (top). The average variation in the type II stress was in between ± 500 MPa. Spikes in the stress value close to 1 GPa were evident, indicative of highly stressed grains, roughly 25 % of total grains observed. Inset shows a close-up of the variations in a part of the line scan (bottom).

A significant observation of this study has been the relative change in the Type I residual stress, represented by a Von Mises stress, which changed from 233 ± 50 MPa for the monolithic zirconia to 807 ± 50 MPa when the monolith was coated with porcelain veneer. The relative change in residual stress, around 575 MPa, was caused by placing the veneer surface on the monolith. A significant change in stress state from a compressive stress of 807 ± 50 MPa to 154 ± 50 MPa after a cyclic fatigue loading was also observed.

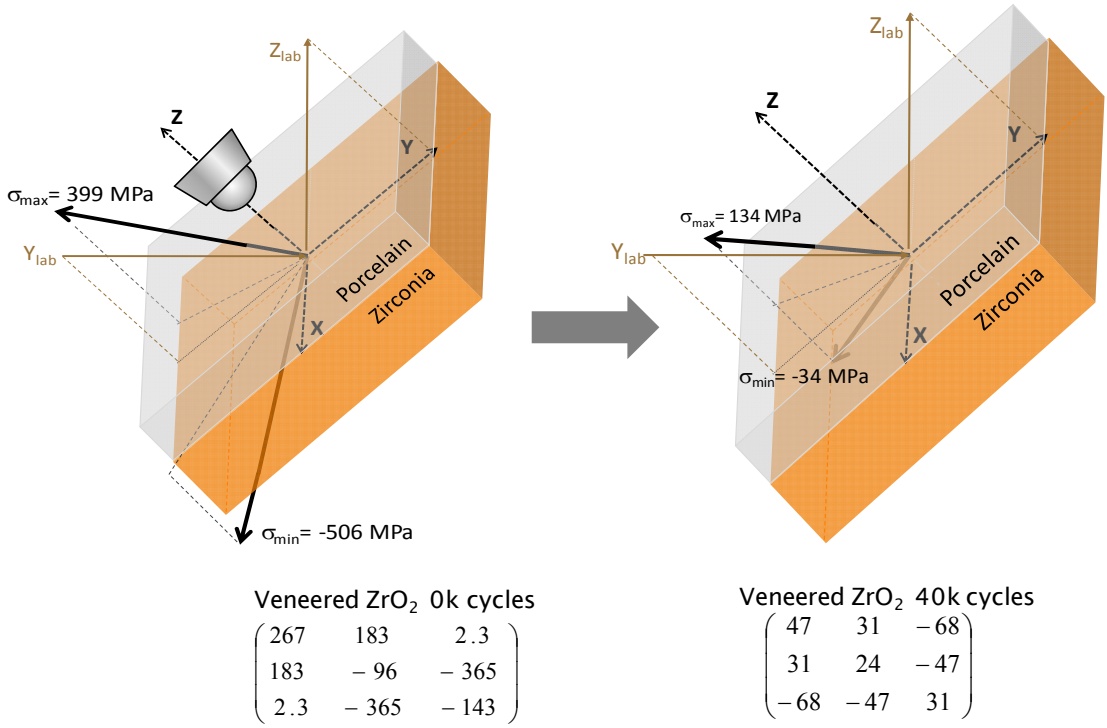

Veneered ZrO_2 0k cycles

$$\begin{pmatrix} 267 & 183 & 2.3 \\ 183 & -96 & -365 \\ 2.3 & -365 & -143 \end{pmatrix}$$

Veneered ZrO_2 40k cycles

$$\begin{pmatrix} 47 & 31 & -68 \\ 31 & 24 & -47 \\ -68 & -47 & 31 \end{pmatrix}$$

Figure 31 Resultant principal maximum and principal minimum stresses in the intact veneered zirconia (left) and veneered zirconia subjected to 40,000 fatigue cycles (right). The direction of the vectors is indicated with respect to the sample oriented at 45° on the stage.

Deviatoric stresses seen at the interface of the veneered zirconia composite were observed to reduce significantly to less than 100 MPa in any given direction (as indicated by the tensors in Figure 31). The relaxation of compressive residual stresses to a state similar to

monolithic zirconia within 40,000 fatigue cycles (which is equivalent to one year's service life in a patient) [6], suggests that the resulting relaxed base must undergo subsequent fatigue cycles under a tensile stress pattern, which hypothetically leads to catastrophic failure of the restoration.

The magnitude of change in residual stress between different fatigue steps is significant and provides context for explaining the commonly observed interfacial cracking in ceramic dental restorations. The change in stress state, starting from a compressive stress towards a tensile stress state can be detrimental to clinical performance where complex geometries along with an aggressive mechanical and chemical environment may synergistically contribute to clinical failures of zirconia all-ceramic dental crown systems. However, these stresses were only measured in the zirconia base layer and were presumed to be balanced by the porcelain layer. Modeling of these stress states is necessary to fully interpret these results.

With no surface treatment or presence of overlying layer, the surface stress on monolithic zirconia is anticipated to be zero. The probe cross section being very close to the size of a grain, we observed stress/strain values from individual grains. The measured stresses are far from zero locally (Type II) but zero globally (Type I).

3.11 Conclusions

Grain-grain residual stresses were observed at a grain resolution including 2500 grains over a macroscopic area in a zirconia ceramic disk. Laue patterns from yttria stabilized zirconia were obtained with a highly focused polychromatic X-ray beam. On average, around 300 reflections were observed for the zirconia sample consisting of 0.1 - 0.3 μm sized grains with an incident beam spot of 500 nm x 500 nm nominal size. Approximately 5 percent of the reflections were brilliant and indexed to the tetragonal phase of zirconia. It was observed that large variations in Type II residual stresses ranging from – to + 1 GPa were observed between grains. Along with the high stress values in monolithic zirconia, a significant relaxation of the compressive residual stresses has been observed in a porcelain veneered zirconia composite due to fatigue. Such high residual stress concentration may be detrimental to clinical performance where complex geometries along with a mild mechanical and chemical environment may synergistically contribute to clinical failures of zirconia all-ceramic dental crown systems. Veneering the zirconia monolith induced a compressive residual stress in zirconia. The measured deviatoric stresses can be interpreted as a Von Mises thermal residual stress close to 800 MPa. These values of stress, averaged over many grains in the scan area, represent the macroscopic residual stress.

CHAPTER IV

4 GRAIN AVERAGED MICRO-SCALE RESIDUAL STRESS MEASUREMENT USING MONOCHROMATIC SYNCHROTRON X-RAYS

4.1 Introduction

The information on the residual stress state inferred from the polychromatic micro diffraction technique is limited to the extent of a few grains. In order to acquire knowledge of the stress state on a large area with the small polychromatic micro-diffraction probe size (0.7 μm x 0.8 μm), several hundred diffraction scans would be required. Moreover, the results of the diffraction scans were obtained through a highly specialized peak indexation post-processing. Since micro-diffraction is sensitive to the grain-to-grain interaction and anisotropic effects, wide variations in stress were observed at that length scale. The use of 2D micro-diffraction with a wider beam cross-section (2 μm x 10 μm) and monochromatic X-ray radiation can provide information of the stresses from several grains in a single exposure. Additionally, the technique inherently provides a grain averaged result (Type I stress), eliminating the need to take several scans and average the results.

4.2 Theory

Measurements of strain using x-ray diffraction experiments involve accurately determining the position of the diffracted beam. The position determined, can readily be converted to corresponding 'd-spacing' based on Bragg's law. The strain can be calculated by determining the difference in measured (d) and unstressed plane spacing (d_o). The accuracy of the strains measured using d_o are greatly dependant on how precisely the d_o value is determined.

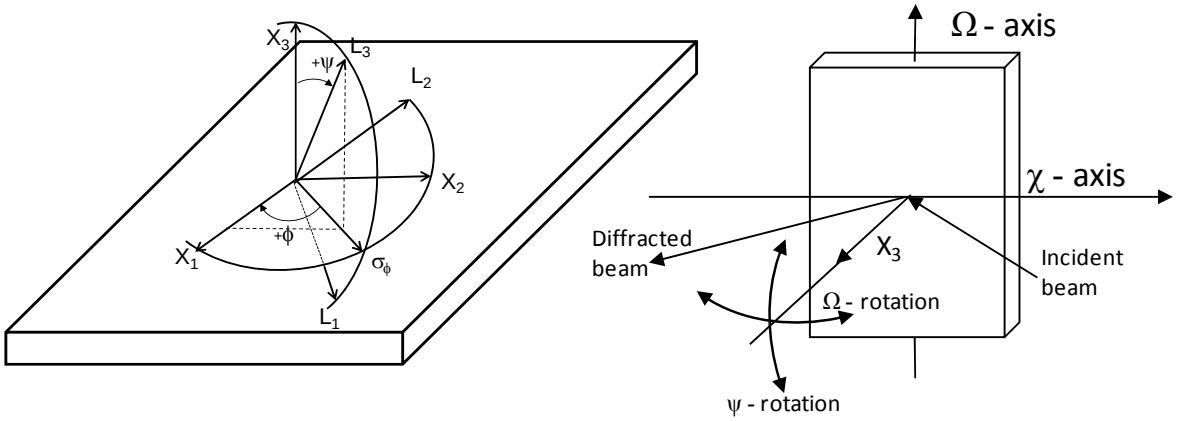

Figure 32 Illustration of the sample (X_i) and Laboratory (L_i) coordinates along with the angles ψ and ϕ. (adapted from [54])

Although there are many ways to evaluate d_o, in practice the exact value of d_o for a given sample may not be easily available. In such a circumstance, simply measuring the relative change in the lattice planar spacing can provide enough information to derive the relative strains.

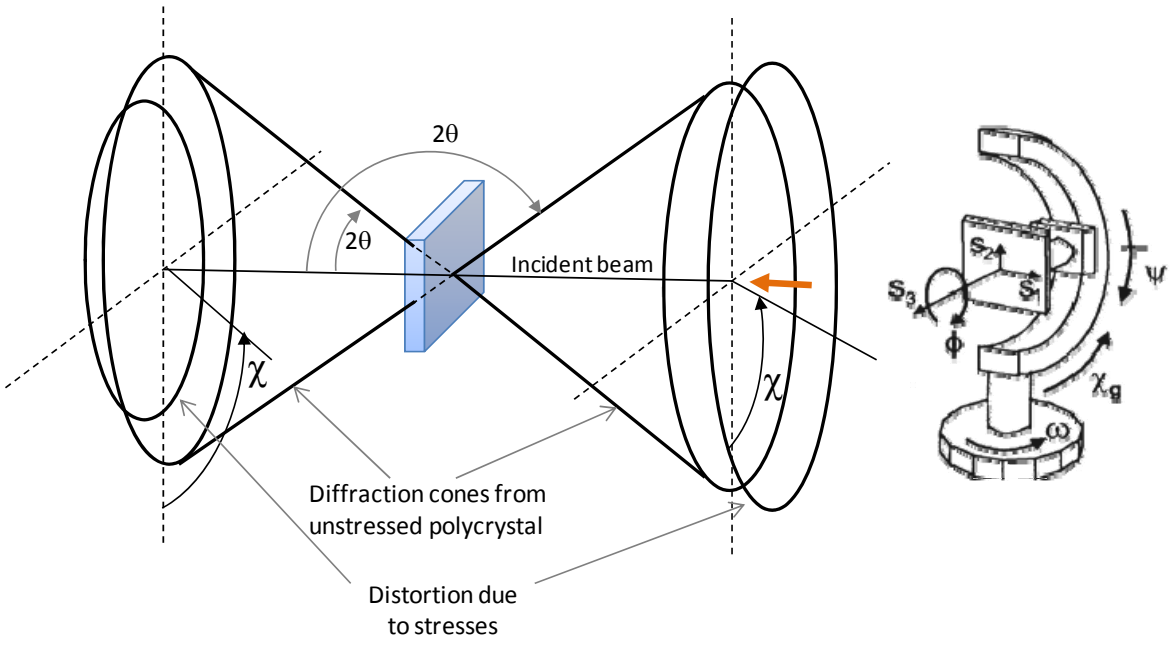

Figure 33 Illustration of the forward and diffraction cones from the sample. Also indicated are diffraction rings that result from lattice distortions. (Right) shows a schematic of the goniometer geometry and the respective sample coordinates S_i (figures adapted from [54])

Figure 32 & Figure 33 indicate sample and laboratory coordinates and various angles that need to be understood in a typical diffraction experiment. Figure 33 demonstrates the schematic of diffraction from a sample with stressed and unstressed crystals.

The fundamental equation of x-ray strain determination is given by [55-56]

$$\left(\varepsilon'_{33}\right)_{\phi\psi} = \varepsilon_{11}\cos^2\phi\sin^2\psi + \varepsilon_{12}\sin 2\phi\sin^2\psi + \varepsilon_{22}\sin^2\phi\sin^2\psi + \varepsilon_{33}\cos^2\psi + \varepsilon_{13}\cos\phi\sin 2\psi + \varepsilon_{23}\sin\phi\sin 2\psi \quad \text{(Equation 6)}$$

The fundamental equation in terms of stress is expressed as

$$\frac{d_{\phi\psi}-d_0}{d_0} = \frac{1+\nu}{E}\{\sigma_{11}\cos^2\phi+\sigma_{12}\sin 2\phi+\sigma_{22}\sin^2\phi-\sigma_{33}\}\sin^2\psi+\frac{1+\nu}{E}\sigma_{33}-\frac{\nu}{E}\{\sigma_{11}+\sigma_{22}+\sigma_{33}\}+ \frac{1+\nu}{E}\{\sigma_{13}\cos\phi+\sigma_{23}\sin\phi\}\sin 2\psi \quad \text{(Equation 7)}$$

Considering the penetration depth of x-rays into the surface to be considerably minimal, we can simplify the above equation under the assumption that a biaxial stress state is observed. Hence the equation is,

Given by $\varepsilon_{\phi\psi} = \frac{d_{\phi\psi} - d_0}{d_0} = \frac{1+\nu}{E}\sigma_\phi \sin^2\psi - \frac{\upsilon}{E}(\sigma_{11} + \sigma_{22})$

Where σ_ϕ, the stress component along the X_ϕ direction is given by

$$\sigma_\phi = \sigma_{11}\cos^2\phi + \sigma_{12}\sin 2\phi + \sigma_{22}\sin^2\phi \qquad \text{(Equation 8)}$$

Further re-arranging the terms leads to –

$$d_{\phi\psi} = d_0\frac{1+\nu}{E}\sigma_\phi \sin^2\psi - d_0\frac{\upsilon}{E}(\sigma_{11} + \sigma_{22}) + d_0$$

$$Slope = \frac{d_{\phi\psi}}{\sin^2\psi} = d_0\frac{1+\nu}{E}\sigma_\phi \approx d_{\psi=0}\frac{1+\nu}{E}\sigma_\phi$$

$$\sigma_\phi = \frac{slope}{d_{\psi=0}}.\frac{E}{1+\nu} \qquad \text{(Equation 9)}$$

The value of slope was determined through the plot of $\sin^2\psi$ and d-spacing as shown in Figure 38.

Micro-diffraction in the $\sin^2\psi$ measurement mode has been previously used in determining biaxial residual stresses. [56-58]

4.3 Method

4.3.1 Specimen fabrication

Specimens comprising of dental crowns made in a clinical dental laboratory, were provided by our collaborators (NYU School of Dentistry) specialized in the field of restorative dentistry. Sample preparation was based on their adopted approach and is mentioned elsewhere. [59]

Plastic models were generated (Figure 34a) on a milling machine based on the CAD files of the prepared tooth model. These models were further placed in a dental articulator (Figure 34b) where they were subject to opposing and adjacent dentition. A CAD/CAM milling center (3M/ESPE, St. Paul, MN) was utilized to fabricate 0.5 mm thick zirconia cores (3M/ESPE, St. Paul, MN). The input parameters were obtained from the impressions (Aquasil, Dentsply, York, PA) of the prepared, adjacent and opposite teeth. A commercial dental laboratory (Marotta Dental Studio, Huntington, NY) carried out the veneering process, wherein the fabricated cores were coated with porcelain slurry (LAVA Veneer, 3M/ESPE, St. Paul, MN) according to an appropriate clinical fit and then fired.

A batch of prepared tooth replicas were fabricated from high modulus polyvinylsiloxane impressions (Aquasil, Dentsply, York, PA) of the machined plastic models. The impressions were filled with layers of resin-based composite (Z100, 3M/ESPE, St. Paul, MN) and cured according to the manufacturer's recommendations.

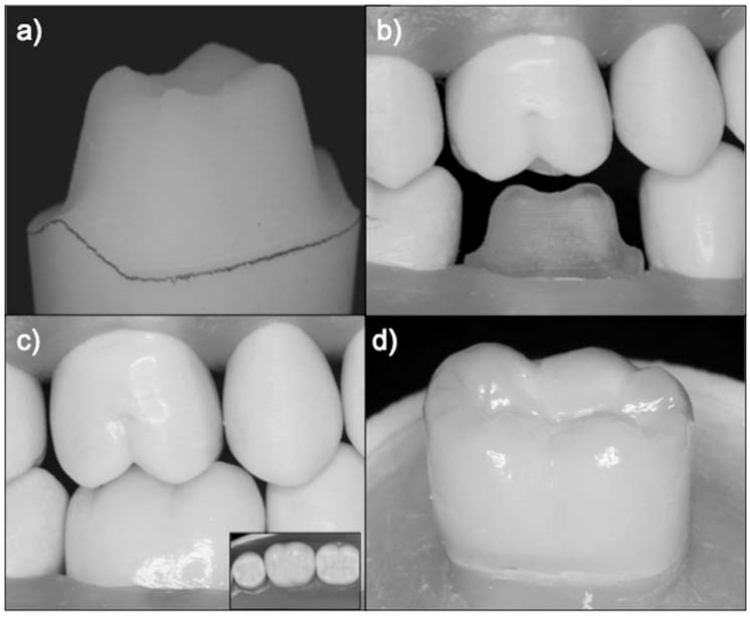

Figure 34 a) Plastic model through CAD based replication of the prepared tooth. b) Placement of the plastic model in the dental articulator with opposing dentition. [59]

The replicas were stored in distilled water at 37^{o}C for at least 30 days to assure hydration and eliminate any effects of water uptake dimensional expansion after crown cementation. At cementation, a layer of metal primer (Alloy Primer, Kuraray, Ltd, Osaka, Japan), was applied to the internal surface of the zirconia core (no sandblasting was employed). The crowns were then cemented (RelyX Unicem, 3M/ESPE) under a 10N load onto the following tooth replica. The crown-tooth replica was embedded in acrylic resin (Orthoresin, Degudent, Main, Germany) in a 1-inch diameter PVC tube. The crown buccal margin was placed 2 mm above the surface of the resin with the long axis of the crown-tooth replica and tube aligned (Figure 34d). Specimens were stored in water.

4.3.2 Sliding-Contact Mouth-Motion Step-Stress Fatigue (SCSSF)

One week after cementation, three crowns were subjected to single load to failure. Sliding-contact mouth-motion step-stress fatigue was then performed on the remaining crowns. For

SCSSF, the specimens were attached to a servo-all-electric system (800L, TestResources, Shakopee, MN), and subjected under water to one of three step-stress profiles following the distribution 4:2:1 (light, moderate, and aggressive profiles respectively based upon the single load to fracture mean value) and tested until failure or survival. All mechanical testing was performed with a tungsten carbide indenter of 6.25 mm diameter sliding 0.7 mm lingually down the disto-facial cusp, beginning at 0.5 mm lingual to the cusp tip, simulating aspects of natural occlusion.

Initial experiments were performed to measure the interface residual stress by the x-ray beam penetrating through the porcelain of an un-cut intact crown. However due to the high absorption through the porcelain layer, along with irregular porcelain thickness, sufficiently bright diffraction peaks were not achievable. Due to this constraint, it was decided to carry out a bi-axial surface measurement of the interfacial stress in the zirconia crowns.

The crown samples were wet sectioned diagonally into two halves using a low speed diamond saw. The sectional cut was positioned such that it super-imposed the cusp which was subjected to cyclic fatigue. Sectioned test specimens were prepared from an intact crown and crown with SCSSF, which had undergone 45,000 cycles of impact fatigue at a 150N compressive load.

The half sections were then mounted onto aluminum mounting tabs using a high strength rapid setting epoxy glue. Care was taken to maintain the sectioned face, parallel to the surface of the mounting tab. The mounting tabs were attached to high precision kinematic bases which facilitate quick and precise alignment on the diffraction stage. Since the tabs

were fixed to the base with a set screw, this mechanism provided freedom in rotating the sample about the surface normal.

4.3.3 Synchrotron setup

The residual stress measurements were conducted on the same setting explained in the chapter related to polychromatic diffraction. A major advantage of the setup was that both polychromatic and monochromatic experiments can be done on the same setup since both beam paths are collinear. Switching between the two beams can be done by rotating the 4-crystal Si monochromator. When aligned parallel to the beam, the beam passes without interfering with the crystals and a polychromatic beam was obtained, which further passes through the focusing optics. In the case of the monochromatic beam, the energy can be tuned between 5 keV and 14 keV. An X-ray energy of 7 keV was chosen to perform the experiment. At higher energy, the diffraction cones shift towards the lower 2θ, and are spaced closely. This leads to a reduction in the resolution per ring. The CCD has 1024 x 1024 pixels and has a resolution of 160 μm/pixel. The CCD covered a two-theta range of 51^{o} to 131^{o}.

The X-ray spot size incident on the sample was focused to a cross section of 10 μm (horizontal) x 2μm (vertical) using a pair of elliptically bent Kirkpatrick-Baez mirrors. Sample orientation was the same as in the polychromatic beam experiment in 90^{o} reflection geometry. The sample-to-camera distance was 78.9 mm, which was determined based on the polychromatic experiment. Prior to conducting the experiment, accurate calibration of distance and camera tilts was done by collecting a polychromatic diffraction pattern from a single crystal silicon placed on the sample. The intensity flux of the beam and energy was tuned by collecting a monochromatic diffraction pattern from the single crystal silicon. It is

critical to align the diffraction surface at the focal point where beam divergence is minimal. This step was carried out using the laser alignment device explained in detail in Chapter 3. Figure 35 is a schematic of the orientation of the sample and the camera with respect to the incoming beam. The diffracting cones corresponding to the lower and higher 2θ angles are also indicated. The diffraction rings obtained by the CCD camera are due to the intersecting arc of the diffraction cone with the plane of the CCD.[60]

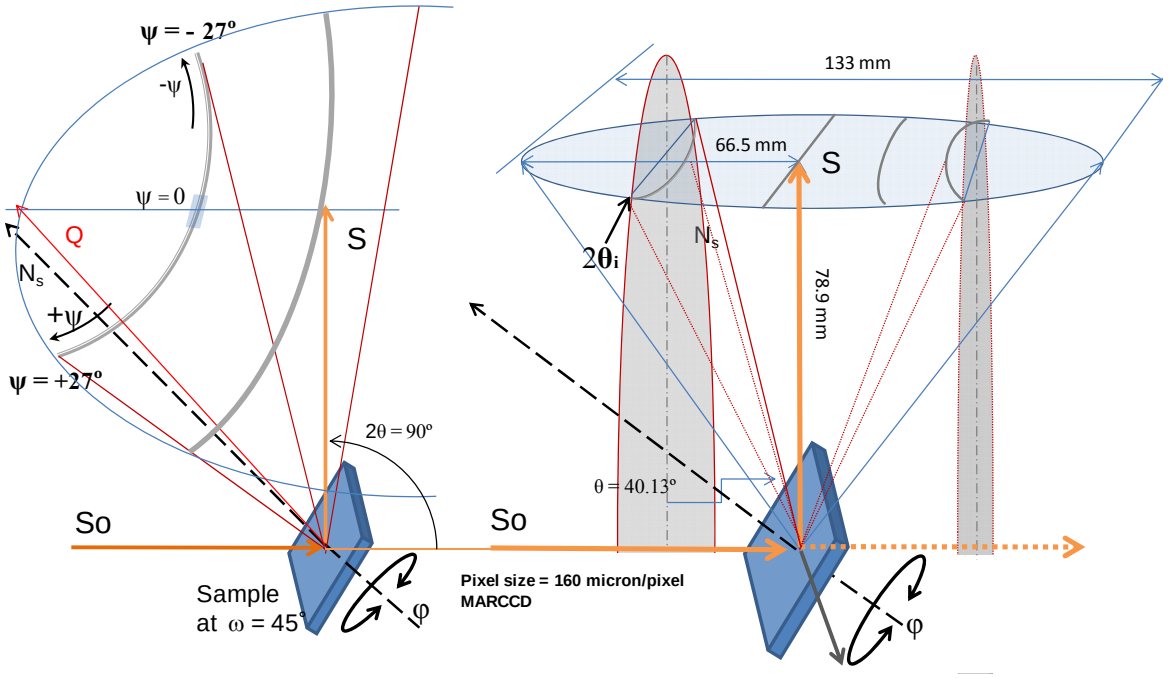

Figure 35 Schematic of the sample orientation and position of the CCD with respect to the diffraction cones. ψ is the angle subtended by the diffraction rings on the CCD. for a sample-to-CCD distance of 78.9mm the maximum psi angle subtended was +27° to - 27°.

Also indicated are the different orientation angles of the CCD and the sample. The sample rotation along ϕ was fixed for a particular location of the sample. Since the interface layer had an irregular contour, the sample was appropriately rotated such that the interface was

always parallel to the plane of the beam. Aligning the veneer-core interface with respect to the diffraction vector is important since it decides the stress component being measured.

4.3.4 Crystallographic information of zirconia

The zirconia core was made of yttria stabilized tetragonal polycrystalline zirconia with grain sizes on the order of 0.1 – 0.3 μm. The tetragonal poly-crystal structure can undergo stress induced phase transformation and form a low symmetry monoclinic crystal, with a larger lattice volume. Figure 36 indicates a simulated fit based on a powder diffraction file (PDF) of a zirconia tetragonal crystal. The PDF file contains information pertaining to the d-spacing of the different diffracting planes along with the corresponding relative intensity.

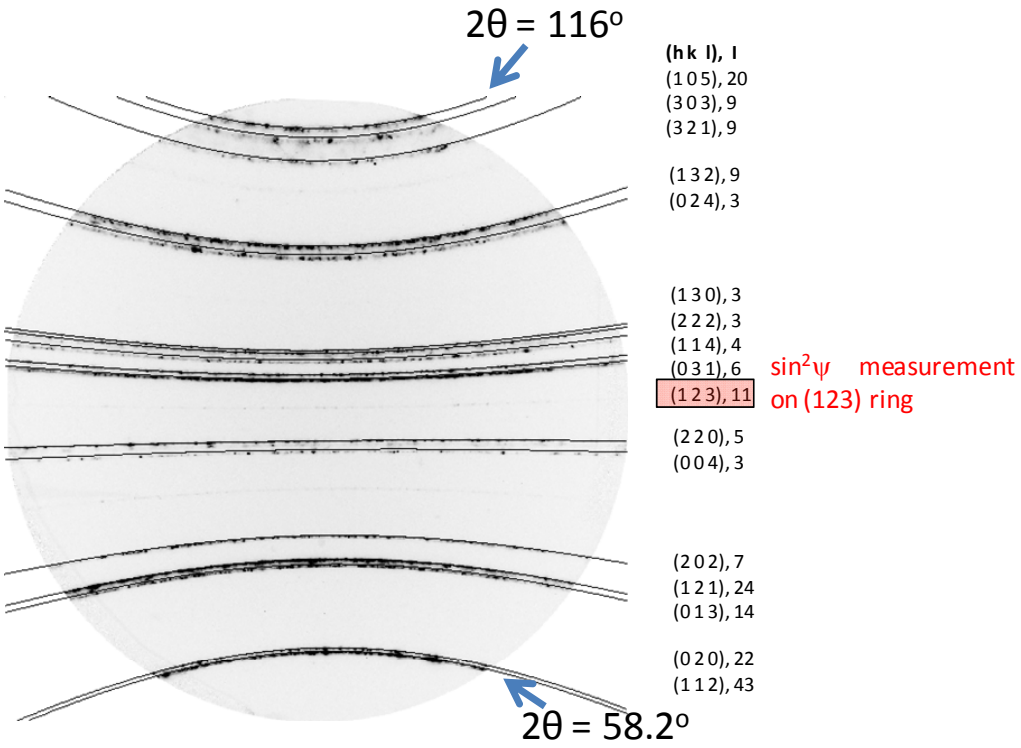

Figure 36 Monochromatic diffraction pattern from the zirconia core. A simulated ring pattern has been overlaid on top of the diffraction image. Also listed are the different diffracting planes the rings correspond to for a tetragonal zirconia crystal. The (123) has the widest ψ range and was utilized for the $\sin^2\psi$ method to evaluate stresses.

$Sin^2\psi$ method to measure the residual stress was conducted on a single diffraction ring corresponding to the (1 2 3) plane. The psi range of the (123) ring extends from $+27^o$ to -27^o. This particular ring was chosen since the ring had a maximum psi range and also comparatively higher intensity values. Figure 37a illustrates the range of psi of the (123) ring. The psi range was split into smaller integration segments of a 2^o psi range. Figure 37b indicates one such segment along with the integration profile along the 2θ direction. The integrated intensity peak was fit using a Lorentzian profile within an automated routine in XMAS. Figure 37c indicates the 3D perspective view of the integration segment along with a segment of the diffraction ring (123).

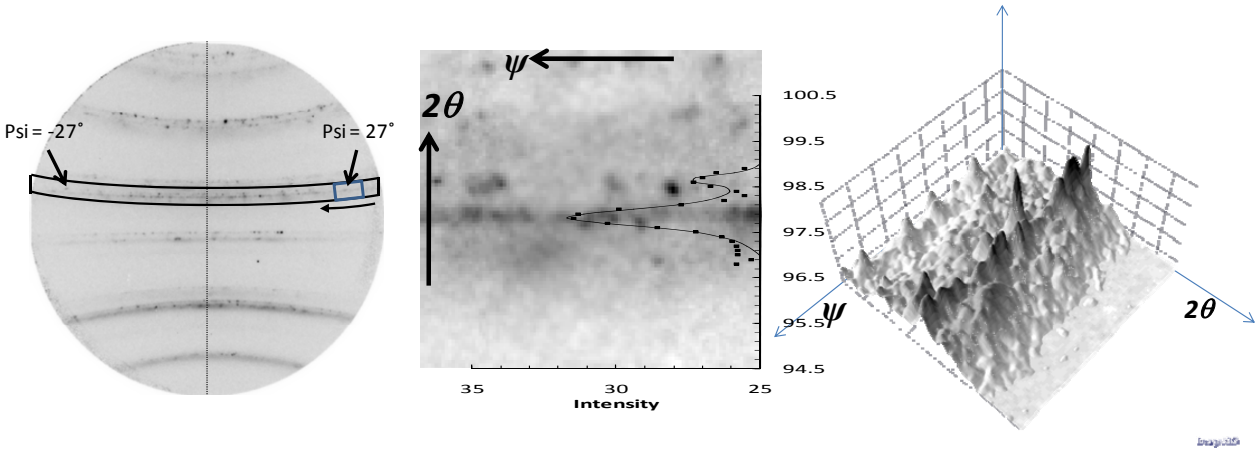

Figure 37 a. Raw diffraction image with the (123) ring highlighted and the total range of psi it incorporates. b. Integrated intensity profile for a 2^o segment of the (123) ring and the orientation of 2-theta and psi is indicated. c. Illustration of the angles in a 3D perspective indicates the signal-to-noise ratio at the given psi segment.

4.3.5 Data Collection and Analysis

Samples were mounted on the XYZ stage of the diffractometer on the kinematic bases. The preliminary step of adjusting the surface height with respect to the focal point was carried out. Based on the position of the beam spot on the sample, the extent of the raster line or

area scan was decided and the co-ordinates of the extents of the automated scan were entered into the CCD/Translation stage control software. The diffraction images were captured at a pre-defined exposure time after incremental translation of the sample.

The images collected were in the MAR CCD format, which can be opened directly into XMAS. The calibration file consisting of the information related to camera distance, tilts, energy and sample orientation was initialized. Following the calibration, the crystal files containing the lattice parameters and d-spacing's were initialized. Based on the crystal information, the rings can be simulated and overlaid onto the experimentally obtained diffraction rings to confirm the calibration parameters.

XMAS contains an automated routine which can evaluate the d-spacing based on the peak fit for every image in a line or area scan. The precursor to the automation is a peak fit template. To prepare an initial peak fit which acts as a template for the automation, an image taken far away from the interface was opened. Far from the interface, the sample was under comparatively lower residual stress and the diffraction rings were less distorted and had a better signal-to-noise ratio. The template provides an initial guess of the 2-theta value for the peak fitting program along with the tolerance and range of 2-theta where the peak profile had to be fit. Another critical input in the template was the angular range of psi for the integration segment. Once the template was created, the automated analysis could be performed on a particular dataset. The automated routine outputs the results in a delimited text format consisting of the 2-theta value based on the peak fit along with the peak width, integrated area under the peak and the corresponding d-spacing and image index. Each automated output file belongs to a specific psi segment. Starting with a peak fit template

creation, the procedure was repeated for multiple psi segments between the $+27^{o}$ to -27^{o} psi range.

In the current analysis the (1 2 3) ring was divided into 37 segments with a 2^{o} angular range. A customized VBA code as attached in Appendix A was developed to consolidate the results from the 37 automated analysis output files related to every psi segment. Further, the code evaluates the residual stress for every scan point based on the d-spacing at different psi locations using the $\sin^2\psi$ method. The program automatically consolidates the inputs from several files, evaluating the stress values and outputting the results in the form of a stress plot along a line or area scan. An example plot of the $\sin^2\psi$ versus the d spacing is shown in Figure 38. The slope of the line fit for the data is used to determine the slope. The intercept indicates the value of $d_{\psi=0}$. The value of residual stress is obtained by substituting the values of slope and intercept in Equation 9.

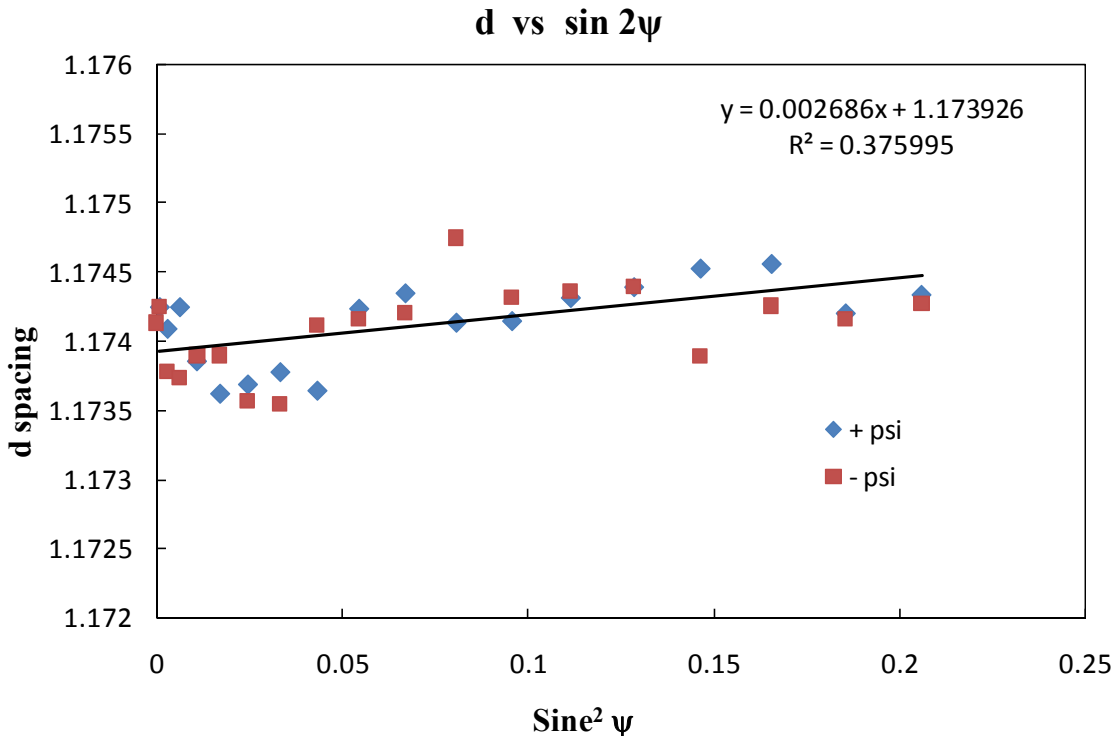

Figure 38 A typical d-spacing versus $\sin^2 \psi$ plot obtained at a scan point in the line scan. Error bars in terms of stress are derived by calculating the standard deviation along the fit. The intercept of the line fit indicates the $d_{\psi=0}$. The calculated slope of the fit is utilized in determining the biaxial stress value.

4.4 Results

The $\sin^2\psi$ method as explained in the previous sections was employed to obtain grain averaged residual stress. Monochromatic diffraction experiments were conducted on a zirconia core sample, a sectioned intact crown sample and a sectioned crown which had undergone fatigue fracture at one of the cusps due to cyclic fatigue of 45,000 cycles. All the results were obtained from the analysis of the diffraction images acquired at line or area scans on the crowns.

4.4.1 Zirconia core sample

A line scan consisting of 15 scan points was performed on one of the cusps of the core. The location of the line scan was decided based on minimal curvature of the core.

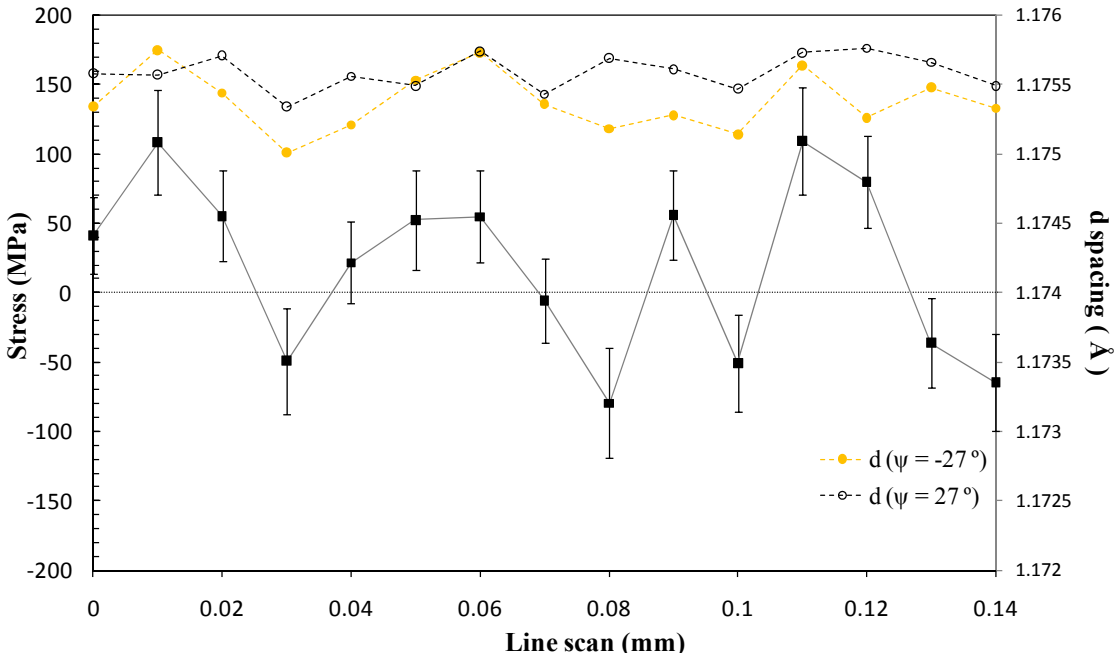

Figure 39 Biaxial stress measurements carried out on a zirconia core on one of the top cusps (indicated in the graphic). The line scan shows that the average type I residual stress observed on the core was close to zero. The line scan was recorded for 150 µm on the surface with a curvature effects < 3 µm. Curvature introduces significant displacement errors in the recorded values.

Figure 39 illustrates the residual stress plot for a 150 µm line scan. An average biaxial residual stress of 10 MPa was determined on the core. A ± 5 µm displacement of the sample surface away from the focal point of the beam was observed for a 0.75 mm line scan on the sample surface. Considering the elastic modulus of zirconia (E = 205 GPa), the 10 µm total sample displacement represents a normal stress of 15 MPa.

The error bars in stress were determined based on the error in the peak fit which corresponds to a 2-theta range that in turn corresponds to a range in d-spacing. The associated strains were determined and converted to stress values. The results obtained from the zirconia core sample serve as a reference and indicate close to zero residual stress on a zirconia core without veneer.

4.4.2 Sectioned Intact Crown with no fatigue

High resolution line scans were performed at two different locations on a sectioned intact crown. The scan points in the line scan were spaced 2 μm apart. Figure 40 presents results for the two line scans L_1 and L_2 as indicated in the picture set in the graph. L_1 was located towards the basal portion of the crown and L_2 was located around the top cusp, adjacent to the curved portion of the core.

The average biaxial residual stress was found to be 327 MPa and 350 MPa for lines L_1 and L_2 respectively. An important point to note, is shift in the stress profile towards compression in the 25 micrometer zone from the interface of the veneer and core. The evidence of such a trend was seen at both the line scans.

The corresponding values of d-spacing in case of L_2 were also plotted (as shown in Figure 41) to observe the behavior of lattice planes as a function of the distance from the interface. The plot exhibits a trend similar to the stress profiles and it was confirmed that there was occurrence of compression of the lattice planes in the vicinity of the interface. Finite element predictions were obtained from a model developed from the micro-tomography of the sample (described in detail in Chapter 5). Predictions from FE model indicate a compressive zone of approximately having a 225 MPa compressive stress on the porcelain side.

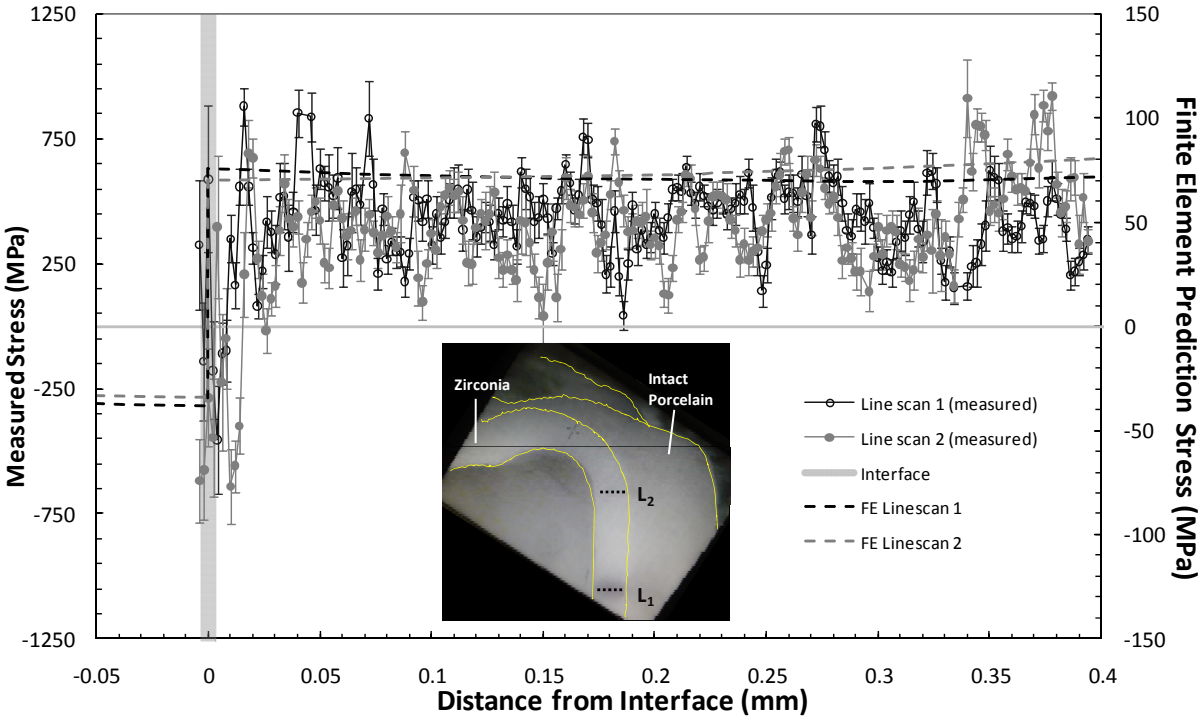

Figure 40 High resolution line scans L_1 & L_2 conducted on a sectioned intact crown. The line scans were located as shown in the micrograph. An average residual stress value of 325 MPa was observed for both the line scans. Variation in stresses (mostly between 100 – 400 MPa) can be seen along the line scan. At the interface the stress values obtained from the tetragonal phase seem to be compressive up to about 300 MPa in both the line scans. Results from finite element simulations of a real geometry of the crown are also overlaid as dotted lines corresponding to L_1 & L_2.

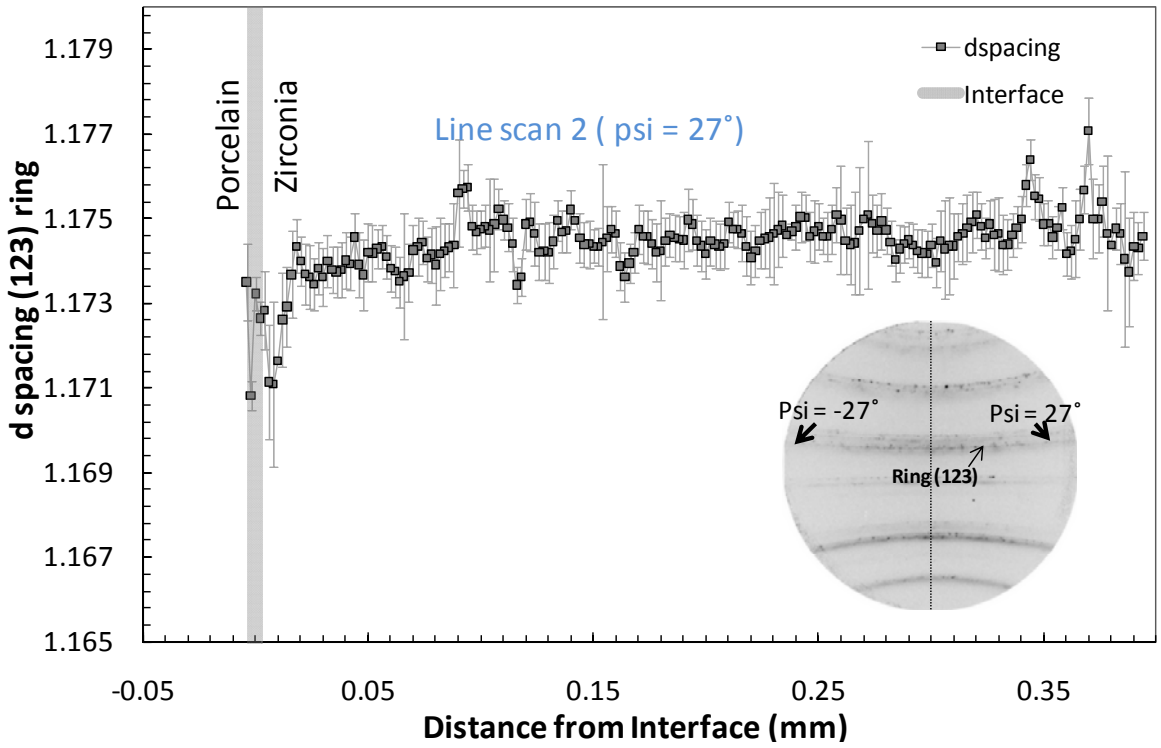

Figure 41 Illustration of the d-spacing variation at scan points along line scan L_2. The d-spacing of the (123) ring indicates compression at the interface.

Figure 42 indicates the diagonally sectioned FE prediction of the residual stresses in the zirconia core crown. Based on the features observed on the sample geometry, the FE model was virtually sectioned in accordance with the section aligned on the sample.

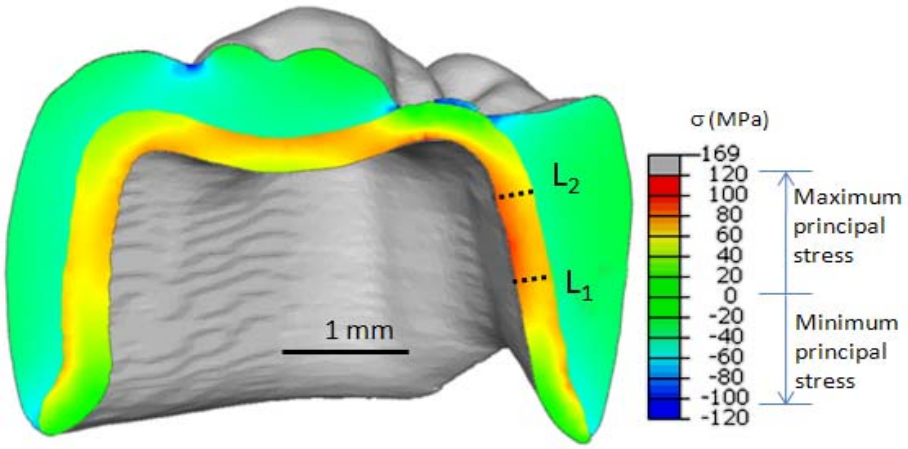

Figure 42 Finite element (FE) simulation of the thermal interfacial residual stresses. The section of the crown indicated in the FE model was created with a close comparison to the real sample section. Results show an presence of tensile residual stress on the core interior side of the zirconia core.

4.4.3 Sectioned Crown subjected to impact fatigue

The crown subjected to 45,000 fatigue cycles at a 150 N load had a failure on one of the cusps. Prior to sectioning the sample, a high resolution tomography was acquired at a 9µm/pixel pixel. Figure 43 indicates a sectional view and a 3D perspective view of the crown with the fractured cusp, respectively. The white exposed portion of the tomography indicates the underlying zirconia core after the veneer was chipped off. Figure 44, illustrates the line scan along which diffraction scans in the $\sin^2\psi$ orientation were obtained. The scans were performed on the flat surface of the wet-sectioned crown. The section was aligned diagonally coinciding with the fractured cusp.

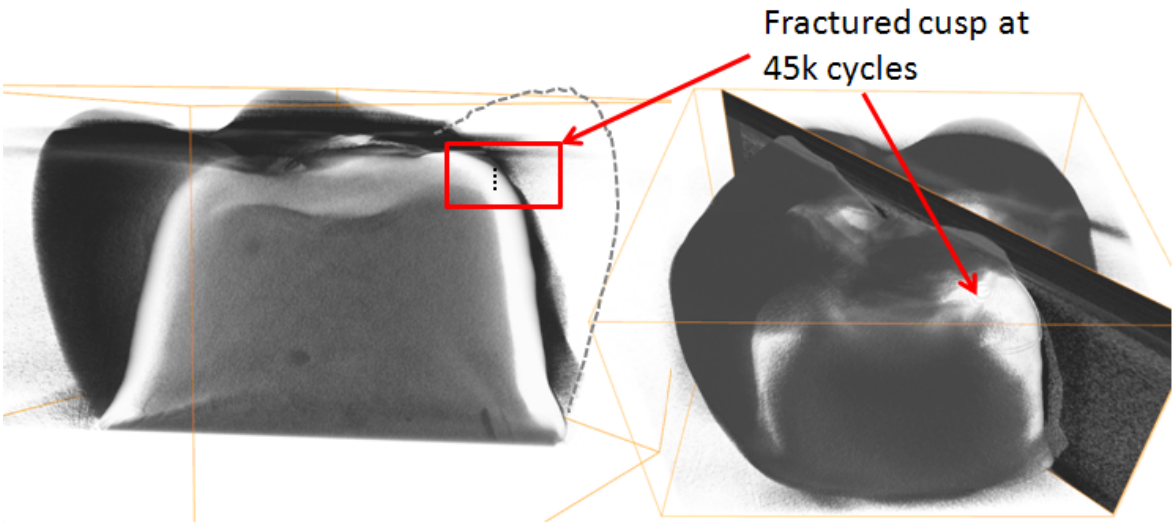

Figure 43 Micro-tomography reconstruction of the fractured zirconia core crown prior to wet-sectioning. (Left) tomographic sectional view showing the chipped veneer indicated by a dotted line. Red box indicates the region where the diffraction line scan was performed post fracture. (Right) 3D perspective view of the crown. Brighter region in the tomograph indicates the exposed zirconia core after fracture.

A 150 µm long line scan was recorded with 2 µm spacing between scan points, extending from the interface region to the inside surface of the core as indicated in the in-set in Figure 44.

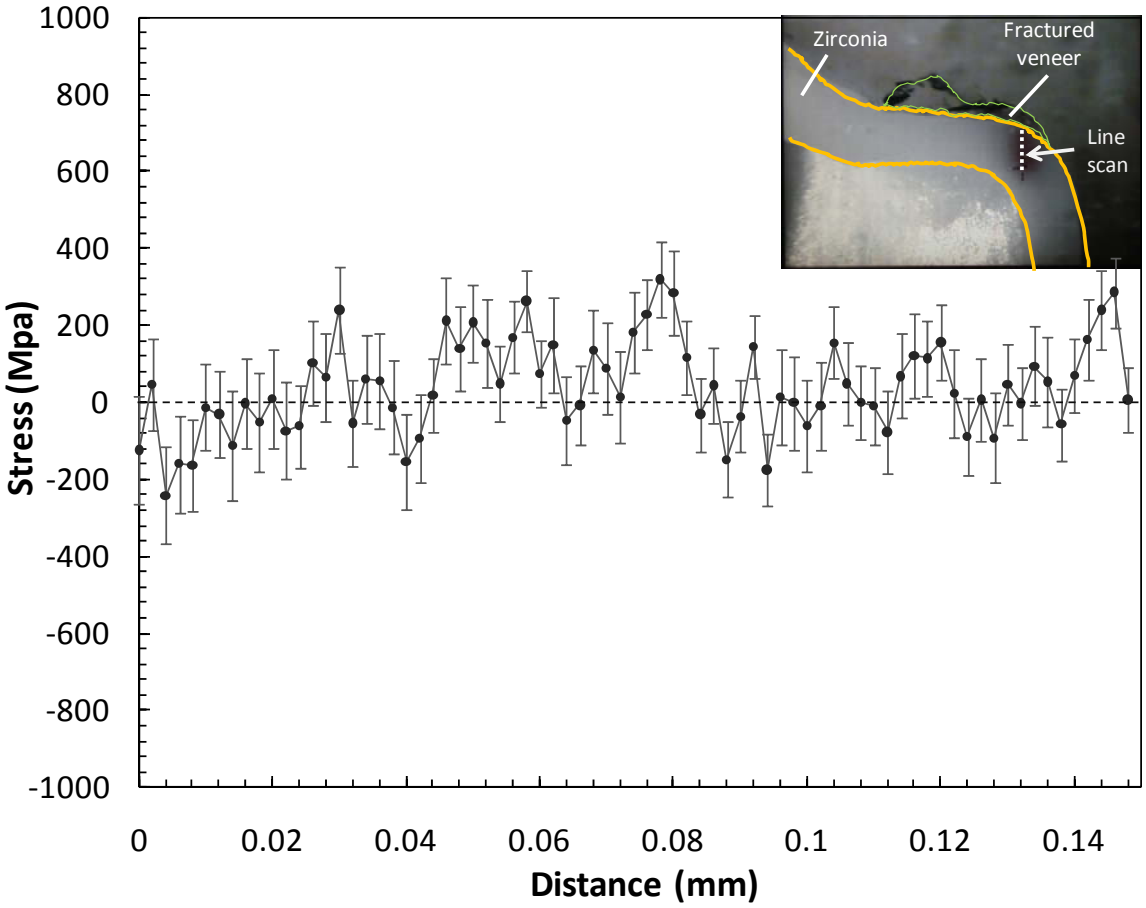

Figure 44 Residual stress information from a diffraction line scan performed on the sectioned zirconia core and normal to the fractured surface. Fracture of the veneer cusp occurred after 45,000 fatigue cycles.

The $\sin^2\psi$ evaluation of the diffraction images along the line scan resulted in an average residual stress value of 22 MPa with a variation between +350 MPa and -350 MPa in the measured stress values.

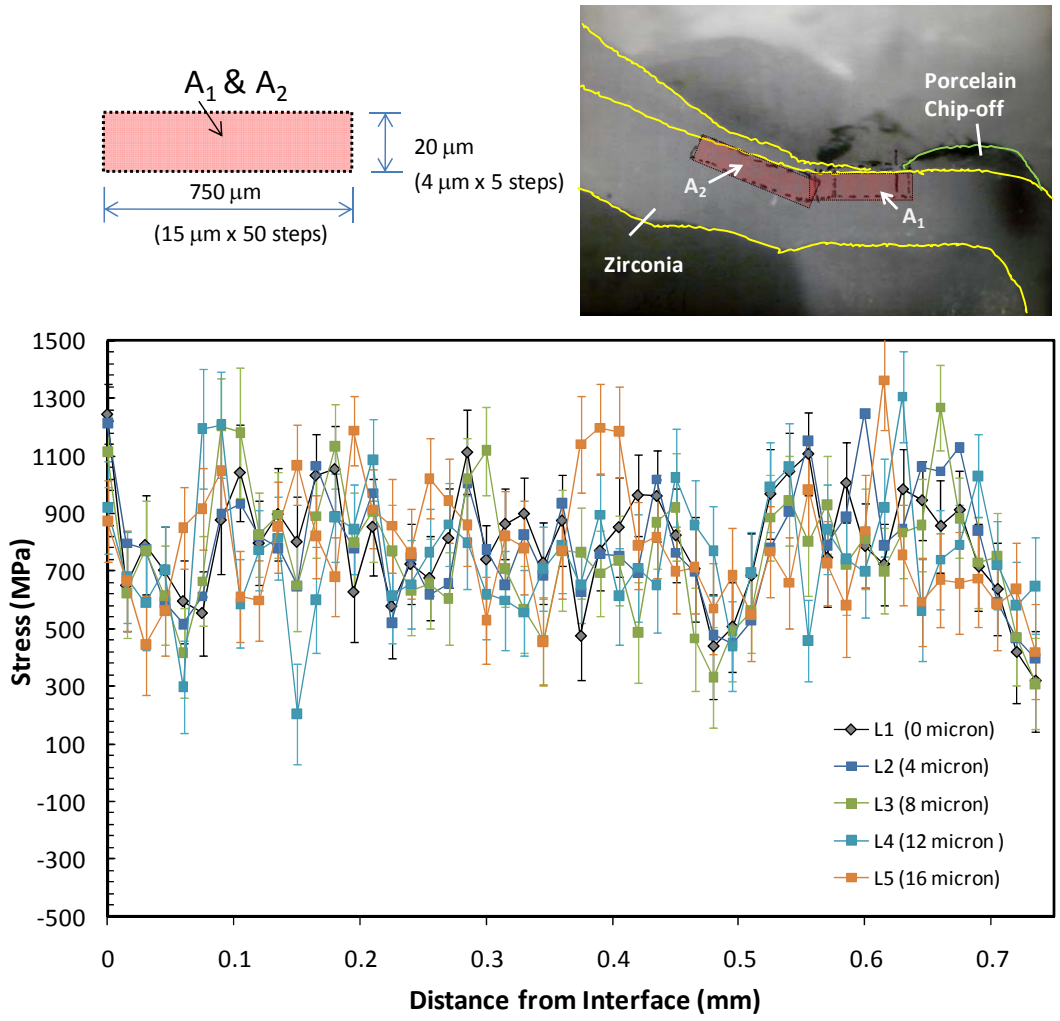

Figure 45 High resolution area scan consisting of 5 line scans in the neighborhood of the free exposed surface after fracture of the veneer cusp. L_1-L_5 correspond to the line scans taken at 4 micron incremental steps from the interface.

The area close to the interface was consistently observed to have large variations in stress values, generally compressive in nature. In order to further investigate the stress state in greater detail, high resolution area maps were rastered along the edge of the sample as indicated in Figure 45. The edges were exposed regions of zirconia after the fatigue fracture of the veneer cusp. The area scan was made up of 5 high resolution line scans spaced 4 microns apart and each one is plotted in Figure 45. Wide distributions of tensile stresses,

ranging from 200 MPa to 1300 MPa were encountered for the small area of 20µm x 750µm at the interface.

4.4.4 Qualitative analysis of X-ray data from intact crown

A qualitative study of the diffraction patterns collected along the line scan was conducted. The ring positions and the ring widths were examined as the interface was approached. Figure 46 shows diffraction images corresponding to positions – far (1), central (2) and at the interface (3) on the sectioned intact crown sample. Arrows indicate three rings which show a evidence of severe lattice distortion approaching the interface.

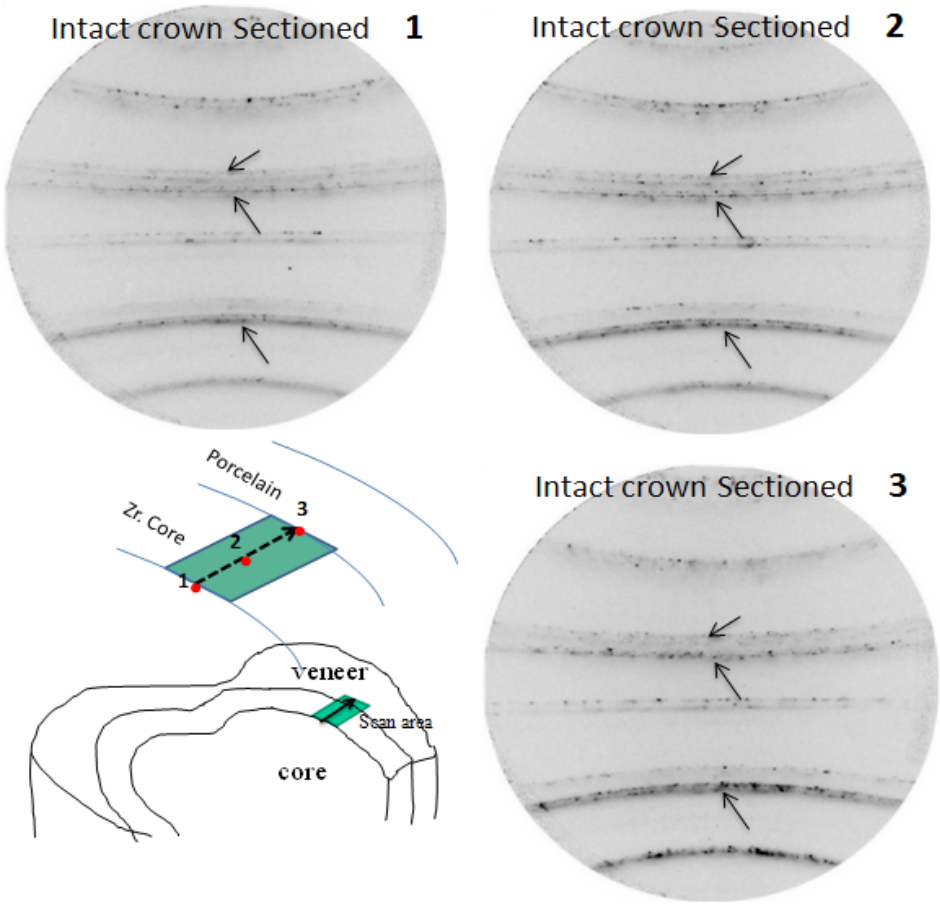

Figure 46 Ring gets brighter and wider towards the interface. As seen in table for Monoclinic ZrO_2 the (-3 0 2), (202), and the (013) rings overlap the tetragonal rings.

At (1) the grains are far away from the immediate zone of the interfacial residual stresses. Distinct rings corresponding to the tetragonal lattice planes were seen. At the central portion of the cross section (2) there was no significant change observed in the rings. However (3) indicates broader and brighter rings as expected at the interface due to the high amount of localized residual stress. The stress and strains for the line scan including location 1-3 are shown in Figure 47.

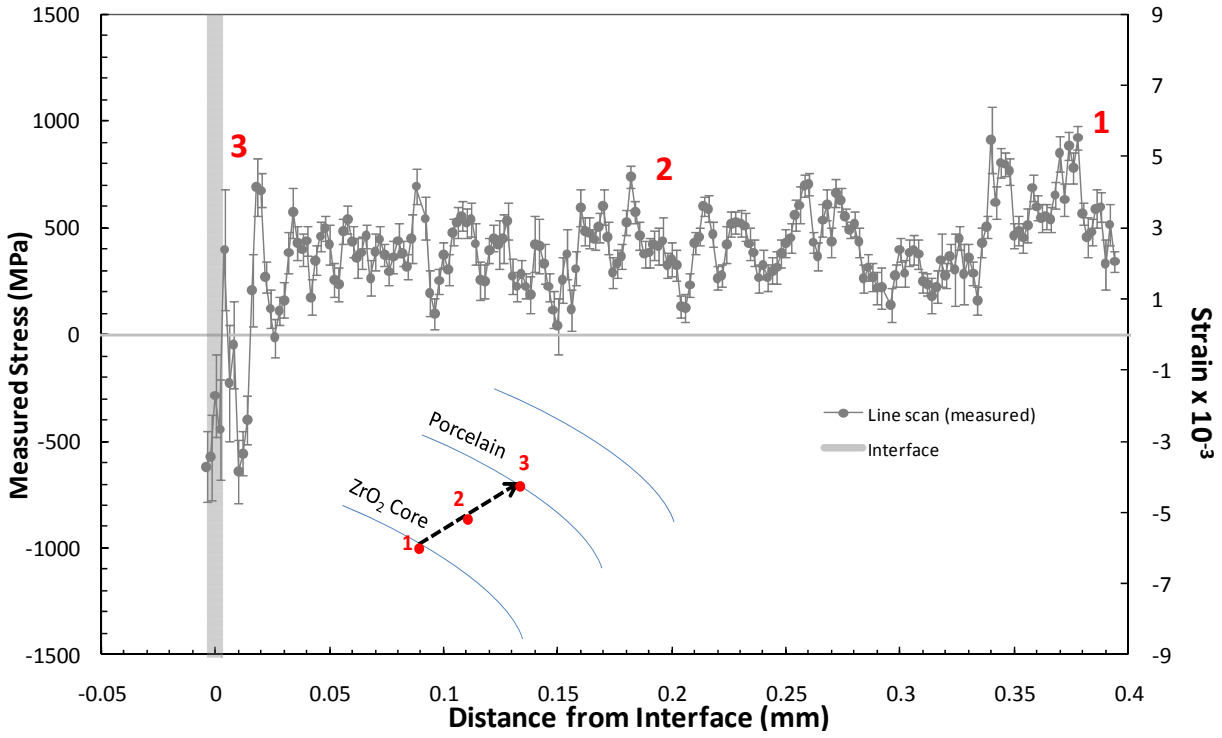

Figure 47 Stress and strain values along a line scan including points 1, 2 & 3 which coincide with the far, mid and close to interface positions on the intact sectioned crown.

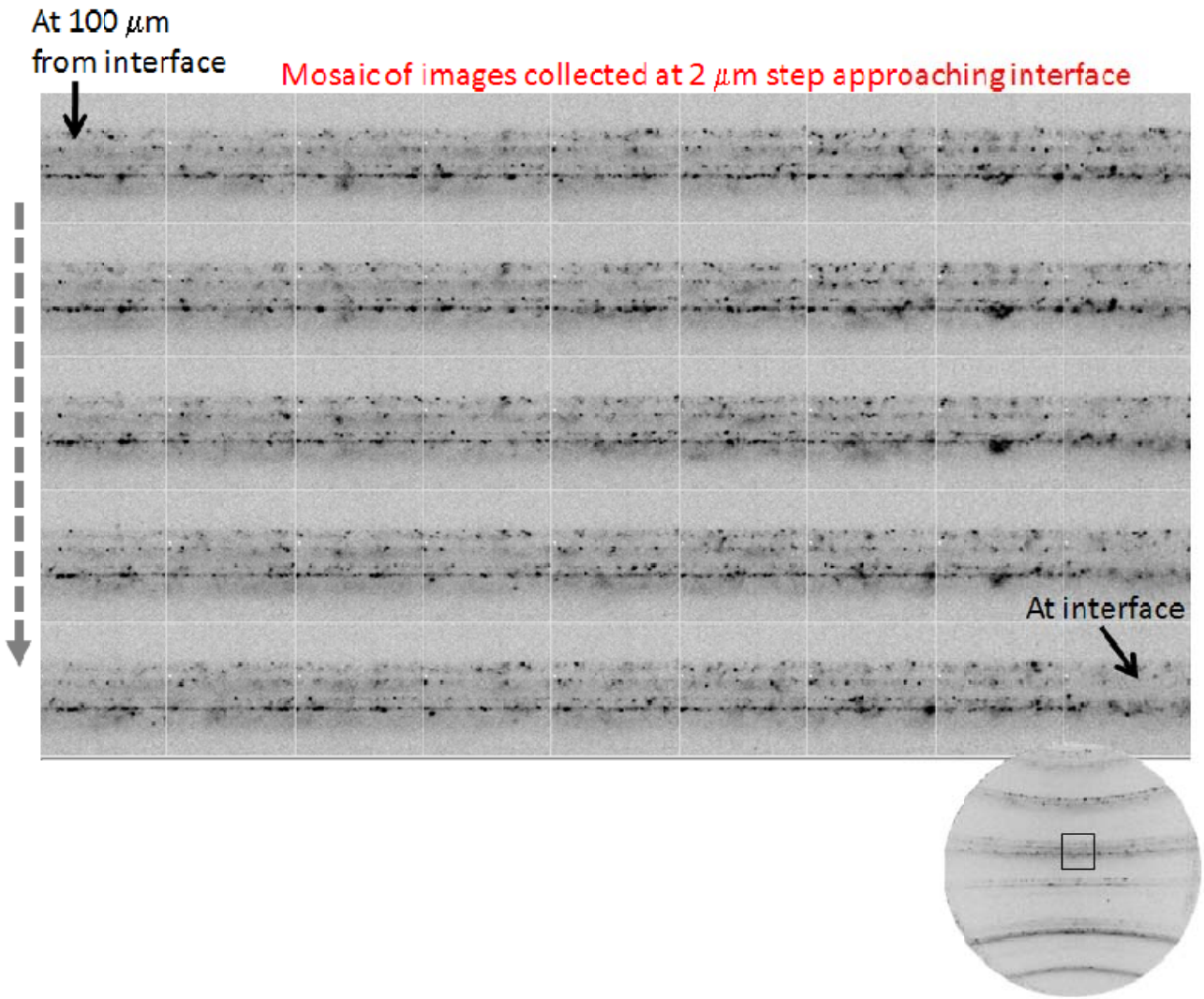

Figure 48 Mosaic pattern of the ψ = 0 segment for the (013) ring. The mosaic represents the rings obtained at 2 μm positions along the line scan starting from 100μm away from the interface. The last few images correspond to the interface where the stress gradients were severe and caused distortion in the rings

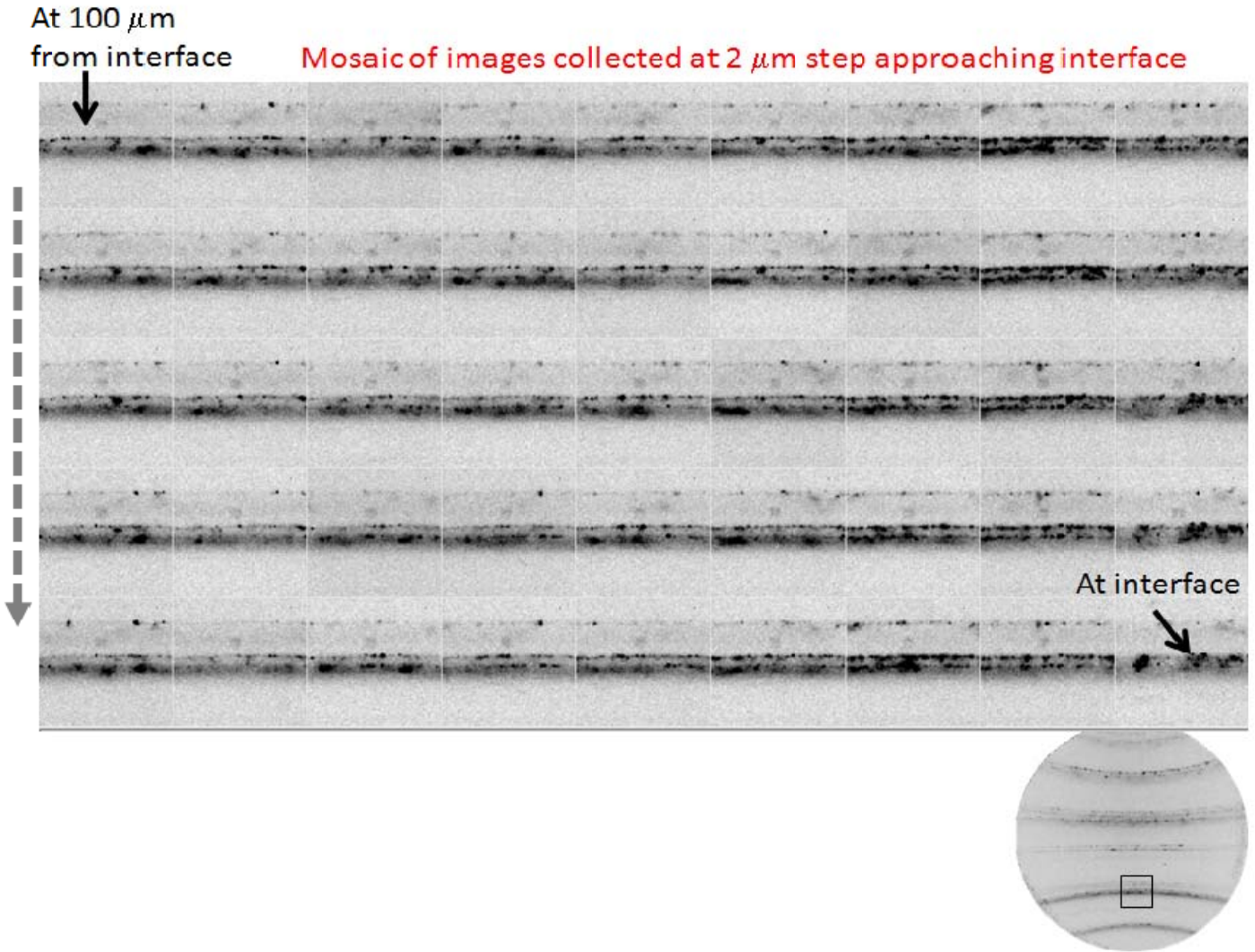

Figure 49 Mosaic of the (123) ring obtained from the same line scan as that used in the previous mosaic pattern. The diffraction rings in the last five images are broadened indicating the distortion of lattices near the interface.

Considering one of the exposure from a line scan at the interface of porcelain and zirconia, a grain contributing to the (123) diffraction cone was examined. The grain with largest deviation from the reference d-value was chosen to estimate the highest stress observed. For the grain observed in the inset in Figure 50, the measured strain based on the 2θ value was 3.658×10^{-3}, which corresponds to a stress of 750 MPa.

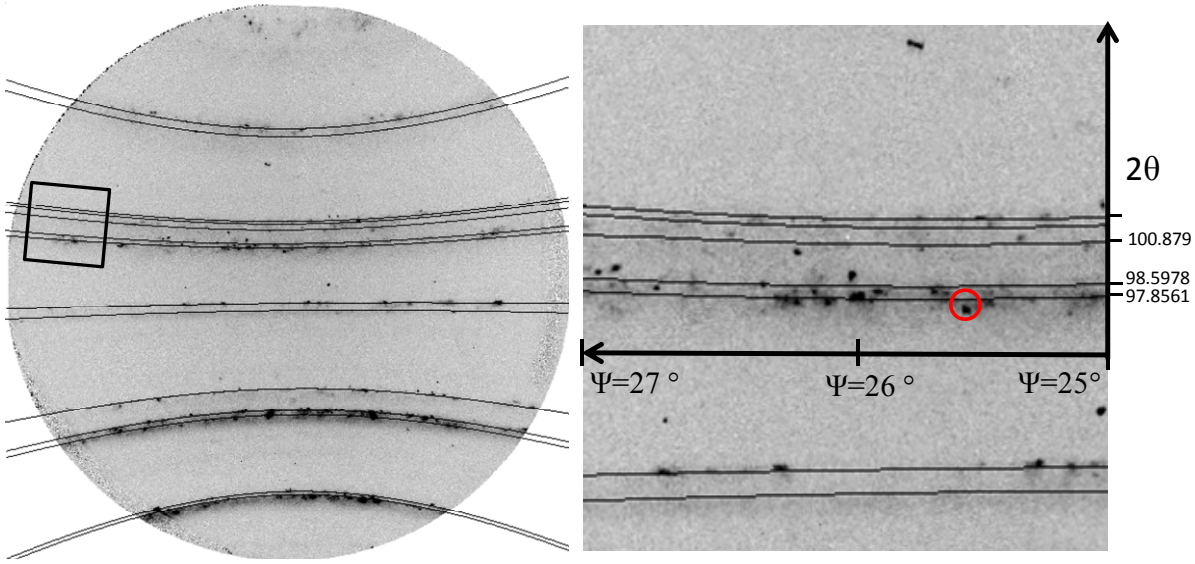

Figure 50 Illustration of the contribution of several grains to the (123) ring. Among many grains, the inset indicates a grain (circled red) with a large strain (3×10^{-3}) at ψ=25.5°.

4.5 Discussion

From the analyzed residual stress from acquired from the intact crown, zirconia core, and the crown subjected to impact fatigue; it appears that the residual stress changes in accordance to the change in the conditions of the sample. A marked difference was observed in the values of the intact and fatigued crown. Residual stress measurements using the $\sin^2\psi$ method were performed only on the zirconia core. Porcelain being amorphous, no diffraction rings could be acquired. A separate experimental technique would be required to assess the magnitude of residual stresses in porcelain. Figure 36 indicates the residual stress in the monolithic

zirconia core was close to zero. Use of a large beam compared to the zirconia grains, leads to a grain averaged residual stress value. Polychromatic micro-beam measurements of inter-granular stresses indicate significantly high values as concluded in Chapter 3.

The process of firing the porcelain veneer on the zirconia core introduced interfacial residual stresses which is evident from Figure 40 - Figure 42. The addition of the veneer layer puts the entire zirconia core in an average tensile stress state of 250 MPa as seen in Figure 40. The sectioned samples were observed under an SEM which reveals rough bands resulting from the wet sectioning on a diamond saw (Shown in Figure 51). Further surface preparations were avoided in order to preserve the residual stress state. The striations from the sectioning can possibly lead to the significantly large errors bars that were observed in the calculated stress values (As shown in Figure 40). Although the process of sectioning the sample would reduce or eliminate the existing out of plane stress, the $\sin^2\psi$ measurement successfully measures the biaxial in-plane stress.

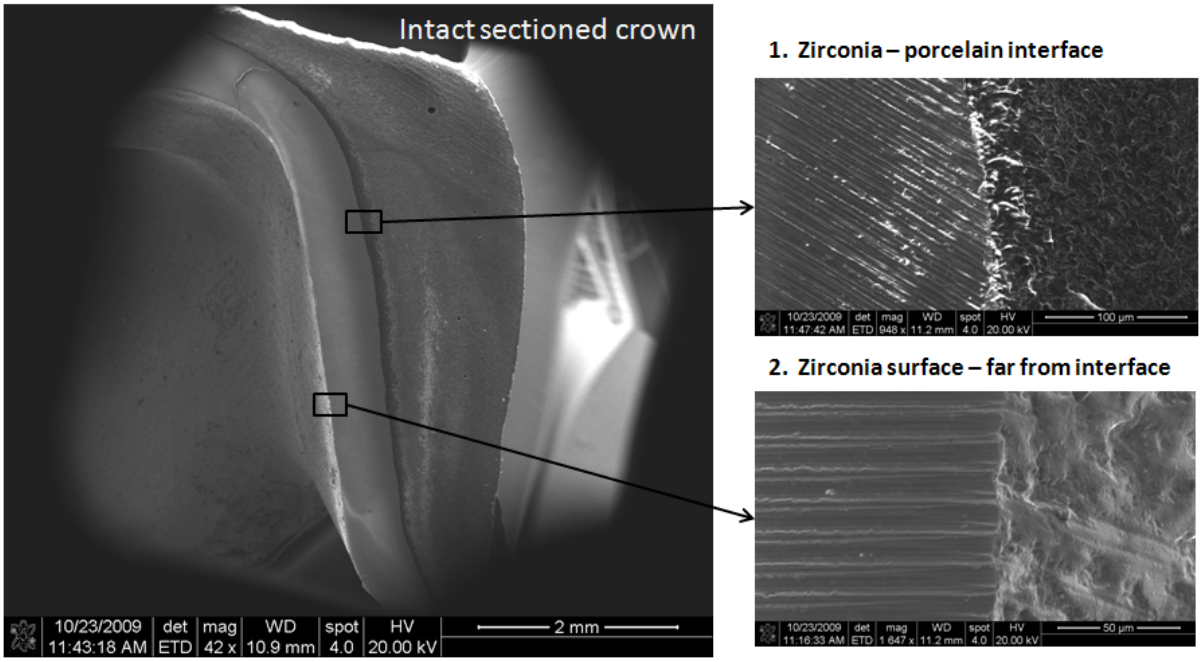

Figure 51 SEM micrographs of interface(1) and wet-cut core surface (2). SEM showed a good bonding between porcelain and zirconia. (2) shows the uneven striations on the surface of zirconia caused in the process of cutting with a diamond saw. No further polishing was done to avoid further contamination of residual stresses.

An interesting point to note in the line scans, is the downward trend of the curve in the direction of compression near the interface. At the interface where the residual stresses are high, zirconia experiencing highest tensile stresses and porcelain under highest compressive stress, the tetragonal crystals of zirconia undergo a stress induced phase transformation. This transformation results in a monoclinic phase of zirconia with larger volume compared to the tetragonal crystal. Neighboring tetragonal zirconia crystals in the vicinity of the monoclinic transformed crystals are now subjected to a compressive stress due to the confinement within the bulk.

A spotty wide inconsistent ring is indicative of the presence of excessive elastic deformation in some grains. Furthermore if the ring is broad throughout along psi, the condition may be

indicative of overlapping secondary crystalline phase occurring due to transformations. Evidence of the monoclinic phases of zirconia close to the interface (20 μm from the interface) was investigated by careful examination of individual rings in a mosaic pattern along the line scan (as shown in Figure 48 &Figure 49). The mosaic of the inset depicts the rings corresponding to the (0 1 3) and (2 0 2) planes of the tetragonal phase of zirconia. As the interface is approached, these initial distinct appearing rings far from interface appear to broaden and merge into each other. A typical intensity versus the 2θ (Figure 52) indicates the emergence of a (-3 0 2) monoclinic peak in between the two tetragonal peaks seen in the inset image. Furthermore, similar occurrence of five different low intensity peaks is seen overlapping the tetragonal peaks between the 2θ range of 96^{o} to 99^{o} (also seen in the inset mosaic in Figure 49). Although it can be inferred from the intensity-2θ plot, that the fraction of monoclinic phase observed is small, the effect on the measured d-spacing of tetragonal phase is very pronounced. Similar evidence can be observed from the simulated ring patterns overlaid on the diffraction image (as shown in Figure 53). The rings with overlapping monoclinic peaks appear broad and hazy.

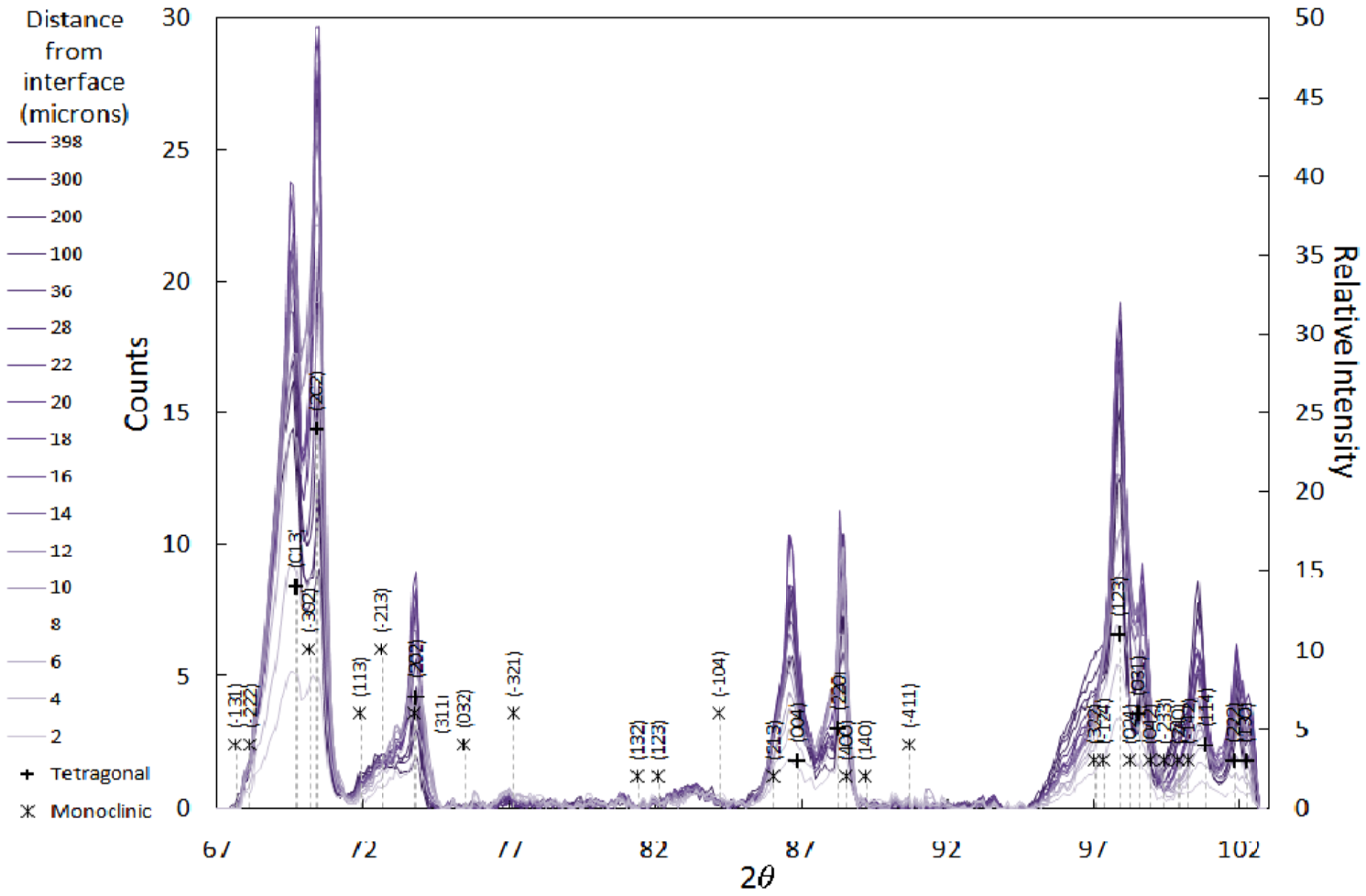

Figure 52 Consolidated Intensity Vs 2θ plot from several diffraction scan points along a line scan approaching the interface of zirconia and porcelain. The powder diffraction data for tetragonal and monoclinic phase of zirconia is overlaid. Faint lines indicate close to interface scans.

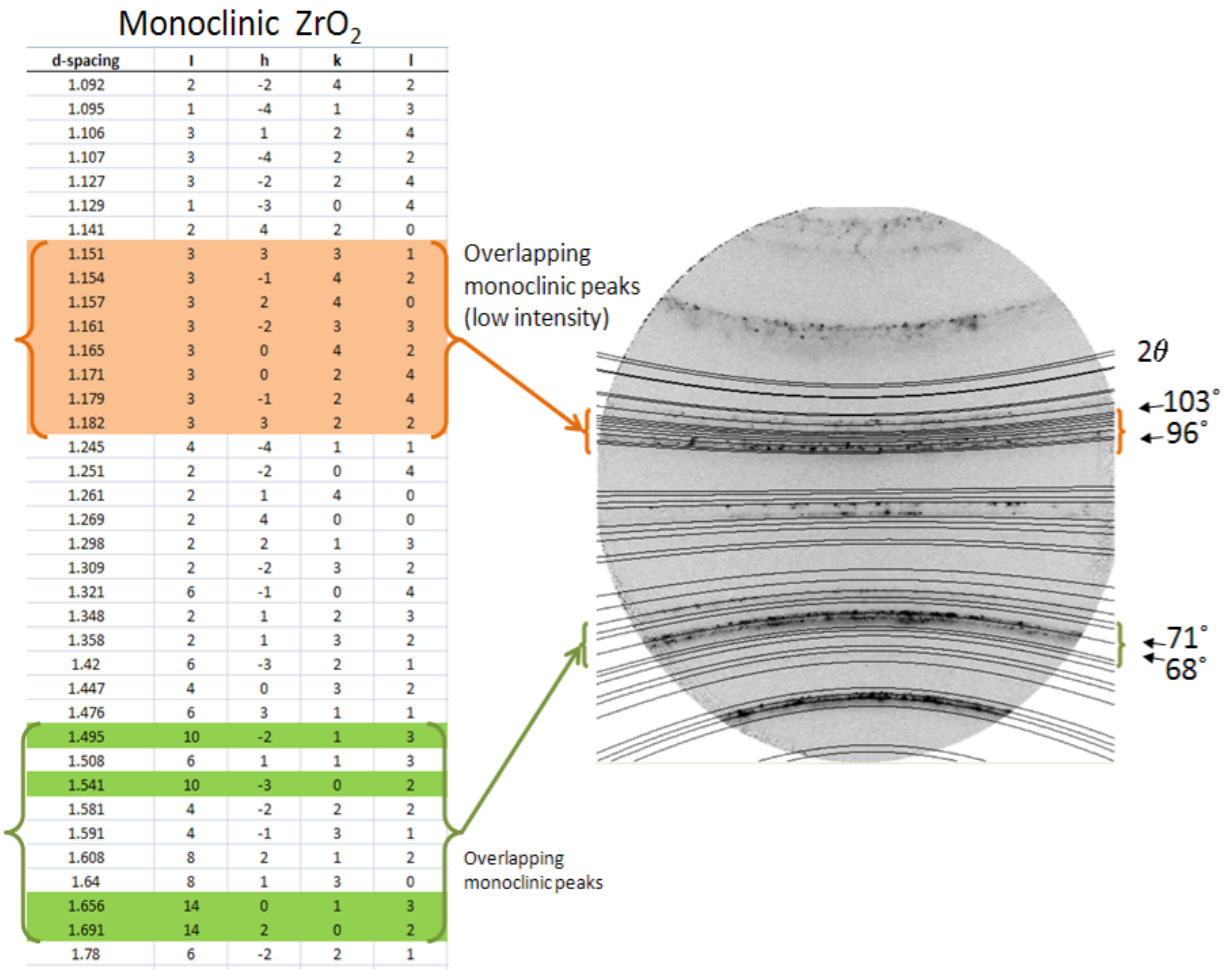

Figure 53 The rings gets brighter towards the interface. As seen in table for Monoclinic ZrO_2 the (-3 0 2) and (202), (013) rings overlaps the tetragonal peaks. This probably leads to the increase in intensity.

The veneer cusp fractured and chipped off from the zirconia core at 45,000 impact fatigue cycles. Although the zirconia is in tension, failures initiate in the veneer region. After fracture, the residual stress equilibrium is changed and a relaxation in the residual stress at the fractured zone is expected. Fracture occurs at the expense of the energy dissipation in propagating the crack. The results of the line scan on sectioned surface underlying the fractured cusp as seen in Figure 45 indicates evidence of this hypothesis. The overall stress

underneath the fracture is comparable with that of the monolithic zirconia core observed earlier.

However, further examination of the nearby vicinity of the fractured veneer interface with high resolution area maps revealed interesting results which were not anticipated earlier. A significantly higher range of tensile stresses (greater than 300 MPa) were observed within 20 μm of the fractured veneer interface. The error bars associated with the data points were larger due to severe distortion of the rings and lower intensity at higher ψ angles. The observation of these high tensile residual stresses can be rationalized through some detailed analysis in terms of the crystallography and the macroscopic stress state as illustrated in the schematic (Figure 54).

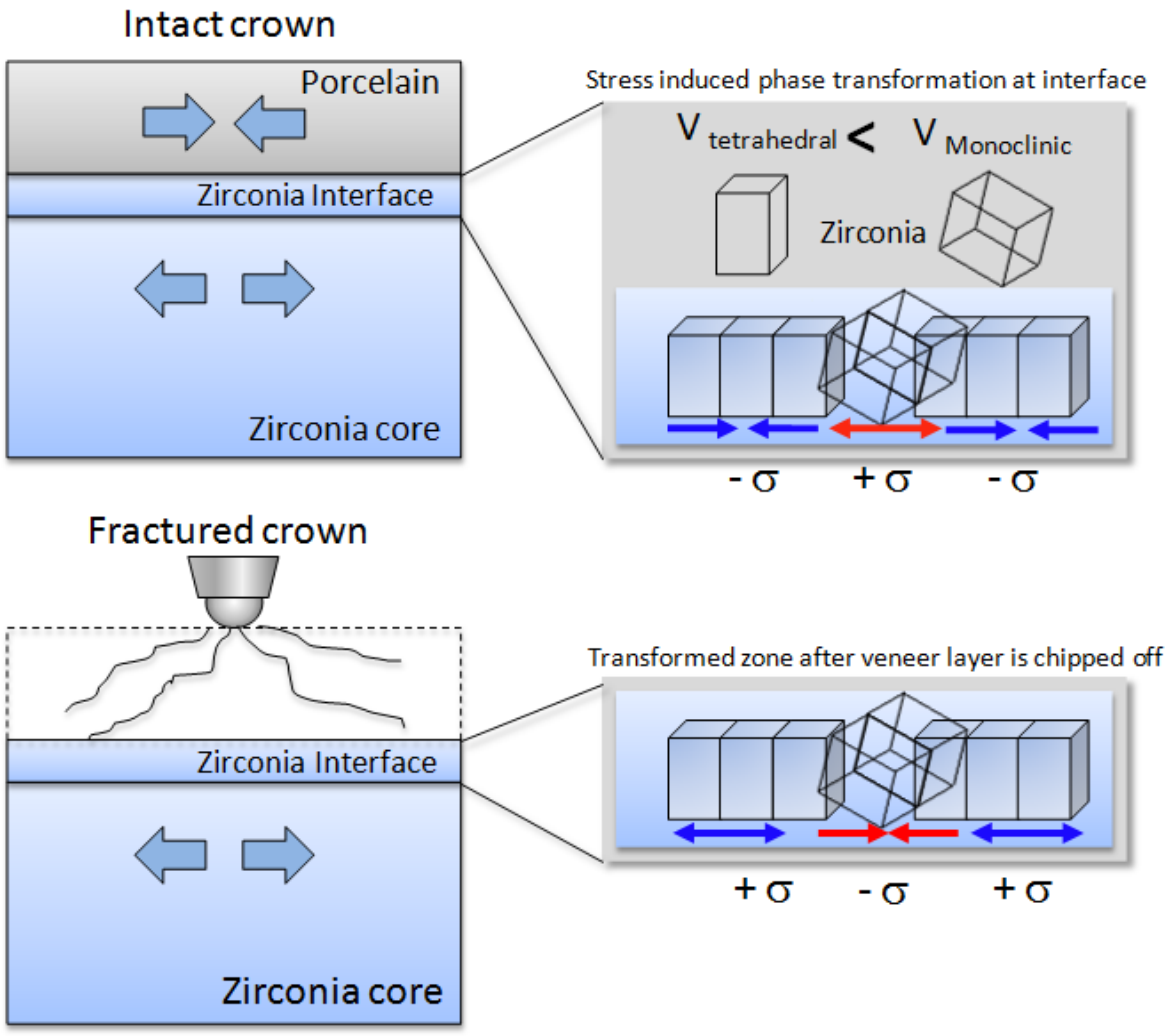

Figure 54 (top) Illustration of the rationale of the observation of compressive stresses in zirconia at the interface layer due to stress induced phase transformations. (Bottom) Schematic of the mechanism of stress relaxation after fracture followed by the tensile stresses in zirconia at the interface.

Figure 54 indicates the state of the interface region of zirconia in an intact crown. Due to the mismatch in coefficient of thermal expansion of the porcelain and zirconia, the core is in a net tensile residual stress and porcelain in a net compressive residual stress. At the interface, the tetragonal crystals under high stress, undergo stress induced phase transformation to form the monoclinic phase of zirconia. Transformation from the tetragonal to monoclinic phase results in a volume expansion locally. As shown in the schematic, this local volume

expansion induces compressive stresses on the neighboring tetragonal zirconia crystals (indicated by blue arrows). This effect is manifested in the compressive trend seen earlier in line scans at the interface. The situation where the crown fractures at the interface leaving behind an exposed core surface is illustrated in Figure 54 (bottom). Upon cracking, the residual stress at the interface is relieved. The monoclinic phase which earlier was in tension, would tend to relax to its original state, and compels the tetragonal crystals to be in tension (shown in blue arrows). Results from the high resolution area maps at the fractured interface were in agreement with this hypothesis.

Predictions of the residual stress from finite element modeling as shown in Figure 42, were nearly 50% lesser than those observed from experimental results. Although, a geometric replica of the crown was used to conduct the simulation, results vary significantly. Simulation results were obtained with a continuum based approach, wherein the contribution of inter-granular stresses and grain-to-grain anisotropy cannot be modeled. Moreover, effects on the localized scale such as the stress induced phase transformation which is prominent in the vicinity of the interface are difficult to incorporate. A better modeling approach incorporating all the contributing factors to the net residual stress would provide with an accurate estimate through simulation.

4.6 Conclusions

A methodology of measuring grain averaged biaxial residual stress at a high resolution and with improved time efficiency using synchrotron X-rays has been developed. Residual stresses were determined without the need of tilting the sample and without multiple exposures at a given location. The technique has an added advantage of sampling the same grains that were analyzed with a polychromatic micro-beam without additional changes to the setup. High resolution line and area scans incorporating large numbers of data-points were performed. An automated data analysis routine has been developed to compute biaxial residual stress values from 2D image data.

Results from the experiments indicate the presence of an average tensile residual stress of 325 MPa in the zirconia core. At the interface of intact crowns, the tetragonal zirconia crystals experience compressive stress of about 550 MPa exerted by the phase transformed monoclinic zirconia crystals. Residual stresses observed in crowns with fracture due to fatigue cycling were close to zero. After a catastrophic failure of the veneer, the zirconia core which was earlier in a state of tensile residual stress is relieved of the tensile residual stress. However, within 20 μm of the exposed interface layer due to fracture, the tetragonal crystals of zirconia exhibited an average tensile stress of 600 MPa. After fatigue fracture the monolithic zirconia tends to retain an equilibrium state by relaxing to its original state and inducing a net tensile stress on the tetragonal phase of zirconia.

CHAPTER V

5 SIMULATION OF RESIDUAL STRESS IN A CROWN GEOMETRY

5.1 Introduction

Failures usually occur abruptly and catastrophically, in the form of veneer chip-off or failure of the crown with complete rupture of the core.[59, 61] An experimental evaluation of the performance of the dental restorations before clinical use is hence extremely critical. Reasonable statistics are achieved through mechanical testing of large number of samples leading to increased time and costs.[6] Simulation of mechanical testing conditions can be used to obtain the results efficiently. Simulation codes have been used over a couple of decades to evaluate mechanical properties such as stress distributions in restoration models.[62-65] Simulation approaches involved applying mechanical loads and boundary conditions on simplified models 2D/3D resembling dental geometries created using CAD. Significant developments were made in refining input models that closely represent the dental restoration through the use of advanced CAD software and input methods such as coordinate mapping of the manufactured part [59, 66-68]. Initial efforts on utilizing X-ray tomography to reproduce the real spatial geometries have been carried out. Efficient methods

of generating 3D geometries have been developed through the use of tomographic image segmentation.[69-71] These methods have allowed incorporating features such as voids, pores and other geometric features which are on the order of a few microns.

A typical dental crown has a complex geometry and an interface between the porcelain and zirconia which is a complex contour. Since residual stresses, influence the service life of a crown, it is important to study the nature and characteristics of the stresses when complex structures like the crown are considered. The task of experimentally determining stresses from an intact sample is difficult. The focus of the current study is application of micro-tomography to analyze the evolution and distribution of thermal residual stresses in dental restorations. Thermal residual stresses develop at the interface of the veneer and core of all-ceramic dental systems due to the mismatch in coefficient of thermal expansion (CTE).[68, 72] Analysis of the dental crowns is difficult due to the complex distribution of stresses and the curved geometry of crowns inclusive of the intrinsic microscopic features. Experimental analysis has shown that curvature can have a critical impact on the analysis of stress distributions.[73-74] Thermal residual stress distributions evaluated through finite element simulation of two different dental crowns with alumina and zirconia cores are presented.

5.2 Micro-Computed Tomography

An alumina core dental crown with a geometry identical to the zirconia core based crown was utilized for micro-Computed Tomography (μ-CT). The SkyScan 1172 μ-CT (Skyscan, Kontich, Belgium, http://www.skyscan.be) setup was used to conduct tomography of the samples. Within the average operable energy range of the μ-CT setup, zirconia has a higher linear X-ray absorption coefficient ($\mu_{l(Zr)}$ = 905 cm^{-1} for Cu Kα X-rays) compared to alumina ($\mu_{l(Al)}$ = 133.9 cm^{-1} for Cu Kα X-rays), which significantly affects the successive 3D

reconstruction. An example of the reconstruction slices from alumina and zirconia crowns is shown in Figure 55.

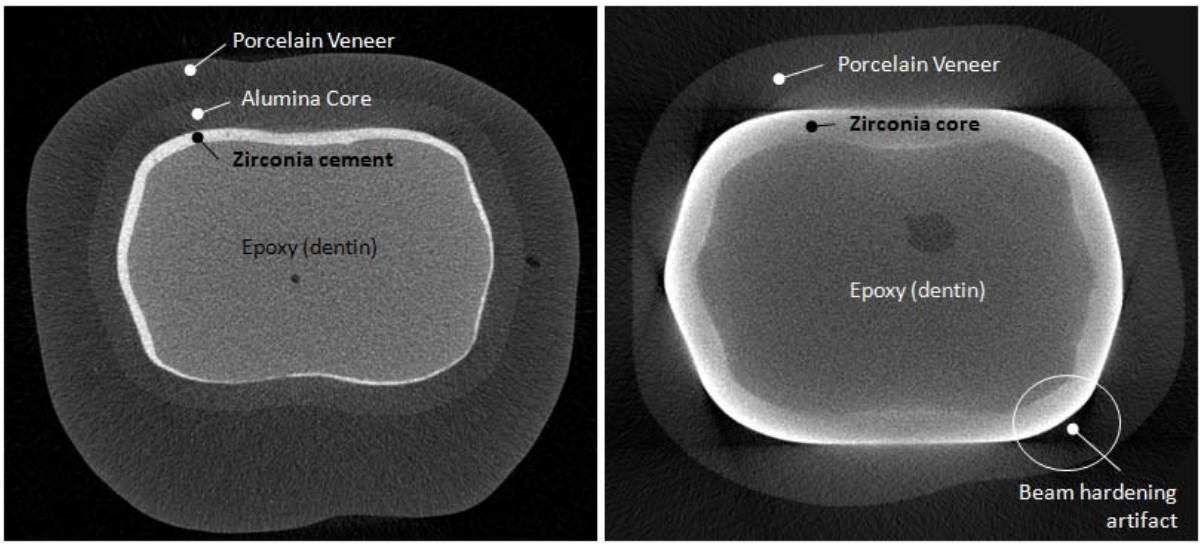

Figure 55. 2D tomograph sections of crown with a) alumina core (left) b) zirconia core (right). Circled area indicates beam hardening effect due to zirconia core

The experiment was setup such that the voltage was 100keV at a max power of 10W. The μ-CT setup has a fan X-ray beam configuration. 450 radiographs were acquired at 0.4 degree steps at and a spatial resolution of 9.08 μm/pixel and an exposure time of 1.475 s with the use of an 0.5 mm aluminum filter. Every frame was acquired through frame averaging of 8 exposures. A three dimensional reconstruction was carried out using NRecon (SkyScan, Belgium) based on the 524 radiographs which consists of a stack of thousand 2D slices in 16-bit TIFF format.

5.3 Image Segmentation

Three dimensional data analysis and visualization was carried out in Amira 3.1.1. The 3D reconstructed dataset had a spatial resolution of 9.08 μm/pixel and required 8 Gb of memory

allocation. The dataset was isotropically re-sampled using a 2 x 2 x 2 Lanczos filter leading to a resolution of 18.4 μm/pixel, in an 8-bit grayscale format. The decision of re-sampling was based on the critical feature sizes and was limited by the maximum memory allocation. Analysis of the dataset pertaining to evaluating micro-structural properties or visual analysis of internal features like cracks and pores can be carried out without a re-sampling. However, the process of image segmentation, surface reconstruction and volumetric mesh generation requires almost three times the memory allocated for the original dataset. Distinct ranges of gray scale values were observed to be associated with different regions of the crown. Lower gray scale values indicate less X-ray absorption and vice-versa due to the different X-ray absorption coefficients associated. As seen from Figure 56, both the porcelain and alumina regions were associated with an X-ray attenuation range of 10 % to 35 %. The zirconia adhesive corresponded to an attenuation range of 80 % to 90 %, due to its high absorption coefficient. The underlying epoxy layer exhibits higher grayscale values due to the low transmission past the zirconia layer.

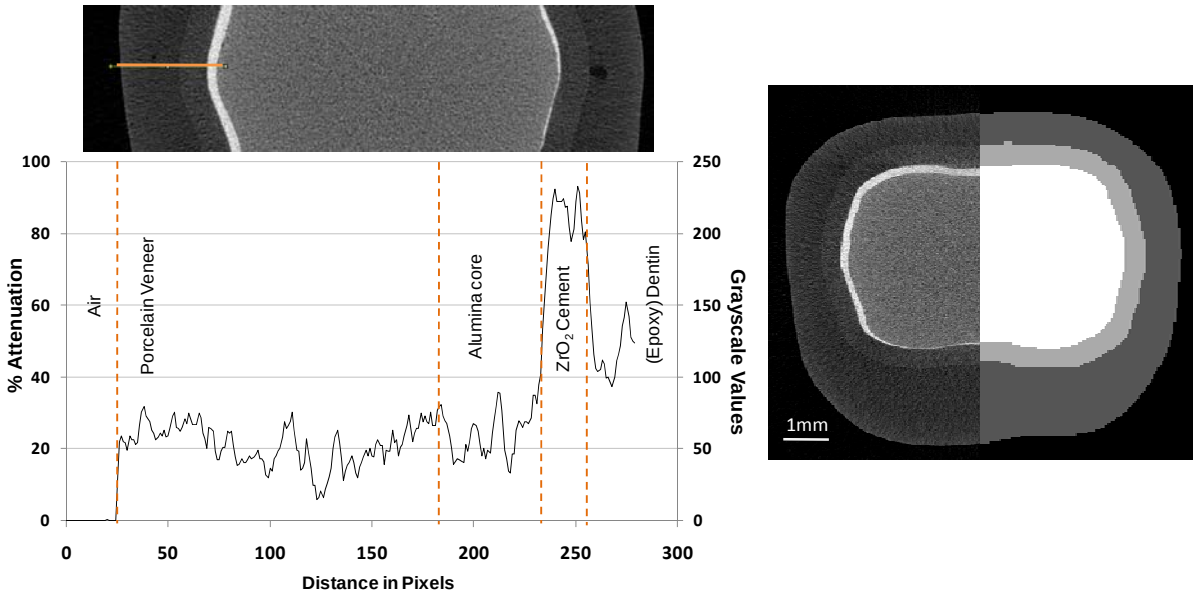

Figure 56 A 40% attenuation threshold value was used to segment the veneer and core regions in an alumina core crown. Semi - segmented area of 2D section of crown indicating the veneer(dark gray), core (gray) and dentin (white).

Image segmentation was conducted in a sequence of steps. Automatic segmentation based on the histograms was effectively implemented in segmenting the combined region of veneer and core, the zirconia adhesive and epoxy. Segmentation of the core and veneer failed using a global threshold value. Manually corrected segmentation was performed using a high resolution graphic tablet. This only accounted for 5% of the entire area. Certain sections of the crown, the top cusped region of the underlying core, in particular, significantly attenuate X-rays leading to beam hardening artifacts. Automatic volumetric segmentation based on the global histogram fails to work in these areas. Unselected regions of the segmented region were manually selected. Each region was individually segmented and assigned labels accordingly. Three regions namely – Porcelain veneer, alumina core and the dentin were segmented. Segmented zones can be stored in a binary image format for further usage. A volume mesh with closed boundaries was generated for each of the segmented labels with

constrained weighted smoothing. Smoothing reduces sharp segmentation artifacts which otherwise lead to vertices with bad qualities, usually severely distorted. The 3D surface model thus generated was constructed using a significant number of vertices (typically > 300,000 vertices). The next step of volumetric mesh generation, consisting of tetrahedral elements was based on the seed vertices generated in the surface model.

The number of 3D tetrahedra generated depends on the number of vertices generated in the surface model. Solid volumetric model generation based on the initial model was not possible due to limited memory. Additionally, a model consisting of more than a couple million tetrahedra would be computationally time consuming.

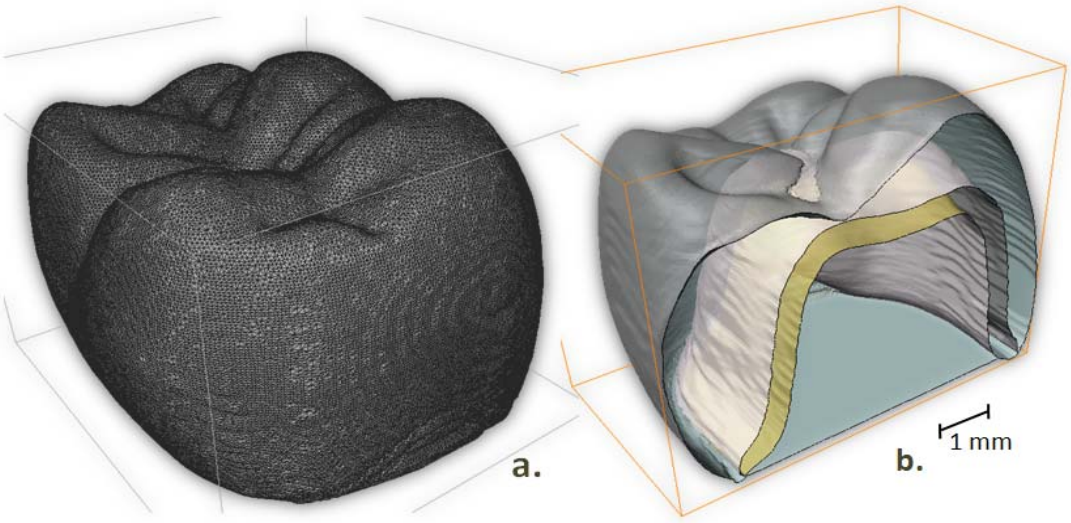

Figure 57 a) Original fine surface mesh with 315,983 faces. b) Cross sectional rendered view of surface mesh indicating the underlying layers.

Using a step wise gradual vertex reduction, the surface model was simplified to having close to 125,000 vertices as shown in Figure 59. Reduction in vertices is carried out by converging coplanar faces. It was observed that at a value close to 125,000 vertices, very few coplanar vertices remain (generally less than 10) and further reduction leads to a gradual modification

of the real geometrical features as shown in Figure 58. Since the internal volumetric mesh generation uses the surface mesh as seed points, further refinement of vertices leads to bigger volumetric tetrahedra which lead to edge effects in the simulation results.

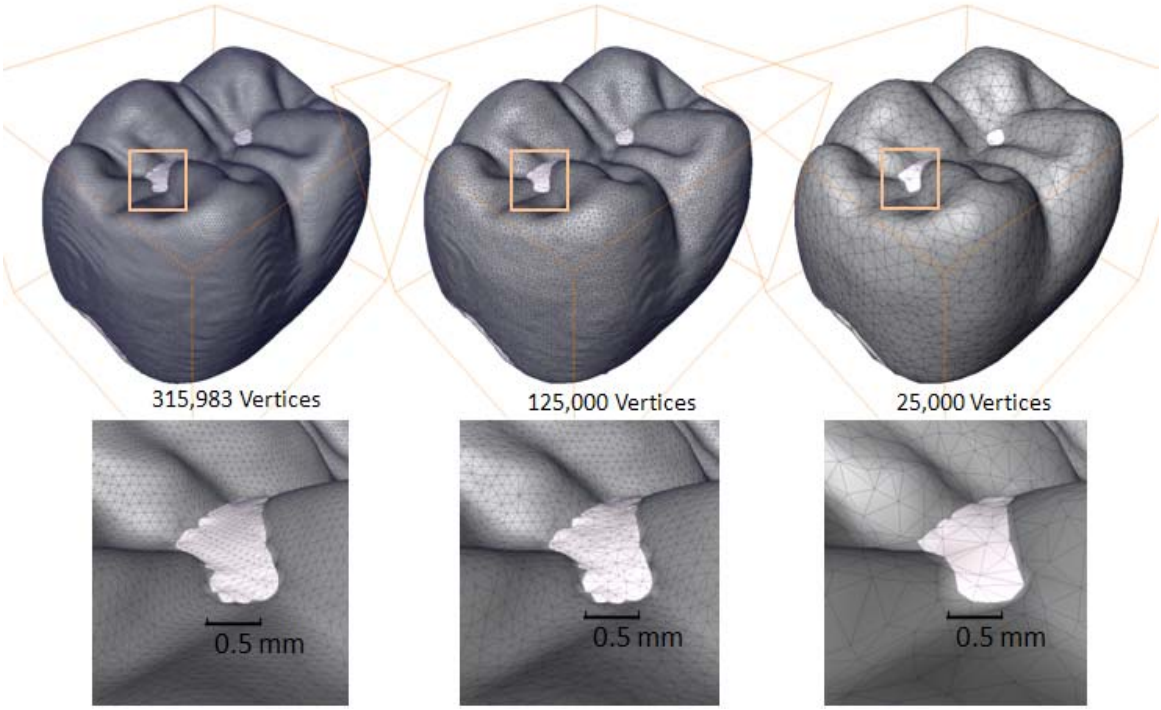

Figure 58 Illustration of the reduction in the number of surface vertices. A value of 125,000 (seen in b.) vertices was optimum. Further reduction results in modification of geometry and coarse mesh (seen in c.).

5.4 Finite Element Volume Mesh Generation

A solid tetrahedral C3D4 and C3D4H element mesh was constructed from the simplified surface model geometry. The closed boundary surface model was filled with solid tetrahedra through the marching cube algorithm. The resulting solid model consisted of 1,232,568 solid tetrahedra, with the corresponding material labels assigned based on the segmentation. HyperMesh (HyperWorks) was used to convert C3D4H elements to C3D4 and export the model in an Abaqus 6.8 import format.

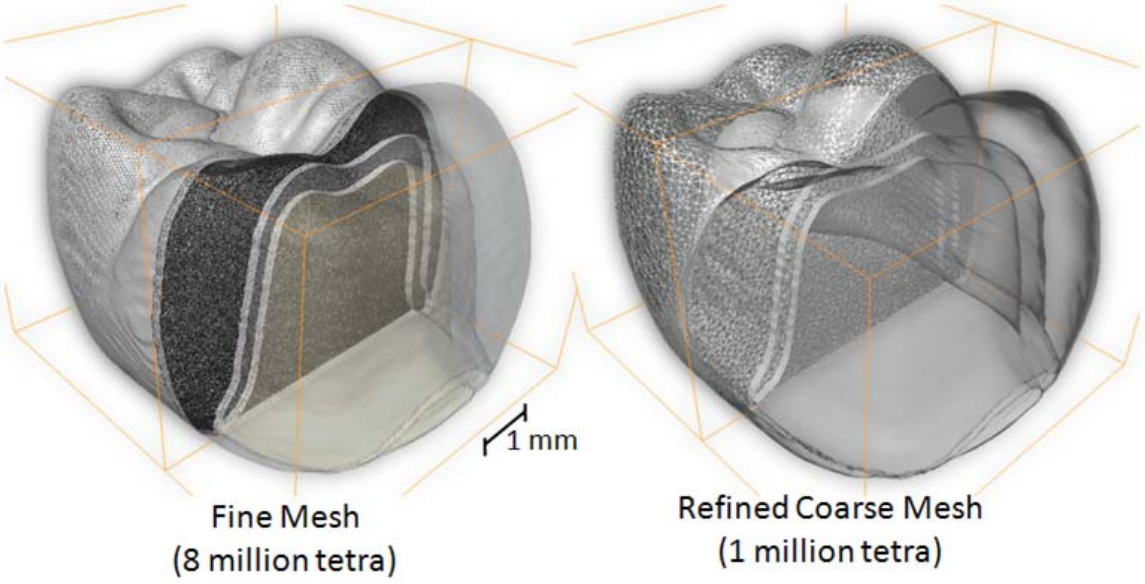

Figure 59 Illustration of the reduction in the number of volumetric tetrahedral (C3D4) elements without variation in spatial geometry.

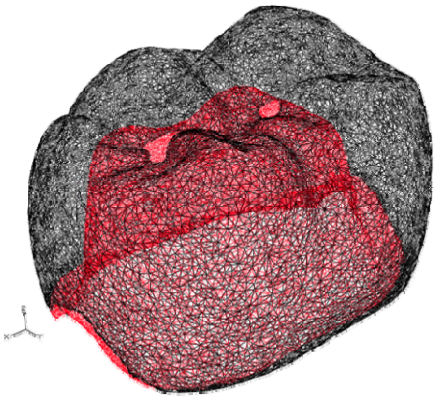

Figure 60 Illustration of the usage of sets to define a collection of nodes in a specific region of interest. Internal Region (red) indicates the node set that defines the interfacial surface between the core and the porcelain veneer.

5.5 Simulation of thermal residual stresses

Residual stresses that develop between the functional layers of a dental crown as a result of the mismatch in coefficients of thermal expansion were modeled using finite element modeling in Abaqus/Standard. The solid volumetric mesh model was imported from HyperMesh. A static, general temperature step starting with a pre-defined temperature field of 1000°C was applied. Following the initial temperature conditions, a cooling step was applied where in the temperature field was ramped down to 25°C to simulate the process of sintering.

The material properties namely - thermal expansion coefficient, Young's modulus and density were assigned to the individual sections through the use of sets. Abaqus uses the term "sets" for a group of pre-selected nodes in an assembly model. The usage of sets assists in rapidly assigning material properties, constraints or boundary conditions to a region of interest in the model. Selection of nodes belonging to a particular region manually was difficult due to the irregularity and complex internal shape.

The grouping of nodes into sets pertaining to different material sections were generated in AMIRA and exported using HyperMesh. The analysis was conducted on two models with the same geometry, but different material properties assigned to the core section. The analytical models were used to compare stresses developed in crowns consisting of alumina and zirconia cores. Properties of all the materials used in the simulation are listed in Table 9.

Table 9 Material properties of constituent layers of the dental crown [59]

Material	E (GPa)	Poisson's ratio	CTE ($10^{-6}K^{-1}$)
Glass	70	0.22	10.3
Y-TZP	205	0.22	11.0
Al_2O_3	370	0.22	8.0

5.6 Results

The residual stresses that develop as a result of the mismatch in the thermal expansion coefficients of the core and veneer material have been simulated using the real geometry. A comparison of the thermal residual stress results obtained from two simulation models: 1) a crown consisting of alumina and 2) one with a zirconia core are presented in Figure 61. From the values of the thermal expansion coefficient for the two layers used in each simulation, it was observed that the alumina core crown gave residual stresses of higher magnitude compared to the zirconia core crown. Average Von Mises stresses of 250 ± 50

MPa were observed for the alumina version. Higher magnitude Von Mises stresses of up to 400 MPa were observed in certain top cusped zones of the alumina core owing to the irregular folded geometry of the veneer.

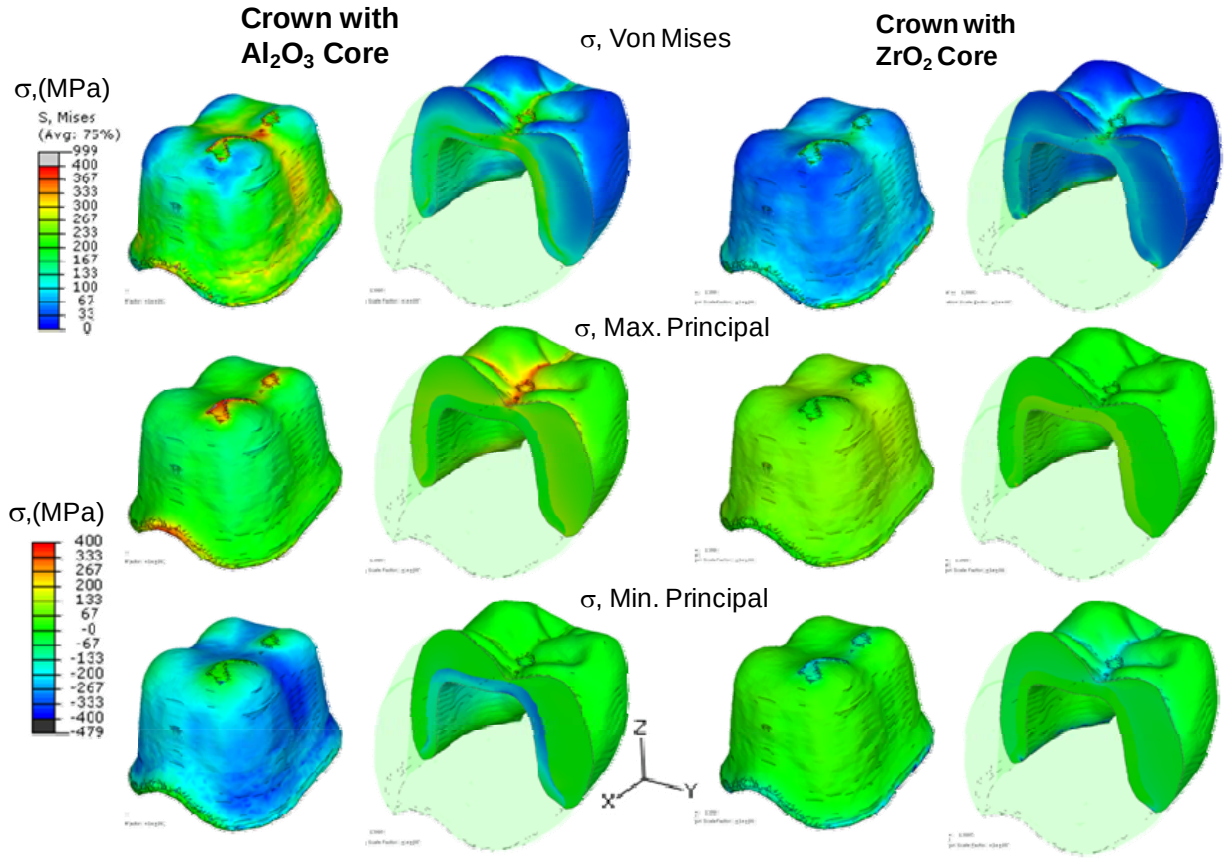

Figure 61 Results of the thermal simulation of the dental crown with alumina and zirconia core. Image also indicates the spatial distribution of stress on the top surface of the core, which was obtained by subtracting the veneer layer for better visualization purposes. Presented are the Von Mises stresses (Top), Maximum (Middle) and minimum (Bottom) principal stresses.

The regions of high stress concentration on the core had thinner sections of veneer. Comparatively lower residual stresses were observed with the zirconia core. Average Von Mises stresses up to 100 ± 25 MPa were observed in zirconia core with maximum stresses of 200 MPa being observed at identical locations of thinner veneer sections compared to

alumina. Observations of stress components as seen in Figure 62 indicate the alumina core to be in compression and the zirconia core in tension. A significant difference was observed in the minimum principal stresses at the interface of the alumina core and veneer as compared to the zirconia core.

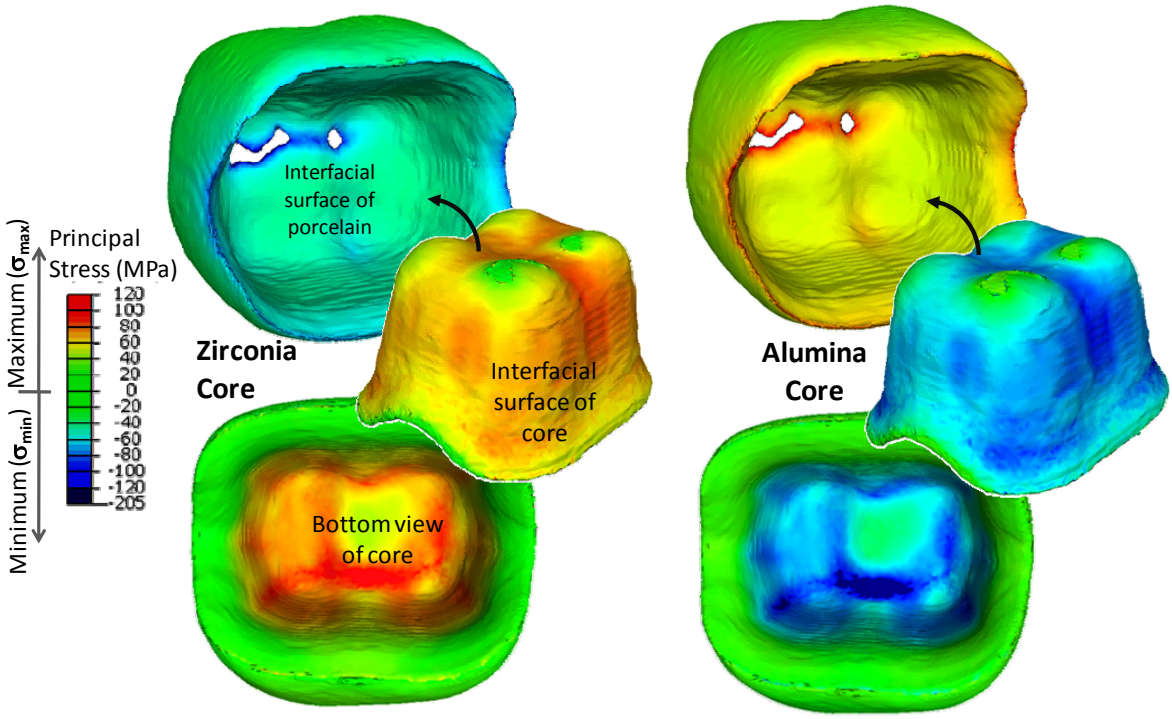

Figure 62 Segmented view of the simulated thermal residual stresses in crowns with zirconia core (left) and alumina core (right). The three views of each crown shows the differences of the residual stresses in the veneer and the core.

In general, regions of stress concentration were observed to be associated with regions having sharply ruffled contours such as ridges, and small crevices, particularly in the veneer. Residual stress results expressed in terms of Von Mises stress, do not provide information pertaining to the compressive or tensile nature of stresses. Residual stress results were obtained in terms of the minimum and maximum principal stresses. Isolated plots of the distribution of principal minimum or maximum stresses individually do not represent the overall residual stress state of the crown. A superposition of the maximum and minimum

principal stresses as shown in Figure 62, illustrates existence of compressive and tensile stresses in the core and veneer respectively. The gradients of these stresses were observed to be aligned parallel to the interface of the core and veneer. Nine different radial paths extending from the internal surface of the core to the exterior surface of the veneer were selected. The principal stresses for the nodes along these paths was extracted and plotted as a function of the distance from the interface as shown in Figure 63.

It was observed that the regions of veneer with thinner cross sections exhibited higher tensile stresses as seen in path 5. Higher values of residual tensile or compressive stress were observed at the interface, which gradually decay to relatively lower value far away from the interface. The cross sectional view of the crown (Figure 63) reveals the core to be subjected to an asymmetric compressive stress state of 350 ± 50 MPa. The irregular geometry of the veneer and varying thicknesses contributes to the localized asymmetric compressive stress in the veneer.

Simulations with identical boundary conditions used in analyzing the real geometry were conducted on simple cantilever beam geometry. Two cases were simulated, a zirconia-porcelain composite and an alumina- porcelain composite. Relatively higher interfacial residual stresses of close to 250 MPa were observed in the alumina –porcelain case compared to the zirconia-porcelain composite where a maximum stress of close to 80 MPa was observed (as seen in Figure 64).

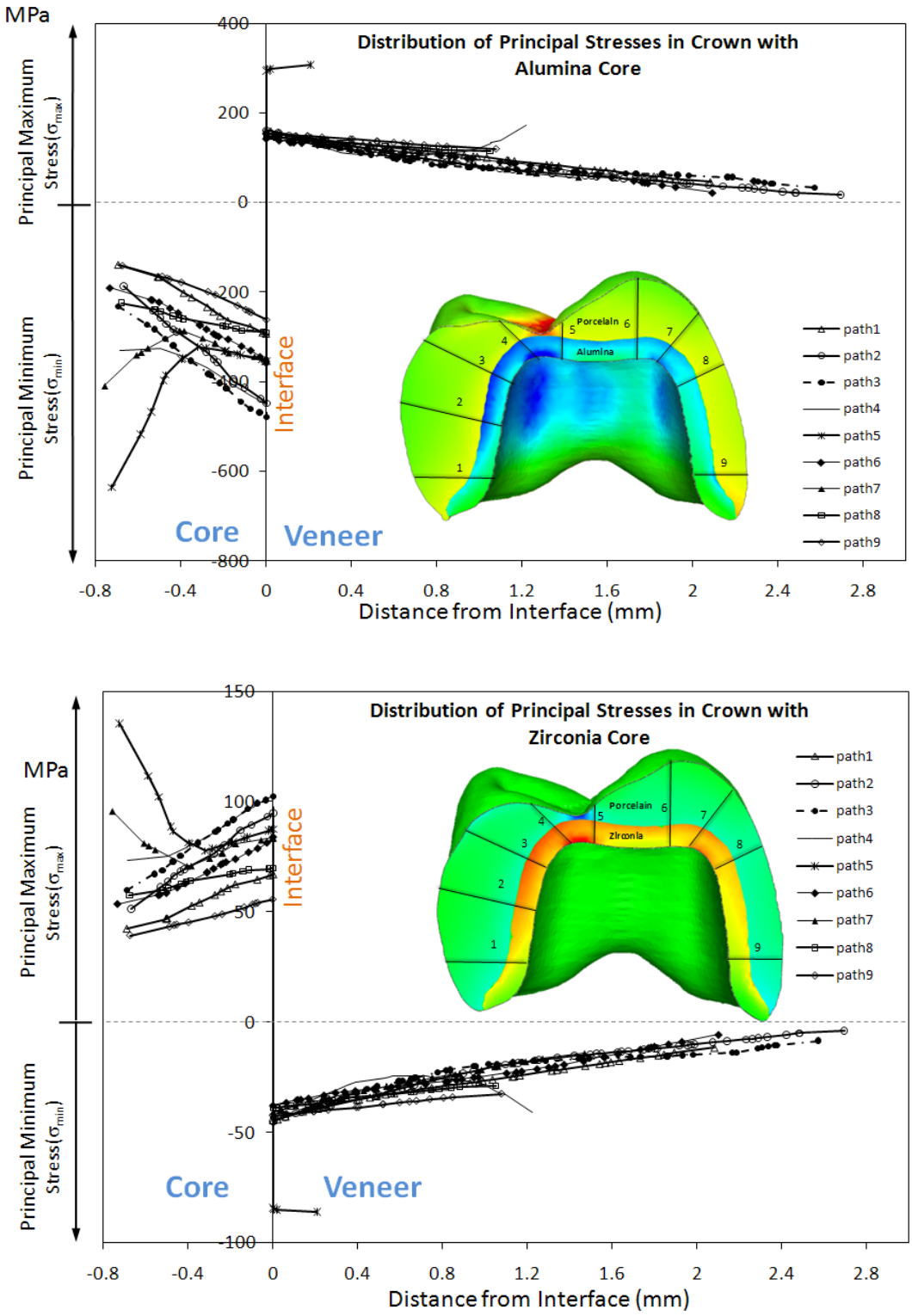

Figure 63 Variation of interfacial residual stresses with respect to distance from the interface. Principal Stresses were plotted along 9 paths located at different regions of the crown. The paths were traced perpendicular to the interface in the direction of the principal stresses.

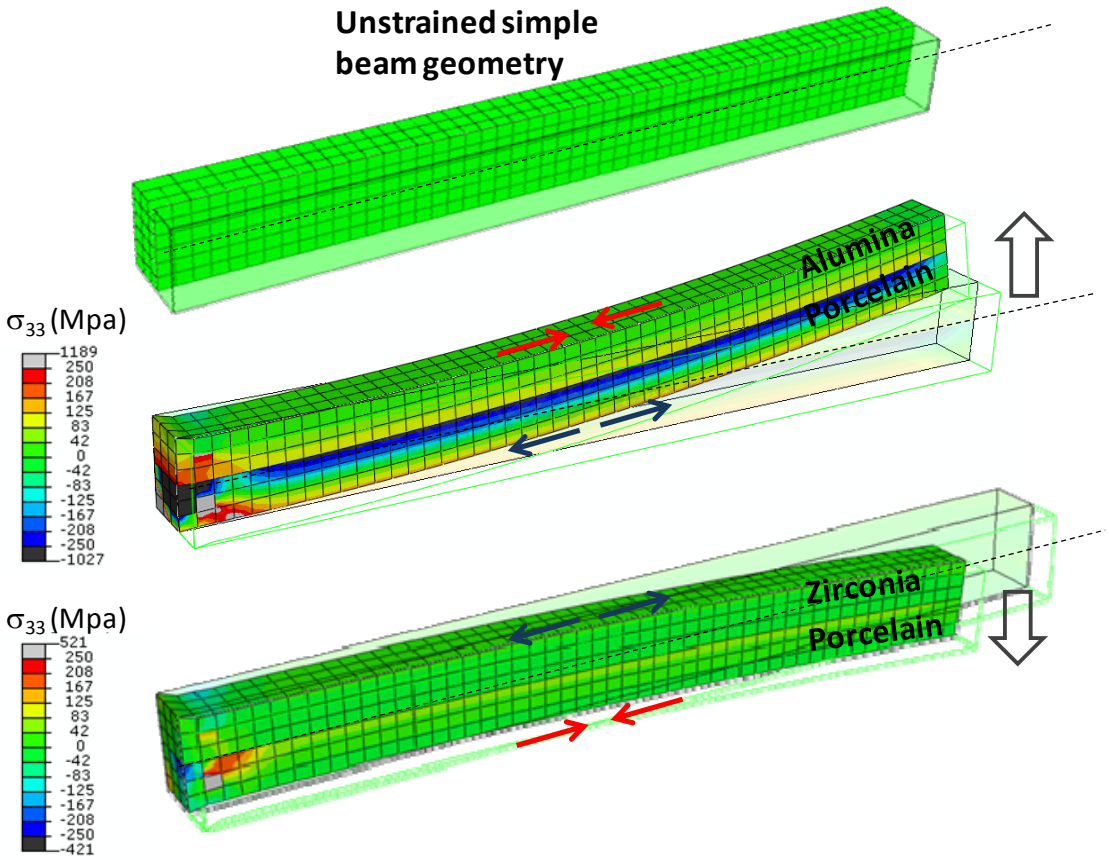

Figure 64 Simulation of the interfacial residual stresses in a cantilever beam geometry consisting of the composite of alumina-porcelain and zirconia-porcelain. The simulations indicate porcelain to be under tension in case of alumina-porcelain ceramic and under compression in case of porcelain-zirconia composite. The highest stresses were observed in the alumina – porcelain composite due to large mismatch in the thermal expansion coefficient.

5.7 Discussion

A simulation procedure capable of replicating real geometries has been developed and implemented on ceramic dental crowns. The aforementioned geometric model can be subjected to thermal, mechanical loading or other scenarios of interest. In the current study, thermal simulations of residual stresses that develop at an interface of the dental crown due to mismatch are reported. Accuracy of the values derived through simulation is strongly dependent upon the values of the thermal expansion coefficients. Literature values used in a

study by Coelho et al. [59], on simulation of clinical failures of all-ceramic crowns have been utilized. The values of the CTE reported for the veneer and core materials have a wide range. It is highly desirable to obtain precise CTE values, for the ceramic crown components being studied.

Significant stress variations were observed in the veneer region with higher convexity such as crevices and cleavages. Studies on loading effects on curved brittle layered structures carried out by Lawn et al. [73], indicate strong influence of curvature on failures. Models generated through CAD fail to replicate the intricacies of real geometry. Upon simulating the residual stress state, the crown can further be subjected to loads similar to chewing. From a dental context, the ability to closely simulate the initial residual stress state prior to loading plays an instrumental role. Simulations on real geometries, incorporating the complete geometric details would assist in non-destructively visualizing the impact; initial residual stresses have on crack initiation and propagation within the crown.

5.8 Conclusion

A method of generating finite element models representing real dental crown geometries has been devised with the use of micro-tomography to input spatial and material type information. Micron sized features such as voids, pores and surface contours were efficiently included. Simulation of thermal residual stresses that occur as a result of the mismatch in coefficient of thermal expansion, have been predicted for two different crown models consisting of alumina and zirconia cores. Geometry has a strong influence in the distribution of the residual stresses in the core. The magnitude of residual stresses at the interface is governed by the Young's modulus, coefficient of thermal expansion and the thickness of the veneer region. The magnitude of residual stresses in the crown with zirconia core was less compared to the core with the alumina core.

CHAPTER VI

6 CONCLUSIONS

Two advanced 2D X-ray diffraction experimental techniques for residual stress measurement at different length scales have been adapted for use on dental ceramics. Both the techniques rely on synchrotron X-rays, with high spatial resolution to measure stress based on changes in lattice spacing. In addition, an effective method of rapidly converting micro-tomography of a real geometry to a simulation-compatible finite element model has been developed. Geometry plays a significant role on the residual stress magnitude and location. For example, the curvature at a cusp provides localized stresses not observed in simple CAD based models. Results from the two experimental X-ray techniques complement each other and assist in summarizing the residual stress effects on dental restorations by bridging the gap between knowledge of micro-scale and macro-scale stresses.

Micro-Laue diffraction experiments revealed information of individual grains including details such as lattice orientation and grain-to-grain interaction. Strain measurement from the

micro-Laue technique is sensitive to the deviatoric component only, measured by quantifying the amount of lattice distortion. Even for monolithic zirconia, on which the mean type I stress was zero, a wide range, including +/-1 GPa, of type II stress was observed indicative of highly localized residual stress concentrations due to grain-to-grain anisotropy. This is a first observation of such highly localized stresses in zirconia, and their existence can have implications to fields beyond dentistry. A type I principal minimum stress of -218 MPa and a principal maximum of 43 MPa were observed in the monolith, derived by averaging type II stresses over a wide area.

Grain averaged interfacial residual stress results indicate a planar compressive residual stress greater than 270 MPa exists at the interface of zirconia and porcelain. Due to limited X-ray penetration depth into zirconia by micro-Laue diffraction, the stresses in the normal direction to the interface were determined within 2 μm of the interface. At this interface, a Type I principal minimum stress of -506 MPa and a principal maximum stress of 400 MPa was observed. Von mises stress values calculated from the deviatoric components in the case of the monolith and veneered zirconia shows the veneer layer introduces significant interfacial residual stress. The material response of monolith zirconia was studied when subjected to cyclic fatigue simulating mouth motion. Significant relaxation of 220 MPa in the Type I stress was observed after 40,000 fatigue cycles, where 45,000 cycles approximates a year of service.

An understanding of the macroscopic Type I stress can also be obtained by grain averaged residual stress measurement experiments. The $\sin^2\psi$ method proved to be a very effective tool in rapidly determining an average state of stress (Type I) over a wide area.

The $\sin^2\psi$ method was less helpful when measuring stresses through the porcelain layer due to X-ray absorption in porcelain. However, the technique produced exceptionally valuable results when applied in the measurement of the stress values on a cross sectional surface of the crown. The Type I grain averaged stress value was close to zero in the zirconia core, as expected. Such measurements help validate this new application of $\sin^2\psi$.

Away from the interface the far field average value of stress in the core of an intact crown was determined to be tensile with a magnitude of 250 ± 100 MPa. At the interface, a compressive biaxial residual stress of 250 ± 200 MPa was observed. High resolution interfacial area scans showed the presence of monoclinic stress induced transformation phase of zirconia. The monoclinic phase was confirmed through the comparison of diffraction peaks with standard powder diffraction data.

The interfacial residual stresses were relieved following fracture of the veneer. Post fatigue line scans performed on the region underneath the exposed interface region exhibit close to zero type I stress. Within 20 μm of the exposed interface layer of zirconia, the tetragonal phase existed in a tensile residual stress of greater than 300 MPa. The far field stress values in the zirconia core at the fracture site relaxed to zero.

X-ray micro-tomography using a laboratory based system provided 3D tomographs which were helpful in characterizing the micro-structural details of the zirconia dental crown. Additionally, the 3D tomographs were processed through 3D region segmentation. A useful technique of generating 3D real geometry volumetric mesh models was developed.

Thermal simulations of the introduction of residual stresses due to the process of firing porcelain veneer on the zirconia core were conducted. These simulations provided an improved interpretation of the distribution of the residual stresses in the irregular crown geometry. Simulations of two different crown models were performed. One of the crowns had an internal structural core made of alumina and the other was made of zirconia. Simulation results predict that the zirconia core was under tensile stresses and the porcelain veneer was under compressive stresses in the zirconia core. Minimum principal stresses up to 650 MPa (compressive) in the alumina core and a maximum principal stresses up to 170 MPa (tensile) in the zirconia core were observed, where the maximum principal stress was generally perpendicular to the interface. Cross-sectional views of the simulated results were utilized in comparing the results from monochromatic diffraction experiments. Simulations predicted values comparable to the experimental values at the far field.

Summarizing the experimental and simulated results on the zirconia – porcelain dental composite system, it can be concluded that, in the transition from metal based to all ceramic dental crowns the occurrence of residual stress was initially assumed to be minimal by the industry. It was attempted to minimize the residual stresses in all ceramic crowns through theoretical calculations and stoichiometric approaches. There existed a lack of a measurement technique and procedure to analyze the residual stresses within real components. It has long been established that concentrations of residual stresses and also zones of higher tensile residual stresses are detrimental to the life of a given component. Through the use of the above mentioned two advanced experimental technique of residual stress measurement and a simulation procedure, the problem of having an unknown residual stress would be tackled. It also will assist in developing improved dental restorations with

reduced localized residual stress concentrations and even distribution of the detrimental tensile stresses. The simulation method can further be utilized in post analysis of the geometry till a satisfactory design both in terms of materials and geometric structure is achieved.

CHAPTER VII

7 FUTURE DIRECTIONS

Several different aspects that can be refined and improved were encountered during the design and implementation of experiments, followed by tremendous amount of data analysis to acquire residual stress results. One such area is in the analysis of monochromatic X-ray data in the $\sin^2\psi$ mode. Current analysis uses only one of the rings among others to determine the residual stress in that direction. However, a typical diffraction image consisting of a number of rings contains much more comprehensive information on the stress tensor than is actually being extracted.

In order to determine the entire stress tensor, an analysis procedure that incorporates positions from all the diffraction rings must be developed. Currently the methodology adopted to fit the ring data, divides individual rings into psi segments and individually fits peaks for every integrated ψ segment. Based on the *d*-spacing determined from the integrated peak fit the slope of a *d* versus $\sin^2\psi$ plot is found from the least squares fit.

Significant errors are associated with the straight line fit to the data from the integrated peak fits. A sophisticated approach to this problem is through a whole diffraction ring fitting using the ellipsoid profile. Results obtained from such a fit would consider a continuity between ψ points and would provide a more accurate result compared to discretizing the ring.[75]

Finite element models show deviation from the actual result in spite of considering the real geometry. A major contributing factor to this deviation would be the effects contributed by the grain-to-grain interactions and anisotropy. The effects of stress induced phase transformation in zirconia have not been incorporated in the simulation model. There is considerable room for developing constitutive models that best predict the inter-granular stresses generated due to the volumetric change from phase transformation.

APPENDIX A

Post Image Processing Automated $Sin^2\psi$ Calculation

Front end of the VBA based $sin^2\psi$ calculation program

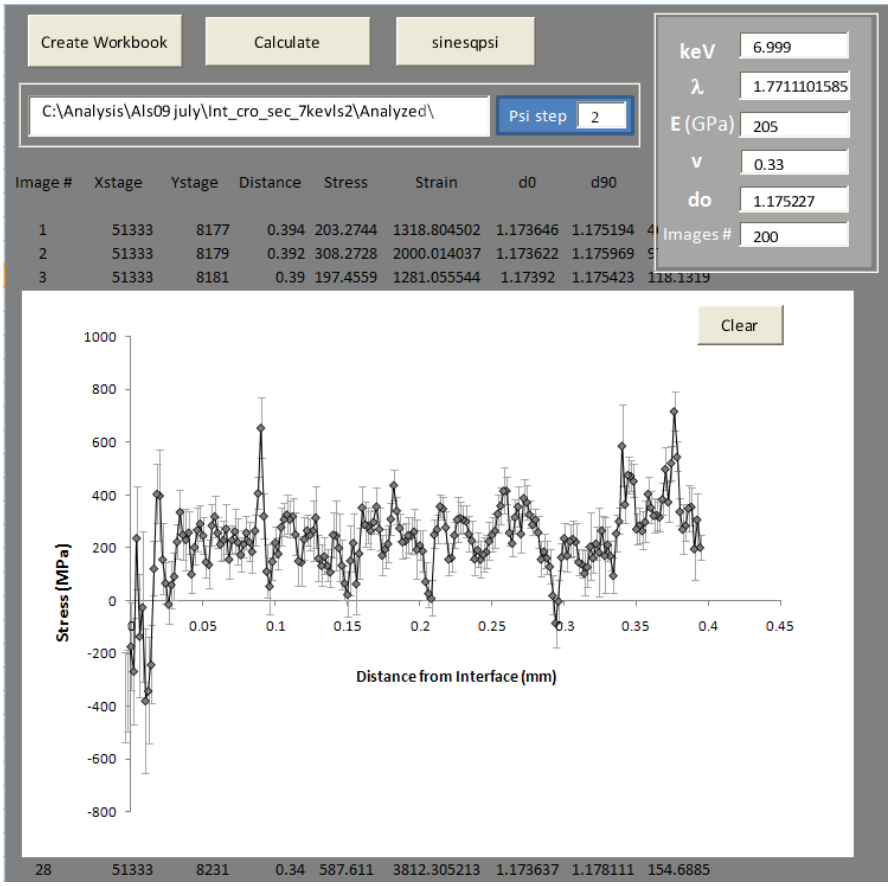

VBA Code

```
Public lamda, keV, E, v, d0 As Double
Private Sub calculatebtn_Click()
   Dim i, n As Integer
   Dim dir As String
   Dim path As String
   imagenum = (CInt(TextBox8.Value) + 2)
   path = TextBox1.Value
      ' MsgBox (path)
   n = TextBox2.Value
   If CInt(TextBox2.Value = "") Then
    MsgBox ("enter incremental value")
   End If


   For i = 36 To -36 Step -n

   If i = 0 Then

      ChDir _
      path
      Workbooks.OpenText Filename:= _
      path & "chi" & i & ".txt" _
      , Origin:=437, StartRow:=1, DataType:=xlDelimited, TextQualifier:= _
      xlDoubleQuote, ConsecutiveDelimiter:=True, Tab:=True, Semicolon:=True, _
      Comma:=True,          Space:=True,          Other:=True,          FieldInfo:=Array(Array(1,          1),          _

      Array(2, 1), Array(3, 1), Array(4, 1), Array(5, 1), Array(6, 1), Array(7, 1), Array(8, 1), _
      Array(9, 1), Array(10, 1), Array(11, 1), Array(12, 1), Array(13, 1), Array(14, 1)), _
      TrailingMinusNumbers:=True
      Sheets("chi" & i & "").Range("A1:N800").Select
      Selection.Copy
      Windows("Grouped.xlsm").Activate
      Sheets("psi" & i & "").Select
      ActiveSheet.Paste

      Call sheetoperation(imagenum)

      Windows("chi" & i & ".txt").Activate
      Application.CutCopyMode = False
      Windows("chi" & i & ".txt").Close


   ElseIf i > 0 Then
   ChDir _
      path
   Workbooks.OpenText Filename:= _
      path & "chi" & i & ".txt" _
      , Origin:=437, StartRow:=1, DataType:=xlDelimited, TextQualifier:= _
      xlDoubleQuote, ConsecutiveDelimiter:=True, Tab:=True, Semicolon:=True, _
      Comma:=True, Space:=True, Other:=True, FieldInfo:=Array(Array(1, 1), _
      Array(2, 1), Array(3, 1), Array(4, 1), Array(5, 1), Array(6, 1), Array(7, 1), Array(8, 1), _
      Array(9, 1), Array(10, 1), Array(11, 1), Array(12, 1), Array(13, 1), Array(14, 1)), _
      TrailingMinusNumbers:=True


      Sheets("chi" & i & "").Range("A1:N800").Select
      Selection.Copy
      Windows("Grouped.xlsm").Activate
```

```
    Sheets("psi" & i & "").Select
    ActiveSheet.Paste

    Call sheetoperation(imagenum)

    Windows("chi" & i & ".txt").Activate
    Application.CutCopyMode = False
    Windows("chi" & i & ".txt").Close
ElseIf i < 0 Then

       ChDir _
    path
Workbooks.OpenText Filename:= _
    path & "chim" & Abs(i) & ".txt" _
    , Origin:=437, StartRow:=1, DataType:=xlDelimited, TextQualifier:= _
    xlDoubleQuote, ConsecutiveDelimiter:=True, Tab:=True, Semicolon:=True, _
    Comma:=True, Space:=True, Other:=True, FieldInfo:=Array(Array(1, 1), _
    Array(2, 1), Array(3, 1), Array(4, 1), Array(5, 1), Array(6, 1), Array(7, 1), Array(8, 1), _
    Array(9, 1), Array(10, 1), Array(11, 1), Array(12, 1), Array(13, 1), Array(14, 1)), _
    TrailingMinusNumbers:=True

    Sheets("chim" & Abs(i) & "").Range("A1:N800").Select
    Selection.Copy
    Windows("Grouped.xlsm").Activate
    Sheets("psim" & Abs(i) & "").Select
    ActiveSheet.Paste

    Call sheetoperation(imagenum)
    Windows("chim" & Abs(i) & ".txt").Activate
    Application.CutCopyMode = False
    Windows("chim" & Abs(i) & ".txt").Close

End If
  Next i
Windows("SinSqPsi.xlsm").Activate
Sheets("Sheet1").Select
  End Sub


'-----------------------------------------------------------------------------------
' CALCULATION FOR DIATANCE, STRAIN AND ERROR
Private Function sheetoperation(imagenum)

ActiveSheet.Range("A2:M2").Select
Selection.Cut Destination:=ActiveSheet.Range("B2:N2")
ActiveSheet.Range("O2").Select
ActiveCell.Formula = "Distance From"
ActiveSheet.Range("P2").Select
ActiveCell.Formula = "Strain"
ActiveSheet.Range("Q2").Select
ActiveCell.Formula = "Error"
ActiveSheet.Range("R2").Select

ActiveSheet.Range("P1").Select
ActiveCell.Formula = "=AVERAGE(J3:J7)"
ActiveSheet.Range("P2").Select

ActiveSheet.Range("O3").Select
ActiveCell.Formula = "=-1*((C3-$C$200)/1000)"
ActiveSheet.Range("P3").Select
```

```
    ActiveCell.Formula = "=IF(G3<=0.2,NA(),((J3-$P$1)/$P$1)*10^6)"
    ActiveSheet.Range("Q3").Select
    ActiveCell.Formula = "=I3*50"
    ActiveSheet.Range("O3").Select
    Selection.AutoFill Destination:=ActiveSheet.Range("O3:O" & imagenum & "")
    ActiveSheet.Range("O3:O" & imagenum & "").Select
    ActiveSheet.Range("P3").Select
    Selection.AutoFill Destination:=ActiveSheet.Range("P3:P" & imagenum & "")
    ActiveSheet.Range("P3:P" & imagenum & "").Select
    ActiveSheet.Range("Q3").Select
    Selection.AutoFill Destination:=ActiveSheet.Range("Q3:Q" & imagenum & "")
    ActiveSheet.Range("Q3:Q" & imagenum & "").Select

End Function

Private Sub CommandButton1_Click()

    ActiveSheet.Range("A10:J5000").Select
    Selection.ClearContents

    Windows("SinSqPsi.xlsm").Activate
    Sheets("Sheet2").Select
    ActiveSheet.Range("C3:G50").Select
    Selection.ClearContents
    Windows("SinSqPsi.xlsm").Activate
    Sheets("Sheet1").Select
End Sub

Private Sub createwrkbookbtn_Click()
    Dim path, incr As String
    Dim i, n, incr1, incr2, incr3, incr4  As Integer

    keV = CDbl(TextBox3.Value)
    lamda = 12.396 / keV
    TextBox4.Value = lamda
    E = CDbl((TextBox5.Value) * 1000)
    v = CDbl(TextBox6.Value)
    d0 = CDbl(TextBox7.Value)
    incr = CInt(TextBox2.Value)
    path = TextBox1.Value
   'ADDING A NEW WORKBOOK AND RENAMING THE 3 INITIAL SHEETS
    Workbooks.Add
    Sheets("Sheet3").Select
    Sheets("Sheet3").Name = "psim36"

    incr1 = (36 - incr)
    incr2 = (36 - incr * 2)
    incr4 = (-36 + 3 * incr)
    Sheets("Sheet2").Select
    Sheets("Sheet2").Name = "psim" & incr1 & ""

    Sheets("Sheet1").Select
    Sheets("Sheet1").Name = "psim" & incr2 & ""
    num = 4

    'ADDING 22 NEW SHEET AND RENAMING THEM
    For i = 36 To incr4 Step -incr

    If i > 0 Then

    Sheets.Add
```

```
    Sheets("Sheet" & num & "").Name = "psi" & Abs(i) & ""

    ElseIf i = 0 Then
    Sheets.Add
    Sheets("Sheet" & num & "").Select
    Sheets("Sheet" & num & "").Name = "psi0"
    ElseIf i < 0 Then
    Sheets.Add
    Sheets("Sheet" & num & "").Select
    Sheets("Sheet" & num & "").Name = "psim" & Abs(i) & ""
    End If
       num = num + 1
    Next i
    'SAVING THE WORKBOOK

    ChDir path
    ActiveWorkbook.SaveAs Filename:= _
       path & "Grouped.xlsm", FileFormat:= _
       xlOpenXMLWorkbookMacroEnabled, CreateBackup:=False

    Windows("SinSqPsi.xlsm").Activate
    Sheets("Sheet1").Select

End Sub

Private Sub sinesqpsibtn_Click()

    Dim image, Index, psi, row, incr, row2, row3, num, imagenum, imagenum1, imagenum2, n As Integer
    Dim path As String
    Dim radians, lamda1, rpsi, rtheta, error_calc As Double


    path = TextBox1.Value
    incr = CInt(TextBox2.Value)
    keV = CDbl(TextBox3.Value)
    lamda = 12.396 / keV
    E = CDbl((TextBox5.Value) * 1000)
    v = CDbl(TextBox6.Value)
    d0 = CDbl(TextBox7.Value)
    imagenum = CInt(TextBox8.Value)
    n = 72 / incr + 1
    imagenum2 = 3 + n
    error_calc = E
    For row = 3 To (imagenum + 2)

    row3 = 3
       image = 3
       For psi = 36 To -36 Step -incr

          Sheets("Sheet2").Select
          Worksheets("sheet2").Cells(row3, 3) = psi
          rpsi = Application.WorksheetFunction.radians(psi)
          Worksheets("sheet2").Cells(row3, 4) = (Sin(rpsi)) ^ 2

          '------------------------enter two-theta

          Sheets("Sheet2").Select
          ActiveSheet.Range("E" & image & "").Select

          If psi > 0 Then
          ActiveCell.Formula = "=[Grouped.xlsm]psi" & psi & "!F" & row & ""
```

```
    ActiveSheet.Range("F" & row3 & "").Select
    ActiveCell.Formula = "=E" & row3 & "/2"
    rtheta = Application.WorksheetFunction.radians(Worksheets("sheet2").Cells(row3, 6))
    Worksheets("sheet2").Cells(row3, 7) = (1 / Sin(rtheta) * lamda / 2)

    image = image + 1

    ElseIf psi < 0 Then
    ActiveCell.Formula = "=[Grouped.xlsm]psim" & Abs(psi) & "!F" & row & ""
    ActiveSheet.Range("F" & row3 & "").Select
    ActiveCell.Formula = "=E" & row3 & "/2"
    rtheta = Application.WorksheetFunction.radians(Worksheets("sheet2").Cells(row3, 6))
    Worksheets("sheet2").Cells(row3, 7) = (1 / Sin(rtheta) * lamda / 2)

    image = image + 1

    ElseIf psi = 0 Then
    ActiveCell.Formula = "=[Grouped.xlsm]psi" & psi & "!F" & row & ""
    ActiveSheet.Range("F" & row3 & "").Select
    ActiveCell.Formula = "=E" & row3 & "/2"
    rtheta = Application.WorksheetFunction.radians(Worksheets("sheet2").Cells(row3, 6))
    Worksheets("sheet2").Cells(row3, 7) = (1 / Sin(rtheta) * lamda / 2)

    image = image + 1

    End If
  row3 = row3 + 1

Next psi

num = 72 / incr + 1
Dim calc_i As Integer
calc_i = num + 2
ActiveSheet.Range("I3").Select
ActiveCell.Formula = "=INTERCEPT(G3:G" & calc_i & ",D3:D" & calc_i & ")"
ActiveSheet.Range("J3").Select
ActiveCell.Formula = "=LINEST(G3:G" & calc_i & ",D3:D" & calc_i & ",,)"
ActiveSheet.Range("K3").Select
ActiveCell.Formula = "=I3"
ActiveSheet.Range("L3").Select
ActiveCell.Formula = "=J3+K3"
ActiveSheet.Range("M3").Select
ActiveCell.Formula = "=(L3 - K3) / K3 * 10 ^ 6"
ActiveSheet.Range("K5").Select
ActiveCell.Formula = "=STDEV(G3:G" & calc_i & ")"
ActiveSheet.Range("L5").Select
ActiveCell.Formula = "=STEYX(G3:G39,D3:D39)"
ActiveSheet.Range("N5").Select
ActiveCell.Formula = "=L5/K3*205000"
Worksheets("sheet2").Cells(5, 13) = ((Worksheets("sheet2").Cells(3, 10)) * E / (1 + v) / (Worksheets("sheet2").Cells(3, 9)))
Index = row - 2
row2 = row + 7

Windows("SinSqPsi.xlsm").Activate
Sheets("Sheet2").Select
ActiveSheet.Range("A1:Q50").Select
Selection.Copy
Workbooks.Add
ActiveSheet.Paste

Application.CutCopyMode = False
```

```
    ActiveWorkbook.SaveAs Filename:= _
       path & "Images\Image_" & Index & ".xlsx" _
       , FileFormat:=xlOpenXMLWorkbook, CreateBackup:=False
    Windows("Image_" & Index & ".xlsx").Close
    'Worksheets("sheet2").Cells(3, 3) = Index
    Worksheets("sheet1").Cells(row2, 1) = Index
    Worksheets("sheet1").Cells(row2, 5) = Worksheets("sheet2").Cells(5, 13) 'stress
    Worksheets("sheet1").Cells(row2, 6) = Worksheets("sheet2").Cells(3, 13) 'strain
    Worksheets("sheet1").Cells(row2, 7) = Worksheets("sheet2").Cells(3, 11) ' d0
    Worksheets("sheet1").Cells(row2, 8) = Worksheets("sheet2").Cells(3, 12) 'd90
    Worksheets("sheet1").Cells(row2, 9) = Worksheets("sheet2").Cells(5, 14) 'Error

    Index = 0

  Next row

  Windows("SinSqPsi.xlsm").Activate
    Sheets("Sheet2").Select
    ActiveSheet.Range("C" & imagenum2 & ":G50").Select
    Selection.ClearContents

  Windows("Grouped.xlsm").Activate
  Sheets("psi0").Select
  ActiveSheet.Range(Selection, Selection.End(xlDown)).Select
  ActiveSheet.Range("B3:C2000").Select
  Selection.Copy
  Windows("SinSqPsi.xlsm").Activate
  Sheets("Sheet1").Select
  ActiveSheet.Range("B10").Select
  ActiveSheet.Paste
  Application.CutCopyMode = False
  Windows("Grouped.xlsm").Activate
  Sheets("psi0").Select
  ActiveSheet.Range("O3").Select
  ActiveSheet.Range(Selection, Selection.End(xlDown)).Select
  Selection.Copy
  Windows("SinSqPsi.xlsm").Activate
  Sheets("Sheet1").Select
  ActiveSheet.Range("D10").Select
  Selection.PasteSpecial Paste:=xlPasteValues, Operation:=xlNone, SkipBlanks _
     :=False, Transpose:=False
  ActiveSheet.Range("D10").Select
  imagenum1 = imagenum + 10
  ActiveSheet.Range("A" & imagenum1 & ":H5000").Select
  Selection.ClearContents
  Windows("SinSqPsi.xlsm").Activate
  Sheets("Sheet1").Select
End Sub
Private Sub TextBox7_Change()
End Sub
Private Sub TextBox8_Change()
End Sub
```

REFERENCES

1. Thompson, V., *Personal Communication at Composites at Lake Louise, from I. Sailer.* University of Zurich, 2007.
2. Scott, H.G., *Phase relationship in zirconia-yttria systems.* Journal of Material Science, 1975. **10**: p. 1527-35.
3. Butler, E.P., *Transformation-toughened zirconia ceramics: critical assessment.* Material Science and Technology, 1985(1): p. 417-432.
4. Raigrodski, A.J., *Contemporary all-ceramic fixed partial dentures: a review.* Dent Clin North Am, 2004. **48**(2): p. viii, 531-44.
5. Raigrodski, A.J., *Contemporary materials and technologies for all-ceramic fixed partial dentures: A review of the literature.* Journal of Prosthetic Dentistry, 2004. **92**(6): p. 557-562.
6. Fradeani, M. and M. Redemagni, *An 11-year clinical evaluation of leucite-reinforced glass-ceramic crowns: A retrospective study.* Quintessence International, 2002. **33**(7): p. 503-510.
7. Coelho P. G., et al., *Laboratory Simulation of Y-TZP All-Ceramic Crown Clinical Failures.* Journal of Dental Research, 2008. **In Press**.

8. Lawn, B.R., Y. Deng, and V.P. Thompson. *Use of contact testing in the characterization and design of all-ceramic crownlike layer structures: A review*. 2001.

9. Kelly, J.R., *Ceramics in restorative and prosthetic dentistry.* Annual Review of Materials Science, 1997. **27**: p. 443-468.

10. Kisi, E.H. and C.J. Howard, *Elastic constants of tetragonal zirconia measured by a new powder diffraction technique.* Journal of the American Ceramic Society, 1998. **81**(6): p. 1682-1684.

11. Hannink, R.H.J., P.M. Kelly, and B.C. Muddle, *Transformation toughening in zirconia-containing ceramics.* Journal of the American Ceramic Society, 2000. **83**(3): p. 461-487.

12. Bale H A, et al., *Interface Residual Stresses in Dental Zirconia Using Laue Micro-Diffraction*, in *8th International Conference on Residual Stresses* 2008: Denver, CO.

13. Bale, H.A., J.C. Hanan, and N. Tamura, *4-D XRD for Strain in Many Grains Using Triangulation.* Powder Diffraction, 2006. **21**: p. 184.

14. Lewis, J.A., et al., *Direct Ink Writing of Three-Dimensional Ceramic Structures.* Journal of the American Ceramic Society, 2006. **89**(12): p. 3599-3609.

15. Hanan, J.C., et al., *Combined Diffraction and Tomography Analyzing Controlled Residual Stress in Solid Freeform Fabrication.* Synchrotron Radiation in Materials Science, 2006.

16. Hanan, J.C. and H.A. Bale, *Analysis of interface stress, impact and damage in ceramic dental restoration materials*, in *International Conference on Advanced Ceramics and Composites*. 2008, American Ceramics Society: Daytona, Florida.

17. Erlangen, *Die Zahnheilkunde.* 1851: p. 348.

18. Perine, G.H., New England Journal of Dentistry, 1883. **2**: p. 162.

19. Guerini, V. and A. National Dental, *A history of dentistry from the most ancient times until the end of the eighteenth century*. 1909, Philadelphia and New York: Lea & Febiger.

20. Black, G.V., *The physical properties of the silver-tin amalgams.* Dental Cosmos, 1896. **38**: p. 965-992.

21. Jorgensen, K.D. and T. Saito, *Structure and Corrosion of Dental Amalgams.* Acta Odontologica Scandinavica, 1970. **28**(1): p. 129-&.

22. Holland, G.A. and K. Asgar, *Some Effects on Phases of Amalgam Induced by Corrosion.* Journal of Dental Research, 1974. **53**(5): p. 1245-1254.

23. Mahler, D.B., *The high-copper dental amalgam alloys.* Journal of Dental Research, 1997. **76**(1): p. 537-541.

24. Land, C.H., *Porcelain Dental Art: No. II.* Dental Cosmos, 1903. **45**: p. 615-620.

25. McLean, J.W. and T.H. Hughes, *The reinforcement of dental porcelain with ceramic oxides.* Br Dent J, 1965. **119**(6): p. 251-67.

26. Helmer, J.D. and T.D. Driskell. *Research on Bio-ceramics*. in *Symposium on Use of ceramics as Surgical Implants*. 1969. South Carolina USA.

27. Piconi, C. and G. Maccauro, *Zirconia as a ceramic biomaterial.* Biomaterials, 1999. **20**(1): p. 1-25.

28. Holand, W., et al., *A comparison of the microstructure and properties of the IPS Empress (R) 2 and the IFS Empress (R) glass-ceramics.* Journal of Biomedical Materials Research, 2000. **53**(4): p. 297-303.

29. Nakamura, T., et al., *Fracture resistance of pressable glass-ceramic fixed partial dentures.* Journal of Oral Rehabilitation, 2002. **29**(10): p. 951-955.

30. Oh, S.C., et al., *Strength and microstructure of IPS Empress 2 class-ceramic after different treatments.* International Journal of Prosthodontics, 2000. **13**(6): p. 468-472.

31. Stappert, C.F.J., et al., *Fracture resistance of different partial-coverage ceramic molar restorations - An in vitro investigation.* Journal of the American Dental Association, 2006. **137**(4): p. 514-522.

32. Fasbinder, D.J., *Restorative material options for CAD/CAM restorations.* 2002. **23**: p. 911-922.

33. Otto, T., *Computer-aided direct all-ceramic crowns: Preliminary 1-year results of a prospective clinical study.* International Journal of Periodontics & Restorative Dentistry, 2004. **24**(5): p. 446-455.

34. Reich, S. and H. Hornberger, *The effect of multicolored machinable ceramics on the esthetics of all-ceramic crowns.* Journal of Prosthetic Dentistry, 2002. **88**: p. 44-49.

35. Hondrum, S.O., *Review of the strength properties of dental ceramics.* Journal of Prosthetic Dentistry, 1992. **67**(6): p. 859-865.

36. Xiao-ping, L., et al., *Strength and fracture toughness of MgO-modified glass infiltrated alumina for CAD/CAM.* Dental Materials, 2002. **18**: p. 216-220.

37. Magne, P. and U. Belser, *Esthetic improvements and in vitro testing of In-Ceram Alumina and Spinell ceramic.* International Journal of Prosthodontics, 1997. **10**: p. 459 - 466.

38. Fradeani, M., et al., *Five-year follow-up with Procera all-ceramic crowns.* . Quintessence Int, 2005. **2005**(36): p. 105-113.

39. Garvie, R.C., R.H. Hannink, and R.T. Pascoe, *Ceramic Steel?* Nature, 1975. **258**: p. 703 - 704.

40. Garvie, R.C. and P.S. Nicholson, *Phase analysis in zirconia systems.* . Journal of American Ceramic Society, 1972. **55**: p. 303 - 305.

41. Fischer, H. and R. Marx, *Fracture toughness of dental ceramics: comparison of bending and indentation method.* Dental Materials, 2002. **18**(1): p. 12-19.

42. Aboushelib, M.N., et al., *Microtensile bond strength of different components of core veneered all-ceramic restorations.* Dental Materials, 2005. **21**(10): p. 984-991.

43. van der Zel, J.M., et al., *The CICERO system for CAD/CAM fabrication of full-ceramic crowns.* . Journal of Prosthetic Dentistry, 2001. **85**: p. 261-267.

44. Piwowarczyk, A., et al., *A clinical report and overview of scientific studies and clinical procedures conducted on the 3M ESPE Lava All-Ceramic System.* . Journal of Prosthodontics, 2005. **14**: p. 39 - 45.

45. Valek, B.C., *X-ray Microdiffraction Studies of Mechanical Behavior and Electromigration in Thin Film Structures*, in *Material Science and Engineering*. 2003, Stanford University.

46. Tamura, N., et al., *Scanning X-ray microdiffraction with submicrometer white beam for strain/stress and orientation mapping in thin films.* Journal of Synchrotron Radiation, 2003. **10**: p. 137-143.

47. Henke, B.L., E.M. Gullikson, and J.C. Davis, *X-Ray Interactions - Photoabsorption, Scattering, Transmission, and Reflection at E=50-30,000 Ev, Z=1-92.* Atomic Data and Nuclear Data Tables, 1993. **54**(2): p. 181-342.

48. Polvino, S.M., N. Tamura, and O. Robach, *X-MAS Manual v1*. 2005.

49. Bale, H.A., N. Tamura, and J.C. Hanan. *Triangulation method for grain depth measurement using polychromatic micro-beam radiation*. in *Syncrotron Radiation for Material Science - 5*. 2006. Chicago.

50. Ganapathi, S.K., F.E. Spada, and F.E. Talke, *Residual stresses and their effect on wear behavior of polycrystalline zirconia overcoated disks.* Magnetics, IEEE Transactions on, 1992. **28**(5): p. 2533-2535.

51. Hwang, B., et al., *Residual Strain Gradients in a Fully Stabilized Zirconia Sample.* Journal of Applied Physics, 1988. **63**(11): p. 5351-5356.

52. Wu, A.W., *Thin Films -Stresses and Mechanical Properties - II.* MRS Symposium Proceedings, 1990. **188**: p. 191-205.

53. Zolotoyabko, E., B. Pokroy, and J.P. Quintana, *Depth-resolved strain measurements in polycrystalline materials by energy-variable X-ray diffraction.* Journal of Synchrotron Radiation, 2004. **11**: p. 309-313.

54. B B He, U.P., K L Smith, *Advantages of using 2D detectors for residual stress measurements.* Advances in X-ray Analysis, 2000. **42**: p. 429.

55. I C Noyan, J.B.C., *Residual Stress Measurement by Diffraction and Interpretation.* ((Springer, New York, 1987)).

56. B. B. He, K.L.S., *Fundamental Equation of Strain and Stress Measurement Using 2D Detectors.* Proceedings of 1998 SEM Spring Conference on Experimental and Applied Mechanics, 1998.

57. Hanan, J., *Damage evolution in uniaxial SiC fiber reinforced Ti matrix composites.* Ph. D. Dissertation, 2002.

58. P. Goudeaua, P.V., N. Tamura, H. A. Padmore, *Mesoscale x-ray diffraction measurement of stress relaxation associated with buckling in compressed thin films.* Applied Physics Letters, 2003. **83**(1).

59. Coelho, P.G., et al., *Laboratory Simulation of Y-TZP All-ceramic Crown Clinical Failures.* Journal of Dental Research, 2009. **88**(4): p. 382-386.

60. B. B. He, U.P., K. L. Smith, *Fundamentals of two-dimensional x-ray diffraction (XRD^2).* International Centre for Diffraction Data, Advances in X-ray Analysis, 2000. **43**.

61. Lawn, B., et al., *Failure modes in ceramic-based layer structures: A basis for materials design of dental crowns.* Journal of the American Ceramic Society, 2007. **90**(6): p. 1671-1683.

62. Farah, J.W. and R.G. Craig, *Distribution of stresses in porcelain-fused-to-metal and porcelain jacket crowns.* Journal of Dental Research, 1975. **54**(2): p. 255-261.

63. Farah, J.W. and R.G. Craig, F*inite-element stress analysis of a restored axisymmetric first molar.* Journal of Dental Research, 1974. **53**(4): p. 859-866.

64. Anusavice, K.J., B. Hojjatie, and P.H. Dehoff, *Influence of metal thickness on stress-distribution in metal-ceramic crowns.* Journal of Dental Research, 1986. **65**(9): p. 1173-1178.

65. Hojjatie, B. and K.J. Anusavice, *3-Dimensional Finite-Element Analysis Of Glass Ceramic Dental Crowns.* Journal of Biomechanics, 1990. **23**(11): p. 1157-1166.

66. Versluis, A., et al., *Residual shrinkage stress distributions in molars after composite restoration.* Dental Materials, 2004. **20**(6): p. 554-564.

67. Ausiello, P., et al., *Stress distributions in adhesively cemented ceramic and resin-composite Class II inlay restorations: a 3D-FEA study.* Dental Materials, 2004. **20**(9): p. 862-872.

68. De Jager, N., P. Pallav, and A.J. Feilzer, *The influence of design parameters on the FEA-determined stress distribution in CAD-CAM produced all-ceramic dental crowns.* Dental Materials, 2005. **21**(3): p. 242-251.

69. Bale, H.A., J.C. Hanan, and J.E. Smay, *Thermal Interface Stresses Including 3D Microstructures in Layered Free-Form Ceramics* Advances in Bioceramics and Porous Ceramics: Ceramic Engineering and Science Proceedings, 2008. **29**(7).

70. Magne, P., *Efficient 3D finite element analysis of dental restorative procedures using micro-CT data.* Dental Materials, 2006(958).

71. Verdonschot, N., et al., *Generation of 3-D finite element models of restored human teeth using micro-CT techniques.* International Journal of Prosthodontics, 2001. **14**(4): p. 310-315.

72. Fischer, J., et al., *Effect of thermal misfit between different veneering ceramics and zirconia frameworks on in vitro fracture load of single crowns.* Dental Materials Journal, 2007. **26**(6): p. 766-772.

73. Qasim, T., et al., *Effect of off-axis concentrated loading on failure of curved brittle layer structures.* Journal of Biomedical Materials Research Part B-Applied Biomaterials, 2006. **76B**(2): p. 334-339.

74. Qasim, T., et al., *Contact damage in brittle coating layers: Influence of surface curvature.* Journal of Biomedical Materials Research Part B-Applied Biomaterials, 2005. **73B**(1): p. 179-185.

75. Hanan, J.C., E. Ustundag, and J.D. Almer, *A New Analysis Method for Two-Dimensional X-Ray Data.* Adv. X-Ray Anal., 2004. **47**.

VITA

Hrishikesh Bale

Candidate for the Degree of

Doctor of Philosophy

Dissertation: MEASUREMENT AND ANALYSIS OF RESIDUAL STRESSES IN ZIRCONIA DENTAL COMPOSITES USING MICRO X-RAY DIFFRACTION

Major Field: Mechanical and Aerospace Engineering

Biographical:

Personal Data: Born in Belgaum, Karnataka, India.

Education:

- Received the B.S. degree from Visveswaraiah Technological University, Belgaum, Karnataka, India, 2002, in Mechanical Engineering.
- Received the M.S. degree from Oklahoma State University, Stillwater, OK, 2005, in Mechanical Engineering.
- Completed the requirements for the degree of Doctor of Philosophy with a major in Mechanical and Aerospace Engineering in Oklahoma State University in May, 2010.

Experience:

- Graduate Research Assistant for Dr. Jay Hanan, Oklahoma State University, Stillwater, OK (2004 – 2009)
- Teaching Assistant for Dr. R. D. Delahoussaye, Oklahoma State University, Stillwater, OK (2003 – 2004)
- Trainee Engineer, Nirmiti Tools Pvt. Ltd. (2002-2003)

Professional Memberships:
Phi Kappa Phi

Name: Hrishikesh Bale Date of Degree: May, 2010

Institution: Oklahoma State University Location: Stillwater, Oklahoma

Title of Study: MEASUREMENT AND ANALYSIS OF RESIDUAL STRESSES IN ZIRCONIA DENTAL COMPOSITES USING MICRO X-RAY DIFFRACTION

Pages in Study: 132 Candidate for the Degree of Doctor of Philosophy

Major Field: Mechanical and Aerospace Engineering

Due to their aesthetic value and high compressive strength, dentists are utilizing ceramics as a material of choice for dental restorations. Among ceramics, zirconia provides high toughness and crack resistance. Residual stresses develop in processing due to factors including coefficient of thermal expansion mismatch, geometry, and grain anisotropy. In the present study, advanced methods were adapted including polychromatic X-ray (Laue) micro-diffraction, which provided grain orientation and residual stresses, and monochromatic diffraction in the $\sin^2\psi$ mode. Analysis tools for both methods were developed to provide grain averaged and grain specific material properties on clinically relevant specimens.

Large type II residual stress variations ranging from – 1 to + 1 GPa were observed between grains. Most grains in monolithic zirconia have a mean compressive deviatoric stress of 70 MPa, depending on direction. Another important part of the study was the interface residual stresses which occur at the interface of a base/core region of a dental restoration and the veneer. Type I residual stresses as high as 800 MPa were observed at the interface. A detailed analysis of the effects of simulated mouth motion impact fatigue cycling on the residual stress states revealed significant relaxation of the residual stress from 800 MPa to around 150 MPa within 45,000 cycles. Results from the $\sin^2\psi$ residual stress measurement technique revealed significantly higher tensile stresses in the zirconia core. Equivelant to approximately one year's service, 45,000 fatigue cycles at a load of 150N led to fracture of the porcelain veneer cusp. Residual stress at the site of fracture indicates relaxation of residual stress. At the interface, stress induced phase transformation of zirconia forming monoclinic phase was observed. Residual stresses can promote crack growth and thereby catastrophic failure. These results have implications for all materials particularly structural ceramics.

ADVISER'S APPROVAL: Dr. Jay C. Hanan